INFORMATION TO USERS

This manuscript has been reproduced from the microfilm master. UMI films the text directly from the original or copy submitted. Thus, some thesis and dissertation copies are in typewriter face, while others may be from any type of computer printer.

The quality of this reproduction is dependent upon the quality of the copy submitted. Broken or indistinct print, colored or poor quality illustrations and photographs, print bleedthrough, substandard margins, and improper alignment can adversely affect reproduction.

In the unlikely event that the author did not send UMI a complete manuscript and there are missing pages, these will be noted. Also, if unauthorized copyright material had to be removed, a note will indicate the deletion.

Oversize materials (e.g., maps, drawings, charts) are reproduced by sectioning the original, beginning at the upper left-hand corner and continuing from left to right in equal sections with small overlaps.

ProQuest Information and Learning
300 North Zeeb Road, Ann Arbor, MI 48106-1346 USA
800-521-0600

IN VIVO MEASUREMENTS OF ALUMINUM AND STRONTIUM IN HUMAN BONE

By

Ana Pejović-Milić, M.Sc.

A Thesis

Submitted to the School of Graduate Studies

in Partial Fulfillment of the Requirements

for the Degree

Doctor of Philosophy

McMaster University

DOCTOR OF PHILOSOPHY (2001) McMaster University
(Medical Physics) Hamilton, Ontario

TITLE: *IN VIVO* MEASUREMENTS OF ALUMINUM AND STRONTIUM IN HUMAN BONE

AUTHOR: Ana Pejović-Milić, M.Sc. (University of Belgrade and McMaster University)

SUPERVISOR: Professor David R. Chettle, Ph.D.

NUMBER OF PAGES: xv, 182.

Život ljudski večno je plakanje.

Sa plačem se radja i umire,

Pri radjanju plače ko dolazi,

Pri umoru plače ko ostaje.

Pevanje je plakanje bez suza.*

Tadija Ž. Pejović

---

*In the honor of three generations of Doctors of Philosophy in the family - my grandfather's thoughts:

Life is constant crying.
In tears we are born,
In tears we are dieing.
At birth cries who is coming,
At death cries who is staying.
Singing is tearless crying.

ABSTRACT

This thesis investigated a means of improving bone aluminum measurement using neutron activation analysis which has been previously demonstrated for measuring trace and minor elements in human tissues. Currently, a KN Van de Graaff-accelerator was used with irradiation parameters of 2 MeV proton energy and 100 μA current, to activate aluminum via the $^{27}Al(n, \gamma)^{28}Al$ reaction. A minimum detectable limit of 1.14 mg of aluminum in hand was achieved, accompanied with a hand dose of 48 mSv delivered to the subject. Further improvements in the sensitivity of aluminum assessment has been investigated by Monte Carlo modeling, and a new irradiation cavity has been proposed. The cavity design focused on increasing the thermal neutron flux to the hand, while providing additional shielding to the subject, and therefore, it should allow ethics approval for *in vivo* testing and application.

A source-based x-ray fluorescence (XRF) technique of bone strontium was also developed. The designed XRF system was tested *in vivo* on ten subjects, successfully detecting the strontium quantities in the finger bone. Furthermore, three normalization techniques were investigated such as: coherent normalization, the strontium Kα/Kβ x-ray ratio and the Sr/Ca ratio in bone. The feasibility of normalizations show that none of the normalization can be reliably applied to healthy subjects. Therefore, an ultrasound measurement was an integral part of strontium XRF, as a means to measure overlying tissue thickness at the measurement site that was necessary for the estimation of bone strontium concentration during the course of this work.

ACKNOWLEDGMENTS

Throughout this work, I have experienced many professional and personal doubts as well as difficulties. Luckily, I was able to overcome them and bring this thesis together mainly because of two men. First is my supervisor, Dr. David R. Chettle, who honored me by accepting me as his student. David persistently pointed out to me my weaknesses and strengths in the last six years, leading me to the Doctor of Philosophy title. Thank you for everything. The second man is first in my heart, my husband Dejan, who gives me his strength to succeed at my dreams.

I would like to show gratitude to the members of my committee, Drs. C. E. Webber, W. V. Prestwich and F. E. McNeill for their helpful suggestions and ideas during the completion of this project.

I extend my gratitude to my dear friends and colleagues, Michelle Arnold and Sandra Bateman for review and translation of this text from my "English" to understandable English, but most importantly for all the fun that we had in the "girls house without a window". Appreciation also goes to the graduate students in medical physics for the open and stimulating scientific environment that I have enjoyed at McMaster.

Thanks to Jim Stark, John Cave and Marek Kiela for technical assistance, patience during my experiments and fast running, and many good morning coffees.

Finally yet importantly, these years had happy and demanding moments that two small boys, Misha and Luka, brought into my life. During my study at McMaster I have learned many other important things, that are much harder than my work presented in this thesis, as a mother. While this work will be soon shelved, my sons will continue to bring joy, happiness and more challenges to Dejan's and my life. I would like to dedicate this work to them and their future.

TABLE OF CONTENTS

LIST OF FIGURES

PART I ***In Vivo* Neutron Activation Analysis of Aluminum in Human Bone**

LIST OF TABLES

PART I

In Vivo Neutron Activation Analysis of Aluminum in Human Bone

Chapter I

Introduction

When the body is irradiated with neutrons, penetrating gamma rays are emitted both during irradiation (prompt gamma emission) and for some elements afterwards (delayed gamma emission). These gamma rays originate from atomic nuclei that have absorbed energy from the neutrons or captured the neutrons themselves, and the energies of the emitted gamma rays are characteristic of the nucleus which emits them. Energy sensitive detectors can identify the emitting nucleus, and the number of gamma rays detected at a given energy may be used to determine the abundance of the target nucleus in the body. The technique that is outlined here is the *in vivo* neutron activation analysis of a live irradiated sample, and it has been reviewed and well explained previously (Chettle and Fremlin, 1984; Scott and Chettle, 1986; Sutcliffe, 1996).

Many elements have been measured using *in vivo* neutron activation analysis, applying different neutron sources, and therefore, delivering different doses to the subjects. The advantage of a neutron – gamma ray combination for *in vivo* applications is that both neutrons and photons have fairly long attenuation mean free paths in tissue (a few centimeters), making it possible to consider deep organs. Typical neutron sources are ^{238}Pu-Be, ^{241}Am-Be and ^{252}Cf, or nuclear reactors and particle accelerators. Every source has a different neutron energy spectrum and flux; therefore, these components have to be considered for a specific application, as well as the dose that the source will deliver to the subject.

Several elements have been studied because of their potential to be used for *in vivo* neutron activation. Those that have been successfully measured can be separated into two groups consisting of essential and trace elements. The more abundant elements are hydrogen, calcium, potassium, sodium, chlorine and nitrogen, while the measured trace elements are manganese, cadmium, aluminum, iodine, silicon and zinc, to name a few.

The key disadvantages of *in vivo* neutron activation analysis are the energy dependence of a nuclear cross-section, the complexity of human gamma ray spectra, as well as the possibility of disturbance from an interfering interaction that will produce the same reaction product, but from a different element in the body. Generally, the whole body dose delivered during this procedure may be up to 10 mSv, greatly influencing its application. In addition, the element's half-life and cross-section may impose additional limits to the application of *in vivo* neutron activation analysis.

The first part of this work will discuss and propose a way to measure aluminum levels in human bone using *in vivo* neutron activation analysis. Although aluminum can be measured, this element has many inconvenient characteristics for neutron activation analysis. There is a rather low probability of interaction with thermal neutrons, a very short half-life for a comfortable *in vivo* measurement, several interfering interactions that will be discussed later, as well as an inconvenient gamma ray energy in the upper tail of the chlorine peak, given that chlorine is always present in the human body. Besides all of these constraints that cannot be altered or adjusted, aluminum levels in healthy subjects, or more precisely in their bones, are very low.

1.1 *In Vivo* Neutron Activation Analysis of Aluminum

Aluminum may be measured, using neutron activation analysis, as either total body aluminum or aluminum in a part of the body via the thermal neutron reaction $^{27}Al(n,\gamma)^{28}Al$ ($\sigma = (231\pm3)$ mb). ^{28}Al is radioactive, with a half life of 2.25 min., and decays by the emission of a 2.865 MeV β^- particle accompanied by a 1.78 MeV gamma ray (100 %).

In addition to this thermal neutron reaction, aluminum undergoes the fast neutron reactions $^{27}Al(n,p)^{27}Mg$ and $^{27}Al(n,\alpha)^{24}Na$. Each of these three nuclear reactions suffer from interference from other elements activated by neutrons in the body. For the $^{27}Al(n,\gamma)^{28}Al$ reaction a further complication is the interference from the fast neutron nuclear reactions of $^{31}P(n,\alpha)^{28}Al$ and $^{28}Si(n,p)^{28}Al$, with thresholds of 1.95 MeV and 4

MeV respectively. Since these reactions also produce ^{28}Al, the measured intensity of 1.78 MeV gamma rays could in general be partially due to the presence of ^{31}P and ^{28}Si in the irradiated sample. Phosphorus is present in large amounts in biological materials and its contribution to the ^{28}Al activation must be corrected for, or its concentration must be known. The interference produced by silicon requires only a small correction factor. Similarly, the ^{27}Al $(n,p)^{27}Mg$ reaction suffers interference from the $^{26}Mg(n,\gamma)^{27}Mg$ reaction, and $^{27}Al(n,\alpha)^{24}Na$ from the $^{23}Na(n,\gamma)^{24}Na$ reaction.

For the (n,p) and (n,α) reactions with ^{27}Al the interference is caused by thermal neutrons, thus the moderation of fast and slow neutrons within the body will always provide some thermal flux to provoke these interfering reactions. The $^{27}Al(n,\gamma)^{28}Al$ reaction, however, is a thermal reaction itself and is interfered with by fast neutron reactions. Therefore, it allows for the possibility of eliminating the fast neutron component from the neutron beam thus preventing the activation of ^{31}P and ^{28}Si.

After the exposure to a neutron beam and the transfer time, sample counting is usually done with low-background detectors, usually NaI (Tl) crystals with large surface areas and volumes. The area or amplitude of the ^{28}Al peak, at 1.78 MeV, gives a measure of the quantity of aluminum present in the body once all necessary corrections are made.

According to the chemical composition of Reference Man cited by ICRP 23 (1975), the content of aluminum in the skeleton is 21 mg. Knowing that 1.25 % of the skeleton is in one hand (the typical irradiated site during the procedure), the expected content of aluminum in the hand of a healthy adult is 0.2 - 0.3 mg. Bone in the hand is composed of 95 % cortical and 5 % trabecular bone (ICRP 70, 1995). For successful *in vivo* neutron activation analysis of aluminum, where only part of the body is exposed to a

neutron beam, it is assumed that aluminum is homogeneously distributed in the skeleton. Due to the small amount of overlying tissue between the external neutron source and the bone mineral in the hand, the attenuation of neutrons by tissue is considered to be negligible.

The absolute number of counts from aluminum in the hand depends upon the size of the hand, the thickness of overlying tissue, and the neutron field profile as well as the irradiation and counting geometry. However, it was shown that the need for extensive corrections for all these factors can be eliminated through the use of γ rays emitted by ^{49}Ca as a normalization parameter for the ^{28}Al intensity detected. It was demonstrated as well that the Al/Ca ratio is simply proportional to the aluminum concentration in bone (Ellis *et al.*, 1988). The Al/Ca ratio, therefore, provides an index of elevated aluminum per unit bone mass.

Calcium neutron activation is based on the $^{48}Ca(n,\gamma)^{49}Ca$ ($\sigma_{TH} = 1.09 \pm 0.14$ b) reaction. The amplitude of the ^{49}Ca gamma peak positioned at 3.084 MeV (100%), gives a measure of the quantity of calcium present in the bone or the irradiated bone mass. In the Reference Man skeleton there is 1180 g of natural calcium or 15 g in one hand. Knowing that ^{48}Ca comprises 0.187 % of natural calcium, about 27 mg of ^{48}Ca may be expected to be in the hand.

The non-invasive *in vivo* measurement of aluminum body burden based on neutron activation analysis of ^{27}Al in bones is presented as a feasible and practical technique of monitoring aluminum levels in the body. Previous studies have been undertaken at Brookhaven National laboratory, Long Island, New York (Ellis *et al.*, 1988) and at McMaster University, Hamilton (Palerme *et al.*, 1993a) using reactor based

sources; at Swansea (Wyatt *et al.*, 1993a; 1993b) using a ^{252}Cf source, and at the University of Birmingham using a Dynamitron accelerator to produce neutrons via the $^{3}H(p,n)^{3}He$ reaction (Green and Chettle, 1992, Green *et al.*, 1993).

At all four research centres, neutron activation analysis of aluminum in the hand was performed. Each centre used the neutron sources mentioned above, delivering different equivalent doses to the hand, with different detection limits and sensitivities. As seen in table 1.1, the Brookhaven study, using a nuclear reactor, demonstrated the best detection limit, which is still greater than the mass of aluminum expected in the hand, as well as the lowest delivered dose. The pilot study at the McMaster reactor demonstrated that the interference reactions arising from the interaction of fast neutrons with phosphorus and silicon in the hand reduces the effectiveness of reactor based neutron sources. However, this work failed to reach the low minimum detectable limit reported in the Brookhaven study. Furthermore, a nuclear reactor is a questionable neutron source for a routine diagnostic procedure simply in terms of its availability to the medical community.

Place	Source	Hand dose (mSv)	Effective dose* (μSv)	MDL (mg)	MDL x √ hand dose
Brookhaven	Nuclear reactor	< 20	26	0.4	1.8
Swansea	Moderated ^{252}Cf (2.2 MeV)	36	47	2.2	13.2
Birmingham	$^{3}H(^{1}H,n)^{3}He$;				
Birmingham	E_p = 1.2 MeV	50	65	2.0	14.1
	E_p = 1.05 MeV	50	65	1.2	8.5
McMaster	Nuclear reactor	43	56	2.8	18.4

* Assuming that 1.5 % of total body skeleton and skin is in one hand, and that 0.1 % of the hand dose will be delivered to the rest of the body;

Table 1.1 Performance of different methods for *in vivo* measurement of aluminum in bone.

The ^{252}Cf neutron source has a low neutron flux (2×10^5 n/cm^2 s) and interference from the fast neutron reaction with ^{31}P. A cyclic activation has been tested and an increase in the aluminum activation detected (240 s of irradiation in five cycles overall), but the detection limit was still much higher than the value of aluminum in the Reference Man hand due to the low neutron flux. To investigate the possibility of lowering the minimum detectable limit, this group has developed an irradiation cell using Monte Carlo modeling (Lewis *et al.*, 1997). Unfortunately, experimental results have not been published up to the present, although a minimum detectable limit has been estimated to reach 0.5 mg of aluminum. The advantage of this source is that it is inexpensive compared with the other proposed neutron sources, and is portable.

The final proposed neutron source, an accelerator-based source, can produce neutrons with a maximum energy below the threshold for interfering reactions and with an adequate flux for hand measurements as shown by studies at the University of Birmingham, and now at McMaster University. A further benefit of this source is that it could in principle be transported (using a mobile accelerator).

1.2 Foregoing McMaster Study of Aluminum in Humans

Since 1993, McMaster's Trace Elements Group has been involved in developing a procedure to measure aluminum levels in human bone. The first results were reported by Palerme (1993b) in a thesis entitled "Pilot Studies for *In Vivo* Bone Aluminum Measurement". Subsequent results were published by the author of this work either as the

Master's thesis titled "An Accelerator Based *In Vivo* Measurements of Aluminum in Human Bone by Neutron Activation Analysis"(1998), or as publications (Pejović-Milić *et al.*, 1998a, 1998b, 2000).

The preliminary experiments investigated the best available neutron source present at McMaster University, as well as suggesting a measurement procedure. For aluminum measurements in bone, high thermal neutron flux is desired to minimize the phosphorous interference and to maximize the activation per unit time. The fast neutron flux was calculated to be 1.1 % and 40 % of the thermal flux for two reactor beam ports, while the KN accelerator beam showed no component of fast neutrons at all. Although the KN Van de Graff accelerator has been indicated as the best neutron source for aluminum activation, due to its immediate unavailability, further experiments were conducted on the better neutron beam port in the nuclear reactor. The first step was to construct phantoms of a Reference Man hand, with varying amounts of added aluminum. After switching from a solution to a fixed, cylindrical phantom to simulate a fist, a calibration curve was generated and a minimum detectable limit for the system was calculated as 2.8 mg of aluminum. Based on the calibration line it was estimated that each phantom contains approximately 9 mg of aluminum as a contamination. The estimated dose to the subject's hand was 43 mSv (table 1.1). This set of phantoms is used and referred to as the cylindrical set of phantoms throughout this thesis.

Following these promising results and suggestions, the KN accelerator was applied as a neutron source using the same phantoms and measurement procedure. The main advantage of the accelerator compared to the nuclear reactor is that the maximum neutron energy emitted is below the threshold energy for phosphorus and silicon,

therefore eliminating the need for corrections due to the presence of these elements in the human body.

Mass spectroscopy was applied to investigate the best chemicals with which to build the hand phantoms. Unfortunately aluminum, being the third most abundant element in the Earth's crust, is hard to eliminate from other chemical compounds, and all tested compounds were contaminated. Aluminum as a trace element in the initial, cylindrical set of phantoms was measured to be 15.47 mg per phantom, predominantly originating from the bone ash. This result was of the same order of magnitude as the content calculated in the previous pilot study using the calibration line.

A new set of phantoms was built and each contained 2 mg of tracer as well, although pure calcium phosphate was used to simulate bone. Furthermore, the new set of phantoms simulated an open hand, compared to the fist, allowing for better irradiation and measurement geometry. The thinner, rectangular geometry influenced the process of aluminum activation and measurement in three different ways. One, it was feasible to move the two large surface area NaI(Tl) detectors closer, approaching 4π-geometry and increasing the solid angle. Secondly, this geometry resulted in a slight reduction of gamma ray attenuation inside the phantoms increasing the gamma signal acquired by the detectors. Lastly, there will have been less attenuation of incident neutron fluence, and thus, marginally greater activation.

Using the Anderson and Braun neutron remmeter and indium foils, the neutron dose to the hand was estimated as 9 or 6 mSv, respectively. The accompanying minimum detectable limit for the 180 s of irradiation and the 300 s of measurement time, with an approximately 30 s transport time, was 1.3 mg at 2.25 MeV with a 550 mSv/h neutron

field. Using the same procedure a minimum detectable limit for the new, flat set of phantoms was 0.7 mg of aluminum in the hand.

All of these results have initiated subsequent experiments in an attempt to further lower the minimum detectable limit in an effort to develop a procedure to measure healthy subjects with an expected 0.3 – 0.4 mg of aluminum in the hand. The next chapters will address different approaches to this goal as well as the use of microdosimetry to measure precise neutron and gamma doses that have to be delivered to the subject in order to measure aluminum levels in bone.

1.3 Why Is Aluminum Important?

Aluminum is the most abundant metallic element in the lithosphere, occurring at about 8 % by weight (Hem, 1986 as cited by Gitelman, 1989). It is largely found as aluminosilicate mineral and as clay mineral in soils. Aluminum is a strongly hydrolyzing metal and is generally insoluble in the neutral pH range, and in turn, plants and animals have had little exposure to soluble aluminum. This has played a major role in maintaining a low burden of this element in animals and most plants. However under acidic or alkaline conditions, aluminum's solubility is enhanced, increasing its amount in environmental waters. Aluminum enters water as the result of complex processes involving its release from soil, rock, and organic matter. In general, the concentrations of aluminum are low in most natural waters. But at certain times of the year and in certain regions, elevated aluminum concentrations are well documented. Strong acidic

conditions, caused by rain-borne nitric and sulfuric acid, coincide with the transport of ecologically significant concentrations of inorganic aluminum to surface waters that is toxic to plants, birds and fish (Robushkin *et al.*, 1995).

Once absorbed by plants and fish aluminum enters the human diet. Fish is just one, minor source of aluminum content in food. Little aluminum in diet is contributed by meat (pork – 0.020 mg Al / 100 g), poultry (chicken – 0.010 mg Al / 100 g), fruits (pears – 0.024; bananas – 0.039 mg Al / 100 g), vegetables (corn – 0.010; broccoli – 0.098; peas – 0.138; pickles – 0.148; spinach – 0.478 mg Al / 100 g), oils (butter – 0.025 mg Al / 100 g) and sugars. Contrary to these, the major aluminum sources are grain products (white bread – 0.233; granola – 0.376; noodles - 0.416 mg Al / 100 g), grain-based desserts (blueberry muffins – 12.8; cornbread – 40.0; pancakes – 6.9 mg Al / 100 g), processed cheese (41.1 mg Al / 100 g) and tea (0.446 mg Al / 100 g) to name some (Gitelman, 1989).

The aluminum content of foods includes that which is naturally present in plants or animals, as well as aluminum that comes from food additives and from contact with containers, cookware and wrappings. Intentional and unintentional aluminum-containing food additives have been summarized by Pennington (1988). Intentional aluminum based additives are buffers, acid-reacting ingredients in self-raising flour or corn meal, emulsifying agents for processed cheese, processing aids, et cetera. On the other hand, unintentional aluminum-containing additives may migrate from paper or food containers, glues, adhesives and rubber to food. The use of aluminum based pressure cookers, roasting pans, pots, coffee pots and foils may increase the amount of aluminum in food as well, however, the magnitude of this increase may not be of practical importance

(Pennington, 1988). Factors affecting the increase of aluminum concentration of food include the pH of food and cooking water, length of cooking time, and the presence of salt or sugar. For example, metallic aluminum is more susceptible to disintegration when in contact with acidic, basic or salty foods.

The amount of aluminum consumed per day depends on the foods selected, the preparation of these foods, and the quantity of foods that are consumed. As Pennington (1983) has estimated, the mean aluminum intakes were about 2 mg/day for infants, 6 mg/day for 2-year old children, 9 mg/day for teenage, adult and older females, and 12-14 mg/day for teenage, adult and older males in US. These values are comparable to values published by Greger and Sutherland (1997) of 2 to 25 mg/day of aluminum. The main difference is the presence of a higher quantity of grain products in Greger's estimates.

Independent of the daily intake of aluminum, the intestine in healthy subjects absorbs only a small percentage of ingested aluminum, and the kidney readily excretes what has been absorbed. Although increased levels of aluminum in bone and serum have been reported for patients ingesting large quantities of aluminum in the form of drugs (aluminum-based phosphate-binding gels and aluminum-containing antacids), the level of aluminum from food in the diet is probably not sufficient to lead to significant retention of this element (Gitelman, 1989). Nevertheless, for those individuals with impaired absorption or excretion of aluminum and/or having high dietary intake due to aluminum contamination, the possibility of aluminum toxicity from diet and/or drugs may lead to health problems.

Before discussing aluminum absorption, elimination and compartmentalization, it is interesting to address its biological function. Aluminum has major effects on the

gastrointestinal tract. It decreases absorption of a number of inorganic elements such as iron, fluoride, strontium and phosphorous, largely forming insoluble compounds with these elements (Gitelman, 1989). It also affects absorption of some organic elements like cholesterol.

Humans are constantly exposed to aluminum via the skin, lungs and gastrointestinal tract. However, these tissues serve as almost complete barriers to aluminum absorption because of the insoluble nature of most aluminum compounds.

Until recently, there was no evidence that aluminum could be absorbed through the skin, even under conditions of high exposure. This pathway of exposure has been investigated on shaved female mice, and resulted in preferential aluminum accumulation in the hippocampus of the brain (Anane *et al.*, 1995). Whether the action of shaving prior to the aluminum application made skin more permeable to the element was not determined. This issue is interesting to manufacturers of deodorants that support administration of aluminum-based antiperspirants, and its activity and efficacy to sweat glands.

Inhaled aluminum is either immediately exhaled or trapped in the pulmonary tissue and not allowed to penetrate further in the body. However, it would appear that in individuals occupationally exposed to aluminum fumes some of the aluminum enters the bloodstream (Gitelman *et al.*, 1995). The inhalation of a significant amount of aluminum via the mouth may result in absorption across the lung epithelia or deposition in the lung and further passage to the gut. In addition to absorption via the lung and/or blood system, there may also be another form of uptake in occupationally exposed people, where aluminum enters the central nervous system directly along the nasal-olfactory pathways.

The primary sensory neurons of the olfactory system are unique in that the cells are directly exposed to the external environment. They are not synaptically isolated from the neurons, which connect them to the brain (Best-Pattersen *et al.*, 1994).

Contrary to the limited number of publications about skin and lung absorption of aluminum, there are a significant number of studies discussing the element's absorption via the gastrointestinal tract. There are a number of parameters that will affect aluminum absorption in this case such as the aluminum compound or form, the amount, pH and the rate at which aluminum can be taken up, to name a few. Aluminum phosphate has been shown to be poorly absorbed due to its insoluble state. Similarly, the formation of hydroxides by a variety of aluminum compounds at the pH of the small intestine results in insoluble compounds that are, therefore, poorly absorbed. On the other hand, a compound that is associated with enhanced aluminum absorption is aluminum citrate. Citrate and aluminum form complexes, maintaining aluminum solubility in the small intestine (Exley *et al.*, 1996). In rats, approximately one hundred times as much aluminum is absorbed, when given as the citrate form, as compared to aluminum chloride salt. It has been suggested that vitamin D enhances aluminum absorption as well, besides other elements such as fluoride, lead, strontium, magnesium and zinc (Ahn *et al.*, 1995; Exley *et al.*, 1996).

Another form of aluminum exposure that is documented to increase the body aluminum is parenterally administrated aluminum. This pathway was initially recognized in uremic patients on dialysis in places where aluminum-contaminated dialysate was used. This was the setting in which aluminum systemic toxicity was first established in humans (Alfrey *et al.*, 1976). Subsequently, aluminum has been shown to be a

contaminant in other intravenous fluids. In most patients exposure to this fluid is short and aluminum concentrations are low. However, it is recognized that aluminum levels in tissues can be increased in particular groups of patients such as premature infants (Moreno *et al.*, 1994) or patients on total parenteral nutrition who have received many intravenous compounds containing aluminum (Leung, 1995).

The major pathway for the elimination of the small amount of aluminum normally absorbed is the kidney. At this time it is debated whether the amount of aluminum absorbed from oral loads may exceed the normal kidney's capability to excrete this element, which would result in some retention of aluminum. Nevertheless, it has been established that patients with compromised renal function are unable to eliminate all of the aluminum absorbed orally, resulting in increased total body burdens (Alfrey, 1980; Alfrey *et al.*, 1980). Another pathway for aluminum excretion, particularly the phosphate salts, is the feces. Ingested aluminum binds to gastrointestinal tract mucus, which ensures the removal of aluminum in the feces. The most recent evidence has suggested that biliary excretion of aluminum is the most important for a rapid clearance following a single dose of aluminum (Exley *et al.*, 1996). This finding supports evidence of the liver as an early sink for absorbed aluminum.

The tissues most affected by aluminum are bone, spleen, heart, kidney and liver (Alfrey, 1980; Alfrey *et al.*, 1980; Spencer *et al.*, 1995 as cited by Exley *et al.*, 1996), while storage organs for aluminum are bone (Exley *et al.*, 1996; Alfrey, 1980; Alfrey *et al.*, 1980) and lung (Gitelman, 1989). It is well documented that aluminum compartmentalization is changed in patients with chronic renal failure. For example, brain aluminum can be very high in patients undergoing oral or parenteral aluminum

administration. This might mean that an alteration in the blood-brain barrier in chronic renal failure allows the aluminum to be deposited in the brain in greater quantities (Exley *et al.*, 1996).

Once absorbed, aluminum is present in plasma and serum. Plasma is a transport medium, and aluminum concentration in plasma largely reflects the magnitude of the aluminum loading that is currently taking place. For estimation of the status of body aluminum probably the most reliable tissue that is reasonably available for analysis is bone (Alfrey, 1980; Alfrey *et al.*, 1980; Exley *et al.*, 1996).

Aluminum exists in the human body in trace amounts with total body aluminum being 35 to 40 mg (Alfrey, 1980). Estimates of up to 61 mg have been made (Ellis *et al.*, 1988), while ICRP 23 estimates the aluminum content of the skeleton to be only 21 mg.

The possible human toxicity of aluminum has been a matter of controversy for well over 100 years. However, the first condition accepted to be related to aluminum exposure did not occur until the 1970s, shortly after the introduction of routine dialysis therapy for patients with chronic renal failure. Dialysis encephalopathy, characterized by speech disturbance seizures and impaired cognitive function (Alfrey *et al.*, 1976; Alfrey, 1993 as cite by Flaten *et al.*, 1996), fracturing osteomalacia and microcytic hypochromic anemia (Flaten *et al.*, 1996) are recognized aluminum related diseases in this group of patients.

During the 1980s and 1990s, several reports appeared describing aluminum accumulation and toxicity in patients without chronic renal failure. These groups included preterm infants fed intravenously (Moreno *et al.*, 1994; Sedman *et al.*, 1985), patients on total parenteral nutrition (Leung, 1995), patients with severe burns (Flaten *et al.*, 1996),

and patients undergoing bone reconstruction with aluminum containing bone cement (Flaten *et al.*, 1996). Additionally one publication documented health problems caused by aluminum deposited in the bone of healthy individuals after accidentally being exposed to higher aluminum levels in the drinking water supply (Eastwood *et al.*, 1990).

A toxic role for aluminum has been suggested and vigorously debated in relation to Alzheimer's disease (AD). There is sufficient evidence to warrant further study of the role of aluminum in AD, especially in light of the public health concern regarding a higher prevalence for AD in regions with elevated aluminum concentrations in drinking water (Martyn *et al.*, 1989; McLachlan *et al.*, 1991). Another connection between aluminum and AD is the possible presence of aluminum compounds in tangles and plaques in patient's brain. Even if aluminum accumulates in tangles and plaques, it might be only a passive effect that needs further clarification within the basic pathology of the disease.

A recently published study has tested the hypotheses about the connection between stored aluminum and Alzheimer's disease. In this study trabecular bone aluminum content was measured in patients with diagnosed senile dementia of the Alzheimer type. Quantitative analysis done by atomic absorption spectrometry showed lower aluminum content (11.9±4.04 μg/g dry bone) in the patients than in the control group (18.2±7.37 μg/g dry bone) (O'Mahony *et al.*, 1995). These results imply that aluminum content in trabecular bone may not influence the disease. On the other hand, it has been suggested that there is an increasing portion of circulating, unbound aluminum in blood, which may cross the blood-brain barrier causing brain damage, and thus may originate from bone. Some previous studies have found a higher aluminum content in

trabecular bone than in cortical (Alfrey *et al.*, 1976; Lefebvre *et al.*, 1988), supporting the measurement of aluminum in trabecular bone, and further, the attempt to correlate it with the incidence of the disease.

Occupational medicine is another area of medicine that provided evidence about long-term exposure to aluminum by inhalation and its harmful neurological effects. In occupationally exposed individuals a considerable number of studies reported cognitive changes (Rifat *et at.*, 1990), and possible impairment and other neurological effects associated with exposure to aluminum dust or fumes (White *et al.*, 1992; Sjogren *et al.*, 1990; Hänninen *et al.*, 1994; Best-Pattersen *et al.*, 1994). Occupational exposure to aluminum has been associated with an increase in both urinary aluminum excretion and serum aluminum (Ljunggren *et al.*, 1990; Gitelman *et al.*, 1995; Sjogren *et al.* 1988). Recently published data indicate that the body burden threshold for adverse effects approximates a urinary aluminum value of 4 – 6 μmol per liter and an aluminum serum value of 0.25 – 0.35 μg per liter among aluminum welders (Riihimäki *et al.*, 2000). On the other hand the bone mineral content, which was determined in the lumbar spine by means of dual photon absorptiometry, showed no significant difference between exposed and non-exposed workers to aluminum powders. The bone density values in the exposed subjects were 1.00 g/cm^2 compared to 1.02 g/cm^2 in the control group (Schmid *et al.*, 1995). This work might suggest that in healthy individuals, with normal kidney function, there is no evidence of a significant change in bone density caused by aluminum deposition in the skeleton.

Aluminum toxicity is currently diagnosed through a qualitative method, namely the histochemical analysis of a bone biopsy sample taken from the iliac crest. This

invasive procedure is painful and consequently has a low patient acceptance. Because of this and the awareness of the potential increase in harmful effects due to aluminum poisoning, McMaster's Trace Element Group has developed a new, non-invasive technique to measure aluminum status using *in vivo* neutron activation analysis.

Chapter II

Accelerator Based Aluminum Activation

2.1 Experimental Design

Aluminum neutron activation of either a phantom or a subject's hand is performed using a KN-Van de Graaff accelerator, in which the production of neutrons is based on the $^{7}Li(p,n)^{7}Be$ reaction. This endothermic nuclear reaction has a Q value of 1.64 MeV, and the minimum proton energy necessary for the reaction is 1.88 MeV. It can produce neutrons with several kilo-electron volt energies, and the neutron energy is a strong function of both angle and bombarding proton energy.

Using a theoretical calculation of the maximum neutron energy of the beam at the irradiation site along the neutron beam axis (0 degrees), protons of 2.25 MeV energy on the Li-target will produce neutrons with a maximum energy of 520 keV, while protons of

2 MeV will produce neutrons with an energy not higher than 230 keV. Since a thick lithium target was used, a spectrum of neutrons was produced instead of discrete values. It should be noted at this point that the maximum neutron energy of the beam, which can be easily controlled, is a significant feature of the accelerator-based system for aluminum activation in human bone. The maximum value of 520 keV is such that the interference reactions of fast neutrons with phosphorous and silicon are not energetically permitted. This is a critical feature of the system in terms of dramatically simplifying the analysis of the aluminum measurement.

Aluminum neutron activation is a thermal reaction in which the product has a short half-life (2.25 minutes) and thus governs the experimental procedure. The general experimental protocol was constant throughout this work, and was independent of the phantoms used or the irradiation parameters. The irradiation time for the phantoms was 180 s, followed by a transfer time of usually 25-35 s, and a counting time of 300 s. The counting time of 300 s was enough to maximize the aluminum signal over the background counts.

Aluminum doped phantoms were constructed to simulate both soft tissue and bone according to the chemical composition of Reference Man cited by ICRP 23. Polyester resin was used as a substrate, to which fixed amounts of bone ash (37.53 g), NaCl (2.35 g), Na_2CO_3 (1.33 g) and varying amounts of $Al(NO_3)_3 \cdot 9H_2O$ were introduced. This set of cylindrical phantoms (76 mm diameter x 90 mm height) consisted of six phantoms corresponding to 0, 0.5, 2, 5, 20 and 50 mg of added aluminum. An additional two phantoms, consisting of the resin matrix only and resin with bone ash, were included in this set, to investigate the presence of aluminum in these two components, since the

resin and bone ash were not of high purity. As previously mentioned, the aluminum impurities were calculated as 9 mg per phantom by converting the units of slope in the calibration line, or as 15.5 mg using mass spectroscopy. The main source of aluminum contamination was the bone ash. Therefore, the second set of phantoms, the flat phantoms (22.6 x 12.4 x 2.5 cm thick), was built with similar amounts of the chemicals, but with calcium phosphate instead of bone ash. For this set ICRP 70 suggestions were followed with bone mass of 5500 g, and that the hand comprises 1.25 % of the total skeleton. This set simulated an open human hand, rather than the clenched fist like the cylindrical phantoms, and it consisted of six phantoms with 0, 0.5, 2, 5.64, 10.07 and 19.45 mg of aluminum. The lower concentration phantoms were made by adding an aluminum salt solution (1 mg per ml), while the phantoms with 5.64 mg of aluminum and above were built using $Al(NO_3)_3 \cdot 9H_2O$. Unfortunately, the phantom with 0.5 mg Al had to be rejected from the set due to an unrealistic aluminum signal that would obstruct the calibration line. Although pure chemicals were introduced, the level of aluminum impurities was still high in the phantoms.

The aluminum phantoms were irradiated at 0 degrees, inside a polyethylene cavity, which had been optimized and built earlier (Pejović-Milić, 1998). Phantoms were positioned manually in the centre of the

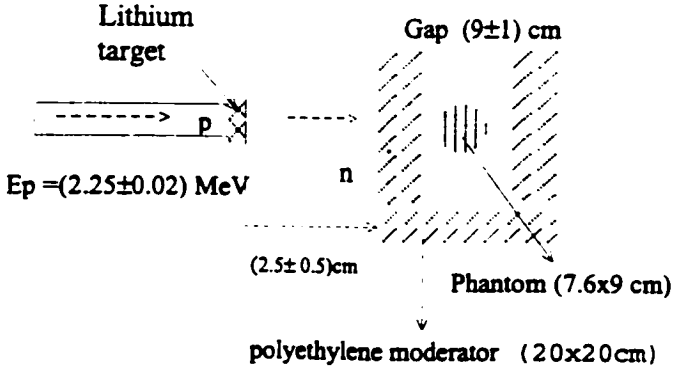

Figure 2.1 Cavity and experiment design.

irradiation cavity (fig. 2.1).

The primary purpose of the polyethylene cavity is to increase the thermal flux in the neutron beam, which is achieved in two different ways. One is the moderation of the epithermal and fast neutron components in the primary beam and the other is the simultaneous reflection and further moderation of neutrons, returning from the cavity wall.

The irradiation parameters were investigated and values were chosen to maximize aluminum activation while delivering an acceptable dose to the subject. As it will be illustrated with experimental results later, the majority of the experiments were conducted at 2.25 MeV proton energy on the Li-target, since it was believed that the delivered dose to the hand and subject was low, and therefore, at an acceptable level for a routine aluminum measurement. Unfortunately, once microdosimetry was applied for more accurate dose estimation, it was learned that the dose was significantly higher than estimated, from indium foils or an Anderson and Braun remmeter, imposing additional limits on the procedure (for further discussion refer to Section 2.3). Therefore, the final experiments, which will be presented in Section 2.4, were conducted with the proton energy lowered to 2 MeV, and using the maximum obtainable current of the KN accelerator. Alternatively, lower proton energy may be used (such as 1.95 MeV which is just above the threshold energy for the $^{7}Li(p,n)^{7}Be$ reaction) with a different irradiation time, but currently the accelerator is not as stable at lower energies.

Between September 1997 and July 1999 the KN accelerator was shut down while the FN accelerator was decommissioned, and therefore the aluminum experiments were started before, and then continued after, this time interval. During the initial experiments.

which were performed before the winter of 1997, neutron field monitoring was performed with an Anderson and Braun remmeter (Tracelab, Model NP-1 portable monitor), which was positioned in the target room at a 67.5 degree angle and 2 m distance to the neutron beam line. However, during the following experiments that began in 1999, two BF_3 tubes (Reuter-Stokes tubes) were used. The larger BF_3 detector (2.5 cm in diameter and 25 cm long) was fixed on the wall at approximately 90 degrees and several meters from the target, while the smaller BF_3 detector (2.5 cm in diameter and 10 cm long) was placed behind the irradiation cavity along the beam axis at 0 degrees. The two BF_3 detectors served as a means of control for any possible changes in the neutron field that might occur due to the melting of the lithium in the target or a change in the scattering component of the neutron field. Additionally, these detectors may serve as a means for normalization.

After irradiation and transfer, each phantom was placed in the detection system. The photon counting system was based on two large NaI(Tl) (200 mm x 50 mm thick) detectors facing each other, built in a Pb-shield environment (figure 2.2), and arranged to achieve 4π-geometry. The air gap between the detectors for the initial, cylindrical set of phantoms was 9 cm. After the flatter phantoms were built, the air gap was made smaller and set at 4 cm. Both gaps were sufficient to

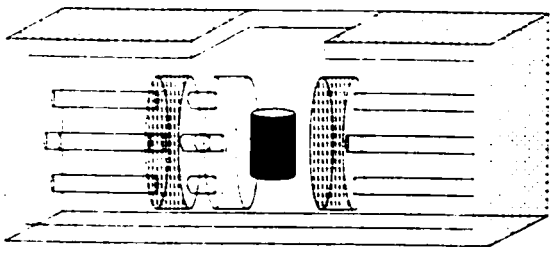

Figure 2.2 NaI(Tl) detection system.

accommodate a patient's hand for future *in vivo* measurements.

Each scintillation crystal has four photomultiplier tubes connected in parallel. The detectors are independently connected to preamplifiers (CI model 1405, serial numbers: 128231 and 48175), and then to amplifiers (Harshaw, models: Na-23 and Na-32). From both amplifiers, the signals are summed (Ortec, model 43388) and sent to a personal computer, where spectra are acquired and saved by commercial software Aptec 6.31.

As illustrated in figure 2.2, the detection system is shielded with 3 cm of lead on each side, and during the phantom measurements the lid is closed. The shield significantly decreases background by protecting the detectors from external radiation.

Figure 2.3 illustrates a typical aluminum activation spectrum for both the

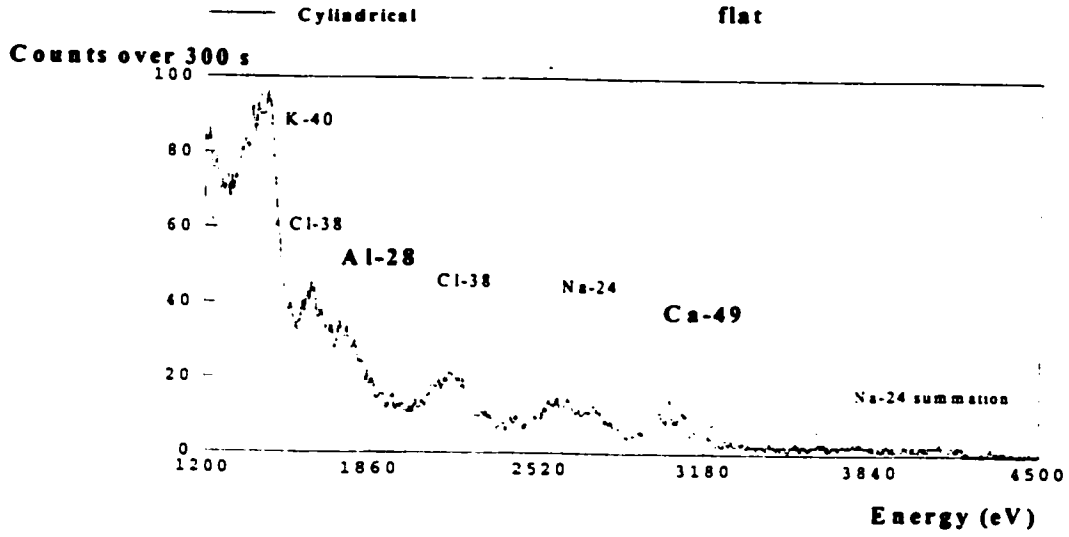

Figure 2.3 Typical spectra of cylindrical and flat phantoms acquired by two large NaI(Tl) detectors arranged in quasi 4π-geometry.

cylindrical and flat phantoms. It is important to note that a higher count rate has been achieved with the flat phantoms. Also, the summation peak for sodium at 4.1 MeV has been observed, which had not been seen before. This provides evidence that the detection efficiency has been improved, primarily from the lowering of the distance between the detectors from 9 cm to 4 cm due to the different phantom thicknesses. Additionally, the irradiation of the flat phantoms provides less attenuation of the neutrons and emitted gamma rays, as well as a lessened screening effect in the phantom itself.

Once the spectra were acquired, further analysis was done using a non-linear least-squares optimization method developed by Marquardt (Bevington, 1992). Detailed spectral analysis was published elsewhere (Pejović-Milić, 1998). In short, two separate fitting routines were applied to the aluminum and calcium characteristic peaks separately. Based on the detector response, it was determined that a single exponential function may be used to fit the background below the Gaussian peaks.

Since chlorine is present in humans and is activated with thermal neutrons, the aluminum region was fitted with two Gaussian peaks tied to one another for the chlorine (1.64 MeV) and aluminum (1.78 MeV) characteristic peaks. The next step in the fitting procedure was to reduce the number of parameters by fixing the width of the Gaussian peak. The inverse variance weighted mean of the width given by the analysis of the spectra was used, and the final data fitting was accomplished with five independent variables for the aluminum region.

As pointed out previously, the number of counts from the hand depends upon the size of hand, the irradiation and counting geometry, as well as the neutron profile. Therefore, the ratio of the aluminum to calcium signal is taken to derive the aluminum

concentration (see Section 1.1). An analogous Marquardt method, thus, was necessary for fitting the calcium peak in the spectrum. Similarly, it was decided that the width could be fixed in order to reduce the number of fitting parameters. The final equations had four parameters fitting one Gaussian peak on a single exponential background.

The amplitudes of the aluminum and calcium peaks, calculated by the Marquardt method, were then further analyzed. These amplitudes were corrected for transfer, irradiation, and counting times separately, due to the differences in the elements' half-lives, using the equation

$$C^* = \frac{\lambda C}{(1-\exp(-\lambda t_{irrad}) \cdot \exp(-\lambda t_{tranfer})(1-\exp(-\lambda t_{counting}))} \qquad \text{(equation 2.1)}$$

accompanied by an uncertainty of

$$\sigma_{C^*} = C^* \sqrt{(\frac{\sigma C}{C})^2 + (\frac{\lambda \cdot \sigma t_{irrad}}{(1-\exp(-\lambda t_{irrad})\exp(\lambda t_{irrad})})^2 + (\lambda \cdot \sigma t_{trasfer})^2} \qquad \text{(equation 2.2)}$$

The calibration lines were obtained by plotting the ratio of these corrected amplitudes (Al/Ca) versus the aluminum mass in each phantom, and then determining the regression line by a linear least-squares method. For each set of measurements, such as the data obtained with the different phantoms or by using different irradiation parameters, the minimum detectable limit (MDL) was estimated.

The minimum detectable limit is defined as twice the precision for a zero concentration measurement divided by the slope of the calibration line. This is a common definition of a lower limit of detection, set as the concentration that gives rise to a signal intensity that is twice the standard deviation of the measured intensity in the limit of low aluminum concentration. As the concentration goes to zero, the peak intensity goes to

zero and, therefore, the uncertainty in the peak intensity is determined by the uncertainty in the background counts under the peak.

2.2 Aluminum Neutron Activation Experiments

The initial set of experiments for developing a procedure for aluminum measurement in human bone using the KN accelerator was performed before 1997. At that time, the irradiation parameters and polyethylene cavity were optimized as discussed previously. It was experimentally measured and confirmed using Monte Carlo modeling (see Part I - Chapter III), that the highest aluminum activation can be achieved by positioning the cavity as close as possible to the Li-target and by using high proton energy. The KN accelerator can produce protons with energies up to 2.5 MeV, but the highest practical proton energy was determined to be 2.25 MeV. The main advantage of higher proton energy is an increase in the produced neutron yield. Therefore, 2.25 MeV has been selected as an appropriate stable proton energy that can produce a practical neutron yield at McMaster's accelerator. A second option to increase the neutron yield is by increasing the proton current incident on the target. During these experiments, the KN accelerator was capable and licensed to run up to a 50 μA proton current, limiting significantly its application for aluminum activation. Since the accelerator was unstable at higher proton currents during the 180 s irradiation time, and it was believed that the current reading was unreliable, the irradiation parameters were adjusted to produce a 550 mSv/h neutron field monitored with the Anderson and Braun neutron detector positioned

in the target room. It is necessary to emphasize that all energies reported here have an uncertainty of ±0.02 MeV, while the uncertainty associated with the current reading is approximately 10%.

The performance in terms of MDL for the cylindrical phantoms was 1.3 mg, while the MDL for the flat phantoms was 0.7 mg of aluminum.

The following aluminum activation experiments were conducted in 1999, after servicing of the beam line and some adjustments in target cooling. Following beam characterization, the aluminum activation experiments were repeated using the previously defined irradiation parameters. Now the cooling system allowed a proton current on the target of up to 120 μA. Therefore, at a proton energy of 2.25 MeV, two different sets of experiments have been performed using the cylindrical set of phantoms, one at 36 μA and

Aluminum mass (mg)	Al/Ca ratio Low Current Experiment		Al/Ca ratio High Current Experiment	
50±0.03	2.147±0.095	1.868±0.076	1.843±0.039	1.765±0.036
20±0.03	0.992±0.043	1.035±0.043	0.959±0.023	1.013±0.024
5±0.03	0.719±0.051	0.685±0.041	0.629±0.018	0.615±0.017
2	0.589±0.037	0.658±0.057	0.557±0.017	0.523±0.016
0.5	0.636±0.047	0.715±0.045	0.552±0.018	0.507±0.016
0	0.563±0.036	0.572±0.037	0.484±0.016	0.485±0.015

Table 2.1 Aluminum to calcium ratio for the cylindrical set of phantoms measured at 2.25 MeV and at 36 μA (low current experiment) and 110 μA (high current experiment) proton current.

the second at 110 μA, in an attempt to investigate the irradiation parameters further. Table 2.1 shows the experimental results of the two, low and high current experiments. As explained earlier, the calibration curve was obtained by plotting the ratio of amplitudes (Al/Ca) versus aluminum concentration. The regression line ($R^2 = 0.98$) for the cylindrical set of phantoms at low proton current was as follows

$$Al/Ca = (0.587 \pm 0.02) + (0.025 \pm 0.001)Al \qquad \text{(equation 2.3)}$$

while for the high current experiment the regression line ($R^2 = 0.99$) was

$$Al/Ca = (0.487 \pm 0.02) + (0.026 \pm 0.001)Al \qquad \text{(equation 2.4)}$$

The accompanying minimum detectable limits were 2.9 mg and 1.2 mg of aluminum, respectively. As expected, the system performance was reproduced. Thus, it was anticipated that with the application of additional approaches to increase the aluminum sensitivity, it might be feasible to reach the level of aluminum present in a healthy subject's hand of 0.2 – 0.3 mg.

2.3 Dosimetry for Aluminum Hand Measurement

Prior to the application of the procedure on humans, further experiments were performed including the construction of a new, modeled irradiation cavity (see Part I-Chapter III) and detailed dosimetry measurements. The dose delivered to a patient's hand during a routine aluminum measurement is made up of the energy deposition of different types of radiation such as neutrons, gamma rays, recoil protons and decay of radioactive atoms.

The neutron dose depends on the incident neutron energy since the radiation weighting factor for neutrons also depends on energy. The reactions induced in the hand by the thermal neutrons are $^{1}H(n,\gamma)^{2}H$, $^{14}N(n,p)^{14}C$, $^{35}Cl(n,\gamma)^{36}Cl$, and $^{23}Na(n,\gamma)^{24}Na$.

The dominant damaging effect results from the neutron activation of nitrogen atoms. There are a few processes contributing to the dose from this reaction: the production and recoil of protons, and decay of the ^{14}C atoms, each contributing to the thermal dose at different levels. Another process is proton recoil that dominates in the case of fast neutron dose. On the other hand, the dose delivered by the gamma rays from neutron reactions with hydrogen, chlorine and sodium is insignificant, because the hand has a thin layer of soft tissue and rather small and thin bones, meaning that almost all of the gamma rays will escape from the hand before making energy deposition. Also, gamma rays have the smallest radiation weighting factor with a value of 1. The dose from the decay of the carbon and sodium atoms is negligible compared with the dose deposited by the protons. It should be noted that the dose from thermal neutrons comes from a mixture of low (γ) and high (p, ^{14}C recoil) LET types of radiation.

The thermal neutron flux within the polyethylene irradiation cavity was measured using an ^{115}In foil (1 x 1 cm) via the thermal neutron reaction $^{115}In(n,\gamma)^{116}In$. The indium samples were very thin foils (1 x 1 cm) made from an indium wire (95.7 % ^{115}In and 4.3 % ^{113}In). $^{116m2}In$, with a short half-life, decays during the transfer time of 30 s, but the $^{116m1}In$ spectra (half-life of 54.1 min) were successfully acquired for 30 min. There are a number of γ rays emitted by the $^{116m1}In$ isotope, with the peaks of the greatest intensity being 1.293 (85 %), 1.097 (55.7 %), 0.818 (11.6 %) and 0.416 MeV (32.4 %). The area of the 1.293 MeV peak, originating from the de-excitation from the first excited state to the ground level, was used for further dose estimation because of its large intensity. These flux measurements allow only an estimate of the thermal dose delivered to the subject's hand during the irradiation, using the fluence to dose equivalent conversion

factor from ICRP 21 (1971). For thermal neutrons, a flux density of 26 n/cm^2/s converts to a dose equivalent of 1 μSv/h.

The indium foils were positioned inside the polyethylene irradiation cavity on the front face of the reflector wall. During the initial experiments, the flux measurements were conducted for a beam energy of 2.25 MeV, with a neutron field of 550 mSv/h on the standard Snoopy, and at a distance of 2.5 cm from the target. For the given experimental setup, the measured average thermal flux density was $(3.3\pm0.2)10^6$ n/cm^2/s converting to a 6.34 mSv hand dose during the 180 s of irradiation.

Two beam energies were investigated again, once the KN accelerator was ready for aluminum experiments after the shutdown: 2.00 (current of 43 μA) and 2.25 MeV (current of 38 μA). The measured averaged thermal flux densities in the cavity were $(2.85\pm0.05)10^6$ n/cm^2/s and $(5.9\pm0.1)10^6$ n/cm^2/s, estimating the thermal neutron doses to the hand as 5.5 mSv and 11.3 mSv, respectively. It also can be seen from the indium activation data that the thermal flux density per unit current doubles if the proton energy increases from 2 to 2.25 MeV.

Complementary dosimetry measurements were completed using the Anderson and Braun neutron remmeter (Tracelab, Model NP-1 portable monitor), colloquially named a Snoopy. The monitor consists of a unique polyethylene moderator / attenuator assembly, BF_3 detector, and associated electronics used to convert the detector pulse output to a meter reading and recorder / scaler signal. The scaler output is useful if integrated dose information rather than dose rate is desired, as in this experiment, and if accurate measurements at very low count rates are required.

During the course of this work, measurements were done at a beam energy of 2.25 MeV, along the beam axis. Due to the difference in size between the cavity and Snoopy, it was only possible to use part of the cavity, namely the polyethylene moderator. This eliminated a scattering component of neutrons from the back and side walls of the cavity, and therefore, the dose measurements were expected to underestimate the dose. Furthermore, the remmeter is sensitive to position orientation. It was previously determined which orientation gives the best sensitivity in the neutron field used (several hundred kilo-electron volts). The sensitivity was 4900 counts per mrem (Pejović-Milić, 1998). An additional limitation was that there are problems with the Snoopy detector in mixed, non-isotropic neutron fields (Rogers, 1979). Nevertheless, the hand dose would be 9.29 mSv at 2.25 MeV for an aluminum measurement of 180 s at 2.5 cm distance from the target as measured in 1996.

After the KN shutdown, similar dosimetry measurements were repeated. It was noted that, due to the detector's saturation, the dose couldn't be estimated at short distances and at high currents. Since it was believed that the dose associated with the aluminum measurement was low, and therefore, an important advantage of this procedure, it was necessary to investigate the dose estimations of 1996 and 2000 more carefully.

A set of Snoopy measurement was performed for a bare neutron beam at greater distances from the lithium target, and further to compare the results, measurements were scaled for the incident proton energy and current. A dose of 0.193 mSv/μA at 50 cm distance and 2.25 MeV was measured in 2000, while (assuming a $1/r^2$ relation between dose and distance) a dose of 0.19 mSv/μA was estimated for the same distance and

proton energy in 1996. Under this condition it was believed that the detector runs well below its saturation, and the neutron beam was covering the whole Snoopy volume, eliminating the need for an area correction. Unfortunately, a similar comparison was not done at shorter distances, since the detector was not able to handle a high count rate.

It was learned that the Snoopy detector saturates at high count rates of approximately 30 000 count per minute (Sokolowski, 1989), and once a dead time correction is incorporated into the dose of 9.29 mSv at 2.25 MeV (a factor of 1.77), the hand dose inside the polyethylene cavity becomes almost 17 mSv.

The dose delivered to the hand is closely associated with many parameters such as the incident proton energy, irradiation time, irradiation cavity design, and neutron yield, to name a few. The use of microdosimetric counters gives detailed information about the neutron and photon dose, and also provides a precise measurement of absorbed dose. Neutron microdosimetry measures the deposited energy, linear energy density and, hence, the quality factor. Detailed microdosimetry measurements were conducted for the bare neutron beam between 0 and 90 degree angles, and for different beam energies, as well as inside the polyethylene cavity (Arnold, 2000). A spherical 0.5" diameter Rossi counter (Far West Technology, serial # 1156; borrowed from Dr. A. J. Waker's research group at AECL laboratories in Chalk River) filled with propane based tissue equivalent gas was used.

Microdosimetry measurements were taken in the centre of the polyethylene cavity and at its edges (± 7 cm from the centre), for beam energies of 2 and 2.25 MeV at 0 degrees and 2.5 cm distance from the Li-target.

Not surprisingly, the measured total dose delivered to the hand, originating from neutrons and gamma rays, is higher than the dose estimated using either indium foils or the Snoopy. The thermal neutron flux contributes 15.2 % of the neutron dose and 14.8 % of the total dose for 2.25 MeV, and 35.4 % and 30.4 % for 2 MeV proton energy (Arnold, 2000). Also, it has been learned that up to 30 % of the total dose within the cavity comes from gamma rays that are predominantly emitted when thermal neutrons interact with hydrogen in the polyethylene. It is estimated that 78.6 mSv and 240 mSv would be delivered to the hand during 180 s of aluminum activation at 2.25 MeV during low and high current activation (see Part I - Sec. 2.2), respectively. The comparable dose at 2 MeV and 115 μA would be of the order of 48 mSv to the hand.

Knowing that microdosimetry measurements measure the total dose during the procedure while the Snoopy measures only the neutron dose, it was expected that the two would differ. An additional problem arises with Snoopy readings, which are unreliable in mixed, unidirectional neutron fields such as the KN field, somewhat offsetting the dose estimations even more. Nevertheless, an effort was made to find a correlation between the microdosimetry and Snoopy dose estimations. Snoopy and microdosimetry measurements were conducted under identical experimental conditions, 10 cm from the target, and it was found that microdosimetry was greater than Snoopy by a factor of 1.4. Note, this factor was less at 50 cm, and therefore, would be expected to be larger at 2.5 cm (due to the greater area correction required as less of the Snoopy volume is in the direct neutron field). Nevertheless, it was assumed that this factor of 1.4 could be used inside the hand cavity – implying that Snoopy would give a dose of 59.26 mSv for the microdosimetry dose of 78.6 mSv (2.25 MeV, 36 μA). However, in addition indium foil

measurements conducted for both the 1998 and 2000, show that the thermal flux (and, thus, the neutron field) differed by a factor of approximately two for the original Snoopy and current microdosimetry measurements. Thus, under the same conditions used in 1998, it is predicted that a Snoopy measurement would be 33 mSv. In summary, the Snoopy measurement from 1998 is roughly half of what it is predicted Snoopy would read now (estimated by making a number of corrections to a set of microdosimetry measurements taken at the center of the hand cavity).

The hand dose, estimated using microdosimetry, that would be delivered to the subject under any suggested conditions at 2.25 MeV is very high, and therefore, unacceptable for a diagnostic procedure. These findings have led to the revision of the irradiation parameters for the aluminum procedure.

2.4 Optimal Procedure for Aluminum Activation Using a KN Accelerator

In spite of the discouraging results that the hand dose delivered during aluminum measurements at 2.25 MeV is high, even though better aluminum activation is achieved at that proton energy, searches for optimal irradiation parameters have been continued. Due to the need to lower the hand dose to approximately 50 mSv for a routine measurement, and still to be able to measure aluminum in the bone using the KN accelerator, the incident proton energy was lowered to 2 MeV, accompanied by the maximum increase of the proton current to 115 μA, while keeping the irradiation time of 180 s and the distance of 2.5 cm between the Li-target and the designed polyethylene

cavity. These parameters provide higher thermal flux, and therefore, aluminum activation, than the other combination of parameters such as keeping the 2.25 MeV proton energy while shortening the irradiation time to 30 s, with the same distance, cavity and hand dose. The dose per unit current increases by a factor of 4.5 (Arnold, 2000), while the thermal flux only doubles as the beam energy is increased from 2 to 2.25 MeV.

Aluminum mass (mg)	Al/Ca ratio	Al/Ca ratio
19.44±0.03	1.130±0.030	1.147±0.032
10.08±0.03	0.826±0.025	0.817±0.032
5.64±0.03	0.657±0.022	0.625±0.024
2	0.574±0.020	0.531±0.021
0	0.495±0.018	0.530±0.019

Table 2.2 Aluminum to calcium ratio for the flat set of phantoms measured at 2 MeV and 115 μA.

The results obtained with these irradiation parameters using the flat set of phantoms are presented in table 2.2.

The minimum detectable limit (MDL) of 1.14 mg of aluminum was obtained, with a 48.3 mSv dose delivered to the hand. Even after correction for the estimated quantity of aluminum that is present in each phantom as an impurity, some trace levels of aluminum remain undiscovered, since the intercept of the calibration line is above zero and not within uncertainty of zero.

Even though these results are obtained using the optimal combination of parameters for the KN accelerator as the neutron source, the estimated MDL is well above the normal concentration of aluminum in the hand. However, the developed procedure is a suitable means of screening patients with significantly elevated levels, which can be up to 50 times the normal level, as found in patients with renal failure (Ellis *et al.*, 1988, Wyatt *et al.*, 1993a and 1993b).

Chapter III

Monte Carlo Design Study of Irradiation Cavity For *In Vivo* Aluminum Bone Measurement

A main reason for the lack of understanding of the correlation between aluminum exposure and different diseases is that there is not yet available an *in vivo*, non-invasive technique for aluminum body burden measurement that is sensitive enough to see aluminum levels in healthy subjects, or one which is widely available.

This has motivated further investigations using Monte Carlo modeling to improve the present aluminum measurement procedure previously proposed (Part I-Sec. 2.4). The MCNP code was used to produce a computer model of the present aluminum irradiation cavity and then, subsequently, to investigate the appropriate materials and dimensions of a new moderator/reflector assembly.

The computational technique used in the design of the new irradiation cavity is a coupled neutron - photon Monte Carlo transport code, called Monte Carlo for neutron and photon transport (version 4b2), which has been used widely for many years and by many researchers. The MCNP version used in this study was installed and run on a personal computer.

Neutron energies were tallied following the US National Bureau of Standard recommendation that thermal neutrons are those with energy below 0.5 eV, epithermals are inside the energy range of 0.5 eV to 10 keV, and fast neutrons are those with energies above 10 keV. In some cases, particularly those involving dose calculations, more detailed neutron energy spectra were recorded.

Theoretical modeling was used to examine the behavior of neutrons (and photons) of different energies in many materials depending on the part of the irradiation cavity being investigated. Materials of different shapes and dimensions were modeled, and the emerging neutrons and/or photons produced were studied for that material's ability to maximize the number of thermal neutrons while minimizing epithermal and fast neutron components, and coupled photon production. As the design progressed, MCNP was run to model two or more materials joined together.

The general design aim was to maximize the thermal neutron flux available to activate aluminum while delivering as low a dose as possible. This required that the epithermal and fast neutron components be minimized and that photon production, from neutron interactions in the materials used, also be kept to a minimum. Activation was assessed as realistically as possible by modeling the flat phantom used in the experiments (22.6 x 12.4 x 2 cm width) containing 20 mg of aluminum. Other elements, such as Na,

Cl, and Ca, were present in the hand phantom at normal physiological concentrations, and the phantom density was measured to be 1.2 g cm^{-3}. If a detector had been used at the irradiation site, rather than the hand phantom, conclusions may have been slightly different due to the neglecting of neutrons thermalized inside the phantom or later the hand, and omitting the small probability of aluminum activation with neutron energies other than thermal ones. The number of particles run was such that the relative uncertainty was less that 5 %.

The first step was to develop a source card simulating the accelerator beam line, with the ^{7}Li target.

3.1 Source Card

Based on published cross section data (Liskien and Paulsen, 1975) and stopping powers (Nuclear Data Tables, 1960), properties of the $^{7}Li(p,n)^{7}Be$ reaction were calculated analytically (Arnold, 2000). In particular, calculations were done to determine the neutron yield for various incident proton energies, the angular neutron yield for each proton energy (table 3.1) and the neutron spectra for various angles for each beam energy. A different source card was derived for each desired proton beam energy, with the angular neutron yields (entered in MCNP as a probability function) defining the starting direction of the source neutrons. Once a direction was chosen the corresponding neutron spectrum was used to determine the neutron energy. In this fashion, the source

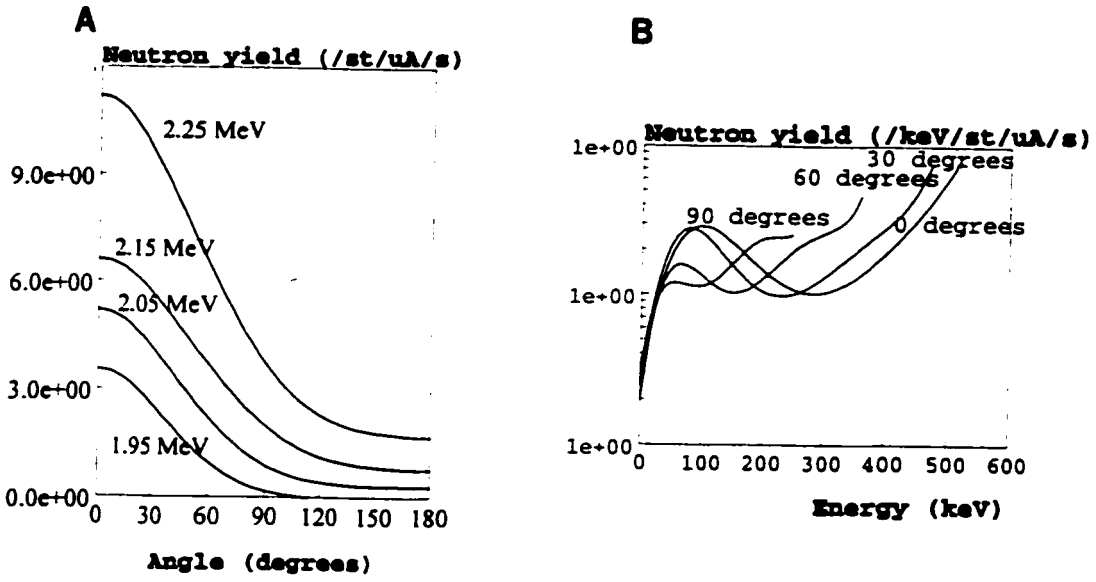

Figure 3.1 Source card information: (a) the neutron angular distribution of neutron yield and (b) the angular spectra for a beam energy of 2.25 MeV (Arnold, 2000).

neutrons modeled the actual spatial and energy distribution of neutrons advancing from the KN accelerator.

Figure 3.1 illustrates the neutron yield as a function of angle and neutron energy spectra at various angles. As can be seen, the beam of 2.25 MeV is more forward directed and has maximum neutron energy of approximately 520 keV; the maximum neutron energy emerging from the target when irradiated with 2 MeV is 230 keV.

3.2 Proton Energy and Positioning of Irradiation Cavity

After a proper source card had been developed and tested, it was used to determine the proton energy that should be used on the ^{7}Li target to produce the highest

thermal flux and aluminum activation in the irradiation site. The KN accelerator presently may be run at proton energies between 1.95 and 2.25 MeV and, thus, source cards with proton energies of 1.95, 2.00, 2.05, 2.10, 2.15, 2.20 and 2.25 MeV were produced. As discussed previously, the KN accelerator has an upper practical limit on proton energy of 2.25 MeV and a lower limit of 1.95 MeV, although it is rather unstable at this lower energy.

At this step a simple geometry was modeled consisting of a polyethylene cylinder (radius 13 cm and thickness 2 cm) as a moderator, placed between the KN source and a hand phantom in the air, each 1 cm apart. Polyethylene was chosen as the moderator based on previous experiments and, as it will be shown later, MCNP modeling confirmed this choice.

The KN accelerator produces a narrow neutron beam that diverges rapidly with increase in distance. The highest thermal flux was achieved if the moderator/reflector assembly was placed close to the target. On the other hand, if it was placed too close only small parts of the hand would be irradiated due to the very narrow neutron beam.

Proton Energy (MeV)	Relative Yield to Yield at 2.25 MeV	Corrected yield (n/s/μA)	Neutron maximum energy (keV)
1.95	0.23	7.9E+07	165
2.00	0.32	1.2E+08	230
2.05	0.40	1.5E+08	290
2.10	0.48	1.9E+08	350
2.15	0.58	2.4E+08	405
2.20	0.74	3.2E+08	460
2.25	1.00	4.3E+08	520

Table 3.1 Relative and corrected neutron yields produced at different proton energies (0° – 90° only).

Experiments implied that aluminum activation decreases as the distance between the ^{7}Li-target and the irradiation cavity increases, and that optimal aluminum activation may be achieved if the moderator surface is placed as close as possible to the ^{7}Li-target. To investigate this more closely, the spatial distribution of the neutron flux inside the hand phantom was tallied for increasing distances between the source and the moderator surface, using the same geometry as explained above. MCNP provides tally data with units of per source neutron and, thus, the total neutron yield is needed to compare results between different proton energies, as presented in table 3.1.

Modeling of the optimum proton energy to be used for aluminum activation in bone was done to test experimental observations. Activation in the 20 mg aluminum hand phantom was tallied, as shown in figure 3.2, and after correcting for the relative neutron yield at different proton energies (table 3.1), modeling results showed that the highest activation is achieved for a proton energy of 2.25 MeV on the ^{7}Li-target.

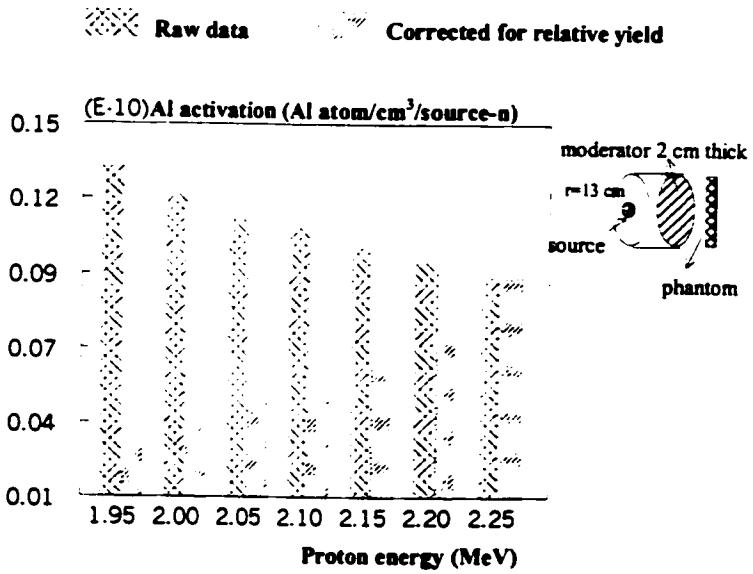

Figure 3.2 Activation of the 20 mg aluminum hand phantom with different proton energies incident on the ^{7}Li target, including data corrected for the relative neutron yields. Modeled geometry is shown in the corner.

The percentages of aluminum activation in the hand phantom

compared to the activation at 2.25 MeV are 78 % and 32 % for the proton energies 2.20 and 1.95 MeV, respectively. This supports the experimental observation (Pejović-Milić, 1998), that an increase in the proton energy gives better aluminum activation with the polyethylene moderator due to an increase in the yield. Therefore, neutron activation of aluminum with the KN accelerator should be conducted with 2.25 MeV protons incident on the ^{7}Li-target, if the only concern is optimal activation.

Knowing that the accelerator produces a small diameter beam that diverges with increasing distance from the target, it was necessary to determine the best distance between the neutron source and the irradiation cavity. Therefore, activation of the phantom and the spatial distribution of the thermal neutron flux inside it were modeled for various distances. The spatial distribution was calculated using point detectors with a radius of 0.5 cm placed entirely inside the phantom. Since the source distribution and

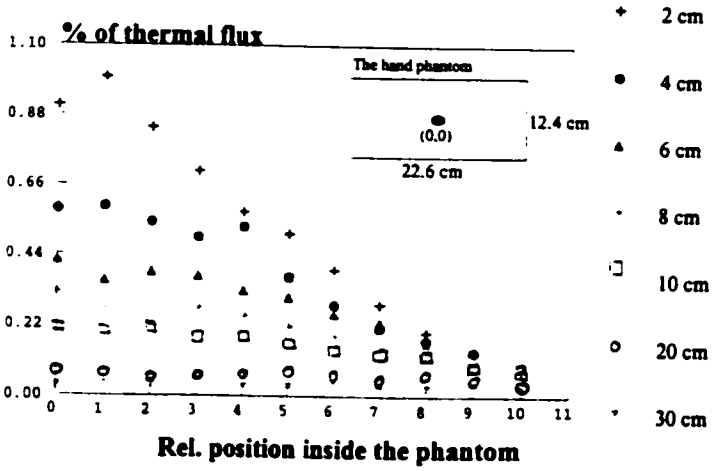

Figure 3.3 Spatial distribution of thermal flux inside the hand phantom with increasing distance between the source and the moderator surface. % of thermal neutrons to the thermal neutrons at 2 cm and at the centre of the phantom (0,0 position). Note that the source distribution is symmetrical, and therefore, only the neutron flux along the longer side of the phantom was sampled.

developed source cards are symmetrical, only the neutron flux along the longer side of the phantom was monitored, and the results are shown in figure 3.3.

Aluminum activation integrated over the whole hand phantom decreases to 56 % and 16 % at distances of 6 and 20 cm, respectively, compared to that at a distance of 2 cm. On the other hand, if the percentage of thermal flux to the thermal flux at 2 cm (in the centre of the phantom (position (0,0)) is followed (figure 3.3), better uniformity of thermal flux is achieved for the farther distances.

Due to the cooling system presently used around the ^{7}Li target, the closest position is about 2.5 cm, and therefore, the new irradiation cavity should be built to accommodate distances up to 6 cm, until the best compromise between intensity and uniformity is determined experimentally.

3.3 Cavity Design for a Proton Energy of 2.25 MeV

3.3.1 Moderator

Knowing that the KN-beam has a lower yield and a much softer energy spectrum than a reactor, the moderator material for the accelerator should have a low atomic number, a large scattering cross section for neutrons, be compact, and preferably be without gamma production (Yanch *et al.*, 1992). The material used for moderating epithermal and fast neutrons should be chosen such that it will increase the number of thermal neutrons, which is the goal of this modeling. Possible materials are heavy and light water, polyethylene, graphite and beryllium.

A moderator cylinder with a radius of 13 cm and with the two thicknesses, 2 and 5 cm, and at two proton energies, 1.95 and 2.25 MeV, was modeled in the air. A radius of 13 cm is the minimum required to cover the entire hand. The neutron beam was directed at the centre of the front surface of the moderator.

Having selected a moderator material, its optimal dimensions were investigated. Firstly, keeping a constant radius of 13 cm, the optimal thickness was sampled. Secondly, different radii (between 13 and 20 cm) were tested with the fixed optimal moderator thickness.

To select a moderator material, aluminum activation and the spatial distribution of the neutron flux were tallied in the 20 mg phantom. As may be seen in figure 3.4, for a moderator thickness of 2 cm, polyethylene provided the highest aluminum activation in the phantom. Alternatively, if the moderator thickness was 5 cm, light water produced the highest activation and presented the best choice as the moderator material. The aluminum activation with 5 cm of water at 2.25 MeV

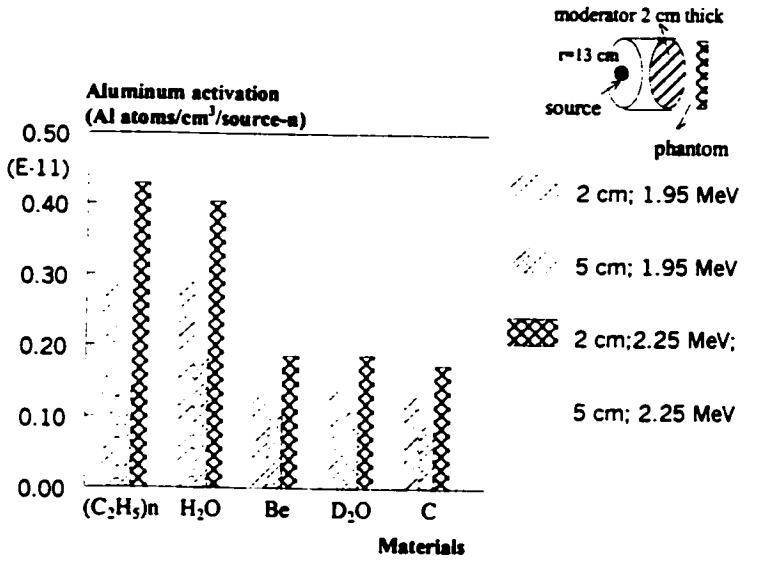

Figure 3.4 Aluminum activation of the 20 mg hand phantom for different moderator materials. Data were obtained using either 2 or 5 cm thick cylinders with 13 cm radius for each material.

is 63 % of that with the 2 cm of polyethylene at the same proton energy. Both materials have the disadvantage of inducing γ-ray production, namely 2.2 MeV γ-rays from the $^{1}H(n,\gamma)^{2}H$ reaction. This implied the need for specific γ-ray shielding as part of the overall assembly.

Since it produced the highest activation and is easy to work with, polyethylene was chosen as the moderator material. It is valuable to note that the same conclusion may be reached using the spatial thermal flux distribution inside the phantom instead of aluminum activation.

As the dimensions of the polyethylene moderator were changed, different neutron spectra and intensities on the hand were produced. Figure 3.5 presents the contribution from each component of the neutron flux on the hand phantom as a function of moderator thickness. The KN source was positioned at one end of the cylinder along the central axis, while the thickness of the cylinder was increased up to 6 cm, and the neutron flux was calculated in the phantom (at (0,0) position), which was

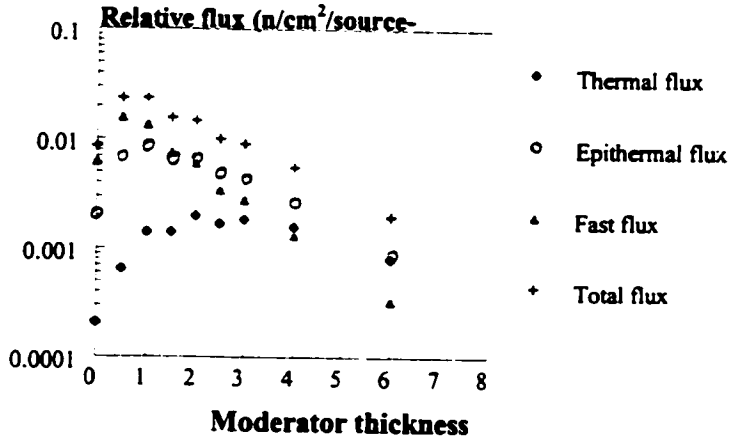

Figure 3.5 Neutron flux at the center of the hand phantom for different moderator thickness with a constant radius of 13 cm. The neutron flux was calculated inside the hand phantom using a point detector with a radius of 0.5 cm. The modeled geometry is the same as in figure 3.4, with varied moderator thickness.

placed on the opposite side from the source. As expected based on experiments, the relative thermal flux reaches its maximum value at a thickness of 2 to 3 cm of polyethylene. It is interesting to note that the thermal flux as a proportion of the total flux increases with increasing moderator thickness, implying a reduction in dose. For example, epithermal and fast components contribute to the total neutron flux with 45.4 % and 41.2 % respectively, if 2 cm of polyethylene is used. On the other hand, their contributions considerably decrease with increased moderator thickness, to 42.2 % and 16 % with 6 cm of polyethylene. However, the absolute value of the thermal flux falls, which would lead to reduced activation and a worse detection limit. Given that the hand does not contain particularly radiosensitive tissues, and that the aim of this design study was to produce as low a detection limit as possible, a 2 cm thick polyethylene moderator was chosen.

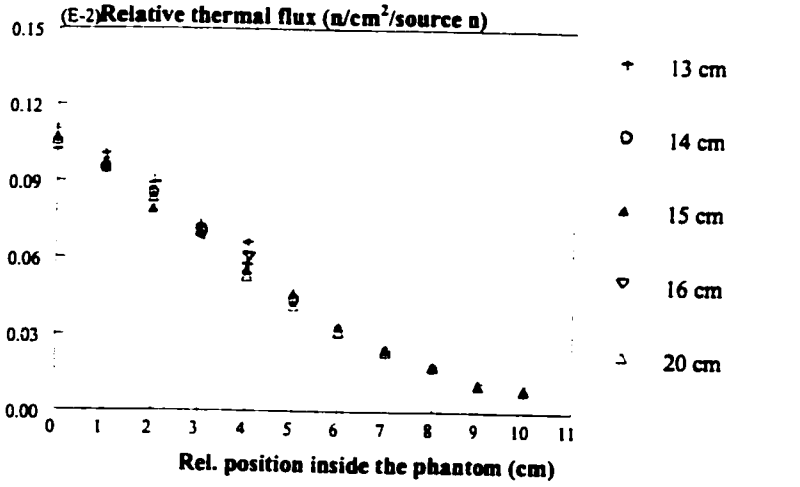

Figure 3.6 Effect of moderator radius on the neutron flux, with a fixed moderator thickness of 2 cm. The neutron flux was sampled in the hand phantom using point detectors of radius 0.5 cm.

The last step in the moderator design was to determine the moderator radius, and it was found that there was no significant change in the thermal flux in the hand phantom

for radii between 13 and 20 cm, for a constant polyethylene thickness of 2 cm. The spatial distribution of thermal flux inside the hand phantom, presented in figure 3.6, as well as aluminum activation (data not shown), illustrate this conclusion as the moderator radius increased.

As stated previously, a minimum of 13 cm is necessary to cover the open hand or phantom surface completely, thus these results imply that a 13 cm radius moderator effectively scatters back into the phantom all neutrons. The thermal flux at the edge of the phantom drops to approximately 10 % of the thermal flux at the centre, and interestingly, this effect is independent of the moderator radius. These data suggest that the number of thermal neutrons reaching the hand phantom saturates at a radial thickness below 13 cm, and therefore, this radius provides enough material to scatter back thermal neutrons into the forward direction and into the phantom. An increase in the moderator radius would unnecessarily enlarge the irradiation cavity, since the number of neutrons that would interact with the other portion of the moderator would be too small to cause a noticeable increase in the number of neutrons scattered back into the hand as thermal neutrons. Adding a reflector material around the moderator will better scatter neutrons back, increasing their chance of thermalization. This has led to the conclusion that a polyethylene cylinder with a radius of 13 cm and a thickness of 2 cm, should be introduced between the neutron source and the hand to increase the thermal flux.

3.3.2 Filter for Epithermal and Fast Neutrons

Even after moderating with polyethylene, the epithermal and fast neutron fluxes to the total neutron flux unnecessarily increase the hand dose. Therefore, it was proposed that these components could be removed from the beam by a material acting as a filter, which preferentially passes thermal neutrons while absorbing those in the epithermal and fast neutrons. Examples of such filters previously used in the design of an accelerator based boron neutron capture therapy facility are aluminum, aluminum oxide, sulfur, silicon and iron (Yanch *et al.*, 1992). In this case, aluminum and aluminum oxide filters could preferentially diminish aluminum activation in the hand.

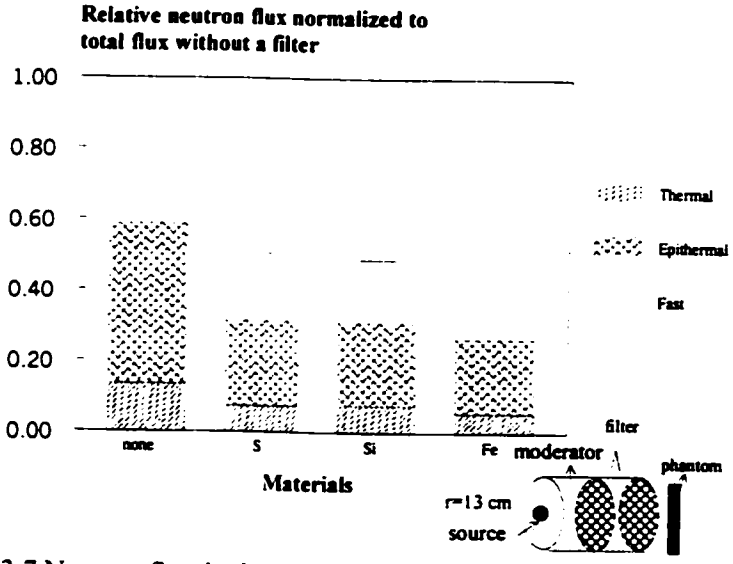

Figure 3.7 Neutron flux in the centre of the hand phantom with different filter materials. Data were obtained using both a 2 cm thick moderator and filter cylinder, with 13 cm radius. The modeled geometry is shown as well.

The modeled geometry consisted of the moderator (2 cm width) and filter (2 cm width) cylinders, each with a radius of 13 cm, adjacent to each other and placed between the source and the hand phantom, each of which was centred on the cylinder's central axis.

The modeled geometry and corresponding results normalized to the total neutron flux without filter are shown in figure 3.7. All filter materials reduced the fast and epithermal component, compared to when no filter is introduced. The largest decrease of fast neutrons, a factor of 2.6, is obtained with iron, compared to 2.3 for silicon and sulfur. A similar decrease is noticed in the epithermal region as well. However, they all also reduced the thermal neutron flux, leading to a reduction in activation. For example, the thermal flux with Si and S filters decreased by a factor of 1.85 compared to a decrease of 2.6 with iron.

Besides monitoring a change in the neutron spectrum, photon production was investigated as well, due to a possible increase in the photon dose. The photon flux was sampled over the hand phantom, and it was found that the highest photon production occurred for iron followed by sulfur and silicon, and the lowest photon flux was noticed if no filter was introduced.

In conclusion, all filter materials resulted in increased photon production, somewhat offsetting any dosimetric advantage gained by a reduction in the fast neutron component. It was concluded that none of these filters would confer an advantage on the irradiation system.

3.3.3 Reflector

To improve the yield of thermal neutrons at the irradiation site by scattering the epithermal and fast neutrons back into the moderator, a reflector material should be added to the cavity design. The preferred reflector material has to have low gamma production,

and to avoid large neutron energy losses and to ensure maximum scattering of neutrons back in the moderator. Possible materials are lead, graphite, bismuth and alumina.

Previous literature suggested that lead, graphite and alumina are similar in their reflective properties while bismuth is less reflecting (Yanch *et al.*, 1992). For the purpose of this study only lead and graphite were modeled, as they are readily available in our laboratory. In addition, other materials more accepted as moderators than reflectors were considered. The idea was to investigate if the simultaneous moderation and reflection of neutrons, scattered back by a reflector placed behind the hand rather than just around the moderator, would increase the thermal flux at the irradiation site. Thus water, heavy water, beryllium and polyethylene were considered as well.

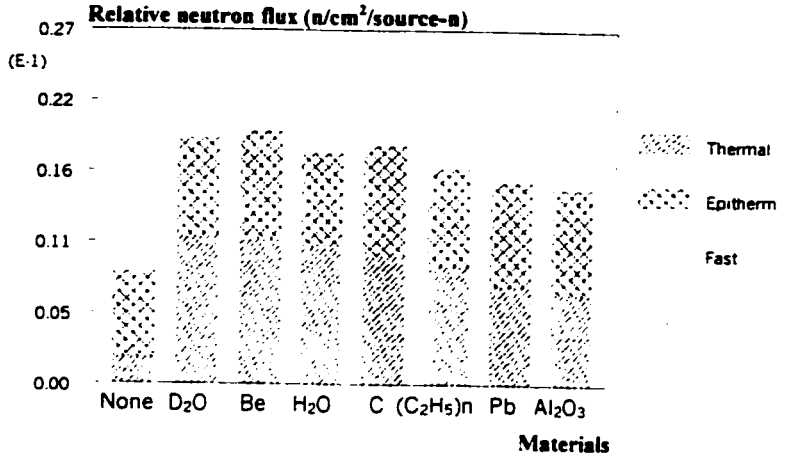

Figure 3.8 Investigating suitable reflector materials by tallying the neutron fluxes over a point detector (0.5 cm radius) placed in the centre in the hand phantom aligned with the neutron source.

The geometry modeled at this step included the adopted dimensions of the polyethylene moderator, as already discussed. and the hand phantom. surrounded by a cube of side 50 cm, hollowed out to allow for insertion of the hand and moderator. Thermal, epithermal and fast neutrons were tallied in a detector (0.5 cm radius) placed at

the centre of the hand. The relative neutron flux over the hand phantom was tallied, divided into thermal, epithermal and fast energy regions.

A comparison of reflector materials is presented in figure 3.8, from which it is seen that heavy water and beryllium produce the highest thermal neutron flux, closely followed by light water and graphite. Another consideration was that lead produced the smallest photon flux, followed by graphite, alumina, heavy water, beryllium, polyethylene and finally water. Given also that beryllium is toxic and heavy or light water inconvenient to handle, graphite emerged as the best overall material for the reflector.

Next, the dimensions of the graphite reflector were evaluated by varying the thickness of the hollow graphite cube surrounding the moderator, hand and neutron source. A hole, by which the beam line may be introduced closer to the moderator, was designed such that sufficient space existed to adjust the distance between the source and the surface of the moderator as explained earlier, simultaneously providing scattering of neutrons produced at higher angles. The modeling results showed that an increase in the thickness of the graphite increased the thermal flux and, consequently, aluminum activation of the phantom, reaching saturation between 25 and 30 cm of graphite. Accompanied with this was an increase in photon production, proportional to the increase in graphite thickness. It is useful to note that the produced photons predominantly fall between 2 and 3 MeV, originating from hydrogen neutron capture activation in the hand and moderator, followed by 2.2 MeV gamma emission.

It was concluded that a graphite reflector would be the best material for aluminum measurement, built as a hollow cube (30 cm thick) around the irradiation site including

the apertures for the beam line and the patient's hand. Once the reflector material size and shape was determined it was possible to proceed with shielding and dose calculations.

3.3.4 Shielding and Dose Calculations

Shielding is needed around the irradiation site to reduce the dose delivered to the patient and activation in the target room. In addition, photons are produced by neutron interactions in the moderator and reflector materials, so some specific γ-ray shielding is required.

Boronated (5 %) wax was modeled, since it is a conventional and commercially available shielding material for neutrons. The neutrons emerging from the irradiation cavity will be thermalized by the wax and eventually captured by boron via the thermal neutron capture reaction. The graphite reflector provides some degree of shielding for photons, but it is not sufficient for the photons that are produced in the moderator and inside the reflector itself. Therefore, a 1 cm layer of lead surrounded the neutron shield.

Dose calculations for the hand phantom and for the patient's body were done after all design features of the irradiation facility had been selected. The hand and beam line apertures allowed neutron leakage along the patient's arm and around the line, increasing the dose to the patient and in the target room. A technician, who might be present during *in vivo* measurements in the target room, was modeled as well (figure 3.11), and positioned on the opposite side to the hand opening. The average equivalent dose to a 70 kg Reference Man, at a current of 25 μA and delivered in the 180 s of aluminum

activation to both the patient and technician, represented by vertical water cylinders (175 cm high x 11.3 cm radius), was calculated.

The neutron fluence for the energy bins specified by published fluence-to-kerma conversion factors were calculated for the hand phantom, a patient, and a technician (Caswell *et al.*, 1982). The photon dose was calculated as

$$D_\gamma = \sum_\gamma E_\gamma \frac{\mu_{en}(E_\gamma)}{\rho} \Phi(E_\gamma)$$

where E_γ is the photon energy, μ_{en}/ρ is the mass energy absorption coefficient (Hubbell and Seitzer, 1996) and Φ is the photon flux.

Shielding	Hand dose (Sv)	Patient dose (Sv)	Technician dose (Sv)
6 cm of boronated (5 %) wax	2.93×10^{-1}	2.60×10^{-3}	2.86×10^{-5}
12 cm of boronated (5 %) wax	2.93×10^{-1}	1.99×10^{-3}	2.09×10^{-5}
20 cm of boronated (5 %) wax	2.93×10^{-1}	1.46×10^{-3}	1.18×10^{-5}
20 cm of boronated (5 %) wax and 1 cm of lead	2.93×10^{-1}	1.29×10^{-3}	3.37×10^{-6}
Experimental work (2.25 MeV and 25 μA)	5.46×10^{-2}	N/A	N/A

Table 3.2 Equivalent dose estimations for the hand, and the effective dose for a patient and a technician during the aluminum measurement.

The modeled data (table 3.2) show that the estimated hand dose for 180 s of irradiation and at 25 μA, is much higher than the experimentally measured value using a microdosimetry detector.

Alongside with the need to measure the hand and subject's dose experimentally, the dose discrepancy between the MCNP prediction and experiments was one of the reasons for the detailed microdosimetry measurements that have been conducted and are reported in Section 2.3. Although the experimentally measured dose that is delivered to

the subject's hand is much higher than expected, based on indium foils and Snoopy measurements, it is well below the dose predicted using theoretical modeling. The reason for this discrepancy is unknown, but it was observed that the difference between the experimental and predicted dose is a constant factor, suggesting that perhaps the experimental yield is much less than that predicted by theory. Therefore, all dose calculations were used only for relative comparison between different shielding materials, as it will be illustrated in Section 3.5, until the source of this inconsistency is determined.

Experimental measurements of the neutron yield from the $^{7}Li(p,n)^{7}Be$ reaction, conducted by Yu and co-authors, found that the actual yield was significantly less than that predicted by theoretical calculations (Yu *et al.*, 1998). The authors were unable to provide an explanation for this discrepancy, however, it follows that if the neutron yield is less, and the experimentally measured dose would also be less. This hypothesis needs experimental confirmation before any absolute dose calculations can be made using MCNP.

Whatever the outcome of this search might be, microdosimetry measurements have governed the adjustments to the procedure that had been suggested for aluminum bone measurements due to the high hand dose. Along with these adjustments in experimental procedure (see Part I - Sec. 2.4.), additional MCNP modeling has been conducted. It was necessary to justify the developed design of the irradiation cavity for a proton energy of 2.25 MeV for the lower energy of 2 MeV.

3.4 Cavity Design for the Proton Energy of 2 MeV

The two main differences between the 2 and 2.25 MeV proton energies are the neutron yields and the maximum neutron energy emerging from the Li-target (table 3.1). Obviously, both are much lower for the 2 MeV proton energy than for 2.25 MeV. Therefore, many of the decisions that were made during the design of the cavity for the higher proton energy, such as the chosen materials with constant proton energy (for example see figure 3.4), are still valid. Only the dimensions of the suggested components for the cavity have been recalculated.

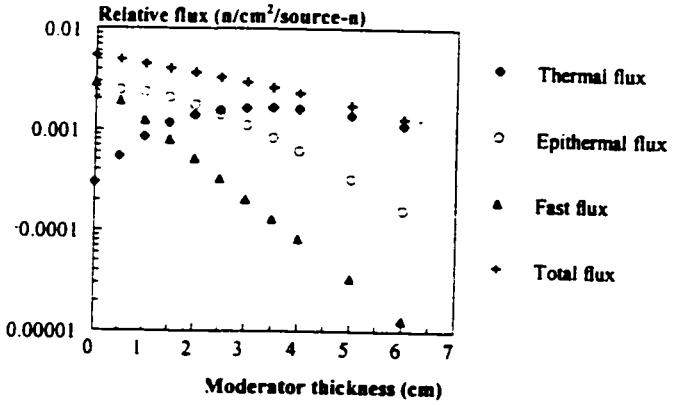

Figure 3.9 Neutron flux over the hand phantom for different moderator thicknesses with a constant radius of 13 cm. The modeled geometry is the same as on figure 3.4, with varied moderator thickness. Proton energy is 2 MeV.

Following the same order as used previously, and the general design aim to maximize the thermal flux on the hand, a polyethylene moderator with different thicknesses was modeled between the neutron source and the aluminum phantom in air at 2 MeV proton energy. Graph 3.9 presents the results of this modeling, clearly showing the maximum neutron flux may be achieved with 3 cm of polyethylene. It is confirmed that the thermal flux as a proportion of the total flux increases with the increase of

polyethylene thickness, being 56 % at 3 cm and 87 % at 6 cm. The absolute value of the thermal flux, however, decreases by a factor of 1.5 with the same increase in the moderator thickness. Therefore, 3 cm of polyethylene is required between the hand and the source to maximize the thermal flux, and further, to increase aluminum activation in the hand. As illustrated in figure 3.6, there is no change in the thermal flux with the increase of the moderator radius, since a 13 cm radius for the polyethylene moderator is necessary to cover the hand completely. Thus, a polyethylene moderator with a radius of 13 cm has been confirmed.

Rejecting the need for a neutron filter, the dimensions of the graphite reflector have been remodeled as the next step. The modeled geometry is the same as explained in Section 3.5, and the accompanying results are presented in figure 3.10. It may be seen that the thermal flux increases constantly with an increase in the graphite thickness, reaching a plateau after approximately 30 cm thickness. Therefore, any reflector thickness above 30 cm will efficiently reflect neutrons into the irradiation site, increasing aluminum activation. On the other hand, an unnecessary increase in the graphite thickness will increase the hand dose as well, because of the photon production. Thus, it is recommended to make the graphite reflector of 30 cm thickness.

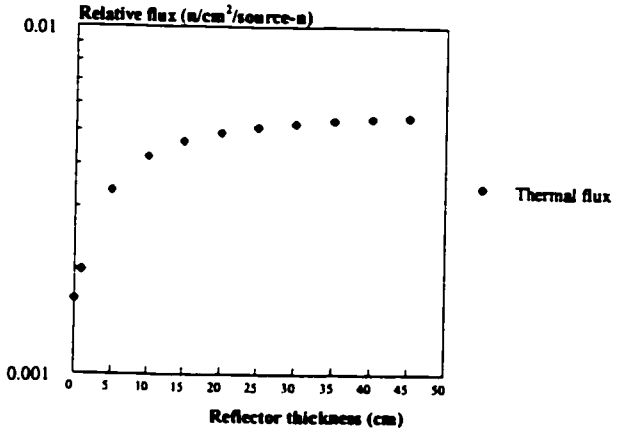

Figure 3.10 Effect of graphite reflector thickness on the thermal neutron flux calculated as neutron flux over the hand phantom.

The Monte Carlo code was used as a tool to design an improved irradiation facility as presented in figure 3.11. The primary design goal was to increase aluminum activation per unit time for a fixed proton current incident on a lithium target. The design studies resulted in the choice of a polyethylene moderator, a graphite reflector and a combined boronated wax and lead shield. Filtration of fast neutrons was rejected as incurring too great a loss of thermal neutrons. The exact source-to-moderator distance involved a compromise, which is left for experimental optimization. An important discrepancy between modeled and measured doses remains to be resolved. The suggested cavity designs are reasonably similar for the proton energies of 2 and 2.25 MeV, with a minor difference in the moderator size that is necessary to achieve maximum thermal flux in the hand.

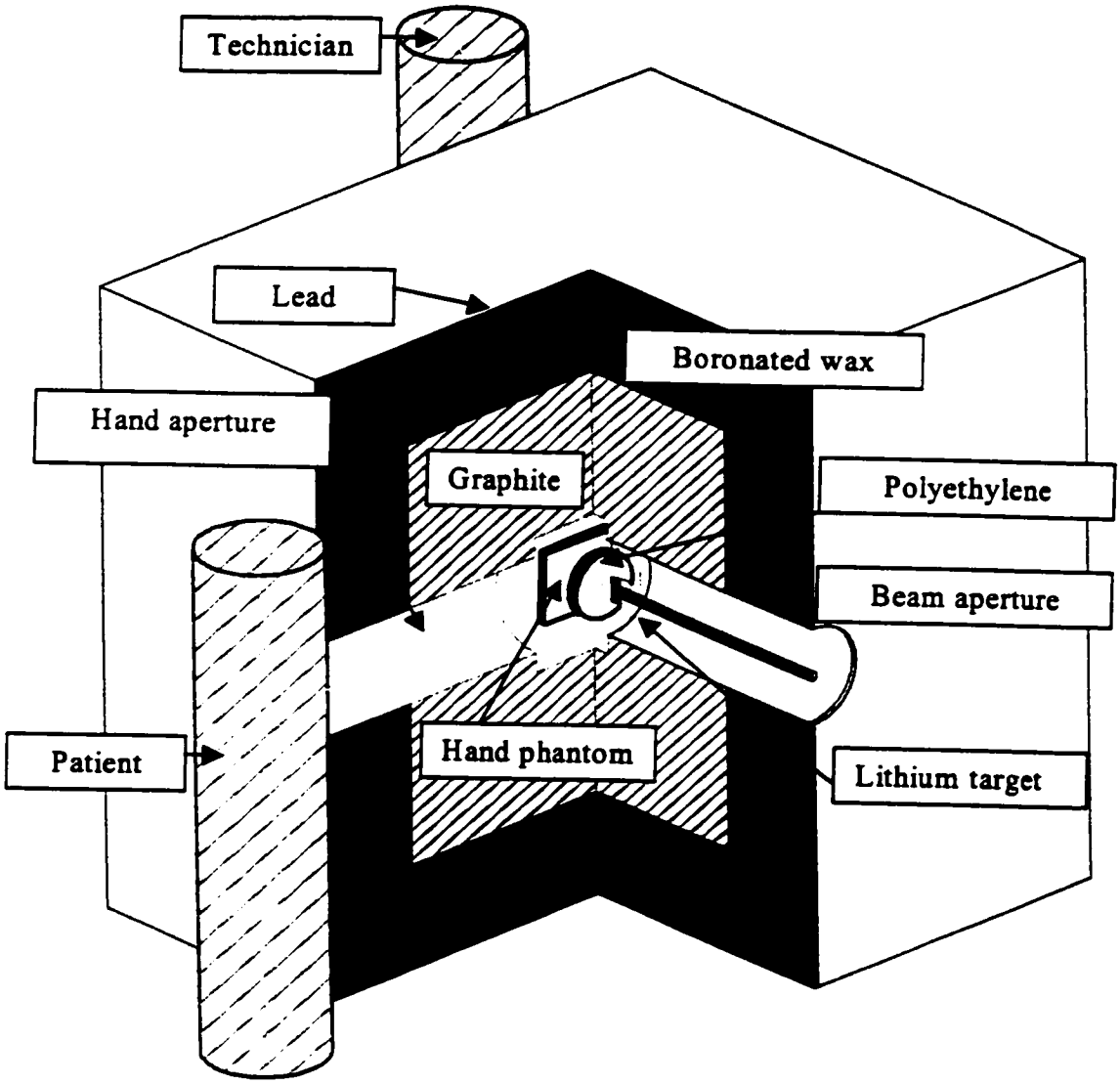

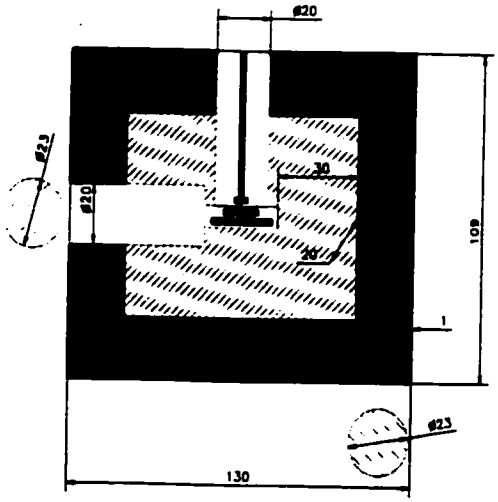

Figure 3.11 The final design of an improved irradiation cavity for bone aluminum activation using an accelerator low energy neutron beam.

3.5 Cost and Weight Optimization of the New Cavity

The next step in the cavity design was to investigate the associated costs for its construction. The cost of the materials that have been chosen for the cavity was very high, giving a total of close to one hundred thousand dollars, excluding precutting, delivery and taxes. Another addition to the price would be the time required for the assembling of the cavity. Therefore, supplementary Monte Carlo modeling has been done in an attempt to lower the cost of building the irradiation cavity. Furthermore, from a practical point of view, the cavity was very heavy, and it was suggested to investigate different possibilities to lower its weight as well.

Significant saving can be achieved by using graphite powder (density 1.8 g cm^{-3}) instead of solid graphite (density 2.25 g cm^{-3}). Modeling has shown that this change does not affect the thickness of the graphite reflector that was previously suggested. An additional price reduction may be accomplished by using different neutron shielding materials, rather than ones that are commercially available and very expensive.

One possibility that would lower the cavity weight as well, is to use borated water around the reflector, rather than boronated wax. Also, it was investigated to use just water as the neutron shielding (Chettle *et al.*, 1980). In both situations the use of a solution that may be emptied, considerably lowers the assembly weight, allowing easier manipulation and repositioning. Since the KN accelerator beam line is constantly used for different experiments, this flexibility was considered important. Table 3.3 presents dose estimations if different materials replace borated wax as the neutron shielding (figure 3.11). It is also necessary to emphasize that all dose calculations have to be compared

relative to one another until the reason for the discrepancy between the experimental and theoretical dose is known.

Shielding	Hand dose (Sv)	Patient dose (Sv)	Technician dose (Sv)
20 cm of boronated (5 %) wax	2.93×10^{-1}	1.46×10^{-3}	1.18×10^{-5}
20 cm of boronated (0.5 %) water	2.94×10^{-1}	3.41×10^{-4}	9.58×10^{-6}
20 cm of water	2.90×10^{-1}	2.40×10^{-3}	5.10×10^{-5}

Table 3.3 Equivalent dose estimations for the hand, and the effective dose for a patient and a technician during the aluminum measurement using different neutron shielding materials. Note that there is no lead photon shielding around the neutron shielding at this point of modeling.

As anticipated, the hand dose is unchanged with the change of the neutron shield while the patient's effective dose has been affected the most. The lowest patient effective dose would be delivered by using boronated water, followed by boronated wax and water. This order is observed for the technician effective dose as well, but accompanied with much smaller differences between the doses.

Besides reducing cost, different ways of lowering the cavity weight have been investigated. As explained before, any solution that can be temporarily poured out would lower its weight. Furthermore, it was considered how the dose would be affected if the top and/or bottom of the reflector box were omitted. These modeling results are in table 3.4. Note that at this point of modeling the lead photon shield has been added around the cavity.

The same pattern has been observed, with a constant hand dose and the patient dose being the most affected once the changes are made. The top and bottom of the graphite reflector may be excluded from the cavity, while keeping the shielding at the sides.

Shielding	Hand dose (Sv)	Patient dose (Sv)	Technician dose (Sv)
Whole cavity	2.91×10^{-1}	1.53×10^{-3}	2.03×10^{-5}
No top on the cavity	2.90×10^{-1}	2.07×10^{-3}	2.12×10^{-5}
No top and bottom on the cavity	2.89×10^{-1}	2.03×10^{-3}	2.51×10^{-5}

Table 3.4 Equivalent dose estimations for the hand and the effective dose for a patient and a technician during the aluminum measurement in an attempt to lower the cavity weight. Note that all cavities are surrounded with 1 cm thick lead as photon shield.

Since there is modest increase in the patient and technician dose, it was concluded that the optimized irradiation cavity for the hand aluminum measurement should be built using a polyethylene moderator, graphite-powder reflector, surrounded with either boronated water or water followed by 1 cm of lead. Moreover, it is possible to build the reflector box without the top and bottom to lower the cavity weight further and improve mobility. It is suggested that a Perspex box should be made for the graphite powder and solution, around which the lead shield may be fixed. The Perspex box should have two cylindrical apertures for entering of the KN accelerator line, and the other one, for the patient's hand. Inside the hollow box the moderator and hand have to be placed along the neutron beam line. The estimated material cost of this, final hand cavity is $ 8000.

The newly designed irradiation cavity is expected to increase thermal neutron flux by a factor of 1.53 compared to the polyethylene cavity that has been experimentally used. This should lead to a consequent reduction in detection limit to 0.92 mg of aluminum in the hand. This is a notable contribution towards the goal of reducing the detection limit of 1.14 mg at 2 MeV towards the normal range.

Chapter IV

In Vivo Neutron Activation of Aluminum in Bone

Measuring aluminum in bone using *in vivo* neutron activation analysis is a particularly challenging measurement to contemplate due to its rather low bone levels, small probability of interaction, short half-life, presence of interfering interactions, and the complexity of the *in vivo* gamma ray spectra. These are the main reasons that there is not yet available an *in vivo*, non-invasive technique for aluminum body burden measurement, that is sensitive enough to see aluminum levels in healthy subjects or which is widely available.

It is believed that for aluminum the main target and storage organ is the skeleton. Thus, the most common site for aluminum measurement is the bone of the hand (Green *et*

al., 1992; Lewis *et al.*, 1997), in which the aluminum level is expected to be between 0.2 and 0.3 mg (ICRP, 1975).

Aluminum may be measured via the thermal neutron reaction $^{27}Al(n,\gamma)^{28}Al$ (σ = (231±3) mb). ^{28}Al is radioactive, with a half-life of 2.25 min., and decays by the emission of a 2.865 MeV β^- particle accompanied by a 1.78 MeV gamma ray (100 %). This aluminum characteristic gamma ray escapes the body, and therefore, may be detected with NaI(Tl) scintillators. Unfortunately, for the $^{27}Al(n,\gamma)^{28}Al$ reaction there are two interfering nuclear reactions $^{31}P(n,\alpha)^{28}Al$ and $^{28}Si(n,p)^{28}Al$, with thresholds of 1.95 MeV and 4 MeV respectively. Since these reactions also produce ^{28}Al, the measured intensity of the 1.78 MeV gamma rays will be partially due to the presence of ^{31}P and ^{28}Si in any *in vivo* sample.

One of the best available neutron sources for *in vivo*, non-invasive aluminum activation in bone is at the McMaster accelerator laboratory, a KN Van de Graaff-accelerator, in which the neutron production is based on the $^{7}Li(p,n)^{7}Be$ reaction. The potential of this low-energy accelerator beam (neutrons up to ~ 500 keV) to provide sufficient thermal neutron flux for bone aluminum measurement has been applied during the course of this work. The main advantage of this neutron source is that the maximum neutron energy produced using the KN-accelerator is well below the threshold energies for the activation of ^{31}P and ^{28}Si, eliminating the possibility of their activation, and therefore, considerably simplifying the aluminum measurement. Until recently, it was believed that another advantage of this neutron source is a low dose delivered to the patient.

Detailed microdosimetry measurements, however, have indicated that the hand dose delivered during an aluminum measurement would be about two hundred millisieverts. Therefore, adjustments to the activation procedure were required. It was anticipated that a hand dose of approximately 50 mSv would lead to ethical approval of the procedure for humans by McMaster Human Ethics Board. Following this guideline, the currently optimal experimental procedure consists of 180 s of irradiation, followed by a short transfer time, and a 300 s counting time. Aluminum activation has been performed in a polyethylene cavity with 2.4 cm thick walls that was placed 2.5 cm from the target. One side of the hollow irradiation cavity was removed due to the need to insert the hand or phantom into the irradiation site. Short transfer followed the irradiation, and the counting of aluminum activation was performed using two NaI(Tl) detectors facing each other, organized in quasi-4π geometry. This geometry minimized the loss of gamma rays and increased detection efficiency. Suggested irradiation parameters of 2 MeV proton energy with an approximate 100 μA current, resulted in a minimum detectable limit of 1.14 mg of aluminum, corresponding to a hand dose of 48 mSv.

The technique of *in vivo* neutron activation analysis of aluminum has been further explored using Monte Carlo modeling. The general aim throughout the modeling was the need to produce as many thermal neutrons as possible in the hand and, further, to lower the measurable levels of aluminum. Specific neutron source modeling was needed, since the McMaster's KN accelerator produces low energy neutrons in the forward direction with maximum neutron energies of 520 and 230 keV at 2.25 MeV and 2 MeV proton energies, respectively (Arnold, 2000).

For computer modeling the Monte Carlo code for neutron and photon transport (version 4b2) was used to investigate the behavior of neutrons and photons in different materials, with three neutron energy bins: thermal, epithermal and fast. A schematic representation of the new assembly, which is expected to provide safe and feasible neutron activation of aluminum in bone, is shown in figure 3.11. With a low energy accelerator neutron beam, the polyethylene moderator (diameter of 13 cm and thickness of 3 cm at 2 MeV) was chosen as the best material to increase the thermal flux in the hand. A position of 2 cm from the ^{7}Li target relative to the moderator surface is found to induce the highest aluminum activation. However, better uniformity of thermal neutrons throughout the hand is achieved at greater distances. Therefore, the assembly was designed to allow a possible variation in the distance until experimental confirmation of the optimal distance is determined, due to the limitations of simulating realistic aluminum measurement. As expected, theoretical modeling illustrated that the filtration of epithermal and fast neutrons decreases the dose to the patient, but simultaneously lowers the thermal flux. Since measurements are performed on the patient's hand, which is considered not to be a radiosensitive organ, a filter was not introduced in the design to be able to maintain the higher thermal flux. Additionally, it is feasible to shield the patient's body while the hand may be extended from the rest of the body.

Around the moderator and source was placed a reflector. A 30 cm graphite reflector was found to provide good scattering of epithermal and fast neutrons back into the moderator. Also, graphite simultaneously moderated and scattered neutrons into the irradiation site, increasing the thermal flux accompanied with low photon production. Neutrons, which are not back scattered but transmitted through the reflector, are

thermalized, and eventually absorbed in the neutron shielding. Thus, 20 cm of boronated wax was added as a neutron shield followed by another 1 cm layer of lead to attenuate emitted photons.

Simulation data show the hand and patient's dose to be high compared to that experimentally measured. It is not possible to explain this discrepancy without further work, but there are published experimental results (Yanch, personal communication; Yu *et al.*, 1998), that also noticed a similar disagreement between the theoretical and experimental neutron yields for a low energy accelerator. Similar conclusions have been suggested for the discrepancy between the modeling and experimental results, during the development of a manganese procedure in humans that has been performed in the same laboratory as this work (Arnold, 2000). Until the cause of this discrepancy is known the theoretical modeling will not be used for absolute dosimetry calculations for the aluminum measurement in the hand.

Extensive dose calculations were performed especially during neutron/photon shielding design. It is suggested that boronated water be used as a neutron shield around the reflector, so that the solution may be emptied to increase the cavity mobility and temporarily lower its weight. Additionally, it is feasible to build the reflector cavity without top or bottom walls to decrease the cavity weight further, with only a small increase in the patient effective dose.

Using MCNP the polyethylene irradiation cavity, that has been experimentally used, was simulated and the thermal flux over the hand was tallied. Assuming that the new assembly would provide the expected experimental improvement, a minimum detectable limit can be estimated. The newly designed irradiation assembly is expected to

increase aluminum activation by a little over 50 %, which should lead to a consequential reduction in detection limit by 20 – 25 %. This presents a significant contribution towards the goal of reducing the experimentally determined detection limit to the normal range of aluminum levels of 0.2 to 0.3 mg that are estimated in healthy subjects.

4.1 Future Development and Application of an Accelerator Based *In Vivo* Aluminum Measurement in Bone

In the final remarks about the *in vivo* procedure for aluminum measurement in humans it is necessary to explore future directions that would lead to the possibility of lowering the minimum detectable limit, and thus, open a broad field of research that may improve our knowledge about aluminum health effects, metabolism and monitoring of aluminum occupational exposure.

Besides building the new irradiation cavity that should lower the minimum detectable limit and provide better subject shielding, it is expected that future work should explore the use of an accelerator that has the ability to produce a higher proton current on the target than the KN-accelerator used throughout this work. The opportunity to produce a higher proton current will open a number of subsequent possibilities for adjustments in the irradiation parameters, that combined might produce better aluminum activation. A higher proton current will produce a higher thermal neutron flux in the irradiation site that is essential for aluminum activation. Furthermore, the incident proton energy may be further lowered to produce an additional increase in the thermal

component in the neutron beam. Knowing that aluminum has a short half-life, the irradiation time may be shortened, when higher current is used, to maintain the hand dose at an acceptable level. In summary any increase in aluminum activation to dose ratio should be investigated when stable irradiation may be achieved.

Presently it is believed that the local hand dose that has to be delivered during aluminum activation is the main limit for the *in vivo* application of aluminum neutron activation analysis. The limit of approximately 50 mSv to the hand is expected to receive ethical approval, when additional neutron and gamma shielding for the subject's body is present. This emphasizes the need for more investigation to increase the thermal flux and further activation in order to reach aluminum levels in healthy subjects.

A cyclic activation technique may be investigated (Wyatt *et al.*, 1993a) in combination with the application of higher proton current. However, again, the dose limit will affect this approach as well. An additional possibility is to use an anti-coincident counting system. This may lower the background below the aluminum and calcium peaks, and further improve the signal to background ratio, leading to lower measurable aluminum levels. Another possibility lies in commercially available digital electronics that might be used for signal processing due to its ability to process the acquired signal better.

Whatever the future pathway in experimental work will be, the developed procedure is a suitable means of screening patients with significantly elevated aluminum levels, such as patients with renal failure (Ellis *et al.*, 1988, Wyatt *et al.*, 1993b). Following experiments to assess the accuracy of neutron activation measurements, for example by comparison with atomic absorption spectrometry, and after obtaining ethical

approval for its application on humans, the proposed diagnostic procedure (with the new irradiation cavity) may contribute to the monitoring of aluminum levels in these patients.

Once the improvement in the system is achieved so that healthy subjects may be measured, it will open broad areas for research about aluminum's role in Alzheimer's disease, water pollution and possibly for monitoring occupational exposure to this toxic element. Following the suggestion that an aluminum serum level of 0.25 – 0.35 μmol/l (Riihimäki *et al.*, 2000) might be correlated with the appearance of health problems in workers, it is expected that a similar relationship between bone aluminum levels and health effects will be found. Contrary to bone aluminum levels, aluminum in blood gives only information about recent aluminum exposure, and therefore, the presence of this relationship might be more significant for regulations in occupational exposure of aluminum.

Once the procedure for aluminum activation analysis is able to measure aluminum concentrations in healthy subjects, the boundaries of future *in vivo* research might be unlimited since our present knowledge about aluminum, its metabolism and health effects is restricted.

PART II

In Vivo X-ray Fluorescence of Strontium in Human Bone

Chapter I

Introduction

If a sample is irradiated by photons that have higher energy than, for example, the K shell binding energy of an element under investigation, photoelectric absorption may result in characteristic K x-ray emission. Separate elements within the sample then can be identified by observing peaks in the pulse height spectrum corresponding to the characteristic x-rays of that particular element. Alternatively to this qualitative analysis, the technique can be used as a quantitative tool when the element's concentration is determined by applying an appropriate calibration process. The technique that is briefly outlined here is known as x-ray fluorescence (XRF), and it has been successfully developed and applied *in vivo* for several different elements.

The first *in vivo* XRF measurement is believed to have been performed in 1968 to measure iodine levels in the thyroid gland (Hoffer *et al.*, 1968). Since then, several heavy

elements, usually toxic, have been successfully measured. For example, cadmium (Christofferson and Mattsson, 1983; Börjesson *et al.*, 1996) and mercury (Börjesson *et al.*, 1995a) had been measured in the human kidney. Furthermore, a number of *in vivo* studies of toxic elements that accumulate in human bone has been reported such as uranium (O'Meara *et al.*, 1997), mercury (Börjesson and Mattsson, 1995b), and gold (Shakeshaft and Lillicrap, 1993) to name some. XRF was successfully applied for measurement of platinum (Jonson *et al.*, 1988; Börjesson, 1991) and bismuth (Börjesson, 1996) as well. The *in vivo* XRF technique has been reviewed and well explained in the literature (Börjesson and Mattsson, 1995b; Mattson and Scott, 1989; Chettle *et al.*, 1990).

The most recognized and applied XRF technique, nevertheless, is bone lead XRF measurements in humans. Measurement of lead began in 1971, and since then, three alternative XRF techniques have been developed. One of these techniques, which has been adopted by many research groups, employs a ^{109}Cd source in a backscatter geometry that induces K x-ray fluorescence of lead stored in the tibia or some other bone. Another technique use a ^{57}Co source in a 90 degree geometry (Ahlgren *et al.*, 1976; Christoffersson *et al.*, 1984) that irradiated a subject's finger bone, and thus, fluoresced accumulated lead. A third XRF technique was developed to measure lead L x-rays by irradiating the bone site either with radiation sources, such as ^{109}Cd (Wielopolski and Slatkin, 1981) and ^{125}I (Wielopolski *et al.*, 1983a), or with polarized x-rays (Wielopolski *et al.*, 1989).

The key advantage of the in *vivo* x-ray florescence technique is that it is noninvasive and delivers a low radiation dose to the subject. Commonly the apparatus required for this technique is transportable, and mobile laboratory facilities are easily

established. In comparison to neutron activation analysis it is less expensive and demanding. Additionally, bone lead XRF measurements have demonstrated that XRF may be easily assembled and used in a clinical environment, accompanied with relatively straightforward personnel training.

Nevertheless, the technique has some disadvantages. Attenuation of the incoming photons, and outgoing characteristic x-rays in overlying tissue imposes a limit to which elements can be measured. It is widely accepted that the *in vivo* XRF technique may be applied only for an element that has atomic number higher than 40 (Börjesson, 1996; O'Meara, 1999; Mattsson and Scott, 1989). However for superficial sites, elements down to iron (Z = 26) have been measured (Mattsson and Scott, 1989). The concentration of an element under consideration may impose an additional limit. In principle, such as when kidney mercury was measured, the lowest detection limit was too high. Thus only those subjects with toxic burden could be reliably measured, a point at which the clinical effects would be already evident (Mattsson and Scott, 1989).

Three broad groups of problems have led to *in vivo* XRF studies. Namely, heavy elements accumulated in occupationally exposed subjects, environmental medicine, and studies of the uptake and kinetic behavior of toxic elements unintentionally introduced into the body or as diagnostic agents.

In the second part of this thesis, bone strontium *in vivo* XRF is developed and tested as a quantitative tool for strontium measurement in human bone. However, before explaining the technique in more details, it is valuable to indicate the motivation for developing such a non-invasive measurement system.

1.1 Why Is Strontium Important?

Strontium is ranked fifteenth in abundance in the Earth's crust occurring at a concentration of 450 mg/kg. In ocean water, it is the most abundant trace element, reaching values of up of 8 mg/l. Ground waters contain smaller amounts of the element ranging from 0.021 to 0.375 mg/l (Cabrera *et al.*, 1999).

Strontium is naturally present in food and beverages. Meat, poultry, vegetables and fruit contain relatively low amounts of the element (0.3 – 5.1 mg/kg), whereas in cereals, grains and seafood it may be present in concentrations up to 25 mg/kg (Özgür *et al.*, 1996). Hence, the amount of strontium content in the human diet and daily intake varies according to the geographic areas, the type of food consumed and the climate.

The gastrointestinal tract represents the main route of entry of strontium into the human body. Approximately 90 % of the element's dietary intake in infants is absorbed, compared to only 10 % in the elderly. The intestinal absorption of strontium increases under fasting and is negatively affected by a high dietary content of calcium or phosphate. There is also a suggestion that strontium may also be absorbed in the lung and through the skin. Strontium is excreted in urine, and to a lesser extent in feces and perspiration (Leeuwenkamp *et al.*, 1990; Cabrera *et al.*, 1999).

Many strontium studies have been performed in conjunction with those of calcium. The two elements have similar chemical and physical characteristics and are similarly involved in a number of biological processes. In animals, 99.1 % of absorbed orally administrated strontium is deposited in bone, comparing to 98.6 % of calcium. Under normal conditions, the animal bone strontium to calcium ratio varies between 0.5

and 1 mg Sr/g Ca, which is on the same order as in serum (Cabrera *et al.*, 1999). The Sr/Ca mass ratio in human bone is normally in range 0.1 – 0.3 mg Sr /g Ca depending on diet, environment, age and sex.

Strontium is a bone-seeking ion that readily exchanges for calcium in the apatite lattice of bone. One potential mechanism existing at high strontium concentrations is that the element replaces calcium in bone by heteroionic exchange. Incorporation of the larger strontium ions in rat bone will induce distortion in the crystal lattice and impaired crystal growth. Consequently, lower bone mineral density is likely to occur in strontium overload. Low doses of strontium, however, do not seem to have adverse effects on the skeleton. In rats, an increase in bone mass is noticed when strontium was given in low doses (Grynpas *et al.*, 1990).

Boivin and co-authors (1996) studied changes in bone mineral due to the administration of a strontium salt (S12911) in monkeys. In control animals, strontium was found to be homogenously distributed throughout the bone tissue, while in treated animals it was detected only in the calcified matrix. It is reported that strontium is dose-dependently incorporated into bone mineral, with a higher amount present in newly formed bone tissue than in old bone. The heterogeneous distribution of strontium in bone is explained by the fact that strontium is not only incorporated into crystals (heteroionic exchange), but it is also taken up onto their surface (absorption and exchange). In contrast, in old bone strontium is exclusively taken up onto the surface of the crystal. Contrary to findings in rat bone, strontium uptake does not modify a monkey's bone crystal unit cells. In addition, in the treated monkeys bone strontium was always higher in trabecular than in a compact bone.

Blood is the second most important location of strontium. Data in the literature on normal serum levels in subjects with intact renal function vary between 10 μg/l and 217 μg/l (Rudolph *et al.*, 1973; Cabrera *et al.*, 1999; Mauras *et al.*, 1986). In uremic parents, either treated or not by hemodialysis, data in general point towards increased serum strontium levels as compared with subjects with normal renal function. Non-dialyzed patients had increased strontium levels in muscle by a factor of 2, while dialyzed uremic patient showed levels as high as 7 times the controls (Rudolph *et al.*, 1973). Recent findings indicated that serum strontium levels in dialysis patients may differ from center to center, ranging from values comparable to those in subjects with normal renal function up to 30-fold higher. The cause of these differences might be in the dietary intake as well as the oral intake of aluminum-containing phosphate binders, which may contain up to 217 μg/g of the element.

The therapeutic potential of the intravenously administrated radioactive ^{89}Sr was recognized in 1940 when it was discovered that it could be used for the treatment of bone pain from metastatic prostate cancer (Cabrera *et al.*, 1999). This isotope, as well as ^{85}Sr and ^{88}Sr, has been used as a marker of calcium metabolism. Another strontium therapeutic effect is in evidence that strontium can harden bone and teeth (Snyder and Secord, 1982). More importantly, a beneficial effect of low strontium doses has been noted in osteoporosis patients, while at intermediate and high doses strontium can induce osteomalacia in renal patients, and rickets in children.

Osteoporosis is an increasing problem in many industrialized and developed countries. The term osteoporosis is often used to describe a condition of reduced bone mass, which is the result of a reduction of both the osteoid and the bone mineral content

in the bone structure. These can induce a change in both the elemental composition and the physical density of bone, leading to enhanced bone fragility, and consequently an increase in fracture risk. Animal studies have found that oral administration of strontium salts can redirect and improve the condition of osteoporotic bone (Marie *et al.*, 1993; Boivin *et al.*, 1996). Prolonged administration of strontium to postmenopausal osteoporotic women resulted in a decoupling between bone resorption and formation that yielded a significant increase in lumbar spine bone mineral density of treated subjects (Reginster, 1997). These findings point to a promising new agent (S12911) for the treatment of osteoporosis in humans (Reginster *et al.*, 1999) that is currently undergoing human trials, and the drug should be available within 1 to 5 years.

The terms 'rickets' and 'osteomalacia' describe disorders in which there are defects in the mineralisation of the organic matrix of the skeleton. Rickets is a defect encountered during the period of growth, whereas osteomalacia is a defect encountered after growth is completed. Vitamin D deficiency is one of the main causes of these disorders, but another factor influencing calcium absorption is its interaction with strontium. There are animal studies indicating that rickets can also be produced by consuming strontium and manganese together.

A recently published work showed that the prevalence of rickets among children living in Turkish villages, having soil strontium content of more than 350 ppm, was significantly higher than that of children living in other villages with lower strontium levels (Özgür *et al.*, 1996). Similarly, an increase in bone strontium concentrations was reported in dialysis patients suffering from osteomalacia (Cabrera *et al.*, 1999).

Concluding the motivation for *in vivo* bone strontium measurements it is interesting to mention that a small strontium fraction incorporated in bone will be registered as calcium when bone mineral density (BMD) or bone mineral content (BMC) is measured, using dual energy x-ray absorptiometry (DEXA) (Nielse *et al.*, 1999). The apparent values of BMC and BMD increase linearly with increasing substitution of calcium by strontium (Christoffersson *et al.*, 1997), commonly administrated as a strontium-containing drug (S12911). A direct linear relationship ($r^2 > 0.99$) was recently found between strontium content and overestimation of BMD and BMC. This demonstrates that reliable DEXA determinations may be carried out in the presence of strontium only if the bone strontium content of the measured bone is known. Currently, a correction due to strontium exchange in bone can be made if bone biopsies are taken from a representative location. Therefore, the availability of an *in vivo*, non-invasive and painless technique that can measure strontium concentration in bone would be of great benefit for bone density measurements as well.

1.2 *In Vivo* X-ray Fluorescence of Strontium

An incident photon, from a radioactive source or x-ray tube, with an energy exceeding the binding energy of an electron in the strontium K shell of 16.10 keV may be absorbed and the electron ejected. Following this process, a less tightly bound atomic electron fills the vacancy. The energy difference between these bound states appears as a characteristic x-ray or an Auger electron. For strontium (Z = 38) the fluorescent yield is 69.1 %, and consequently, favours photon emission. By measuring the energy and the number of characteristic x-rays, it is possible to detect the strontium amount in human tissue. Strontium characteristic x-rays have low energies of 14.16 keV and 15.83 keV for Kα and Kβ, respectively. Therefore, the absorption of the emitted K fluorescence radiation in human tissues restricts *in vivo* measurement of strontium. Similarly, an x-ray emitted due to a L shell vacancy is termed L x-ray fluorescence, and has correspondingly lower energies than K XRF. The absorption of strontium L x-rays is even more pronounced than K x-rays. Moreover, they are positioned at energies lower than 2 keV, thus completely precluding L x-ray fluorescence for *in vivo* strontium assessment.

This technique essentially samples strontium concentrations in a few millimeters of bone, and although subject to the uncertainties associated with microstructure, could provide information on the strontium distribution at the bone surface only. More than 99 % of the strontium recorded from the thick bone by XRF will reside within 2 mm of the surface. Due to the their energy difference, the strontium Kα signal will originate from only 1.71 mm while the Kβ from 2.33 mm thickness of cortical bone, when the

attenuation of both the incoming as well as the outgoing radiation is taken into consideration.

It might be predicted that the size of the strontium x-ray peaks in the spectrum depend on the concentration of strontium in the bone, as well as on the thickness of the overlying tissue, shape and size of the bone, distances between the source and sample, and the sample and detector. A proper estimation of strontium concentration in bone would require correction for all these factors. However, a technique for XRF signal normalization has been well developed and applied to the ^{109}Cd backscatter geometry bone lead system, which normalizes the lead K x-ray peaks to the coherent scatter peak, making the above corrections unnecessary. In an attempt to eliminate the need for complex corrections, the use of this normalization will be investigated for strontium XRF assessment, along with two other approaches (Part II - Chapter III).

In vivo XRF has been previously studied and applied to animal bone strontium assessment (Snyder and Secord, 1982), along with a post-mortem measurement of human tibia bone (Wielopolski *et al.*, 1983b).

Snyder and Secord (1982) measured normal and elevated levels of strontium in animal (rabbits and dogs) bone to determine whether, following one administration of strontium, a time dependant change in bone strontium content could be observed. A 37 MBq ^{109}Cd based system was used with a SiLi detector mounted in approximate 45 degree geometry, while the source-skull distance was between 0.5 and 1 cm. A shielding system surrounded the detector and included a shutter for covering the source when not in use. Three pins were mounted on the front surface of the shield, as reference points for repositioning the detector to the shaved bone site - skull. Since the intent of the study was

to observe the kinetic behavior of bone strontium and to estimate its biological half-life in bone, animals were injected with a high dose of strontium salt and no attempt was made to determine absolute strontium contents. During a 20 minute measurement time, the system delivered a surface skin dose of approximately 6 mGy.

Animal strontium measurements revealed that essentially the entire strontium content measured at the skull site was associated with bone (Snyder and Secord, 1982). It was recognized that variations in thickness of the skull tissue influenced the measured strontium content, therefore, each individual strontium measurement was corrected using the elastic–to-inelastic ratio. Another interesting finding in the above-mentioned study is a pattern of maximum uptake one day after the strontium injection, followed by a constant decrease that was observed in both types of animals. A factor of 3 to 5 increase in concentration over the pre-injected strontium value in rabbit skull bone and 40 times in dog tibia bone was reported.

A second *in vivo* bone strontium XRF measurement was studied, using either ^{125}I or ^{109}Cd radiation sources, in an approximately 90 degree source-detector geometry relative to the sample position. The radiation dose delivered to the skin surface (~ 1 cm^2) was high at 10 mSv. Six post-mortem legs along with five amputated legs from dialysis patients were measured, along with eight normal volunteers (Wielopolski *et al.*, 1983b). Results suggested that XRF is a promising technique for bone strontium measurement. The measurement time was at least 45 minutes, and furthermore, on some post-mortem and amputated legs, part of the overlying tissue was removed during the measurements. A bone specimen from the measurement site was taken for atomic absorption analysis for quantitative calibration of strontium. Although healthy volunteers were measured in this

study, the areas of strontium characteristic peaks were not correlated to the strontium level in bone.

In vitro strontium measurements in various tissues have been successfully conducted in the last two decades as well. For example, human hair was measured for a variety of trace toxic elements in cancer patients by irradiation of the sample with 2 MeV protons, followed by acquiring the signal from emitted characteristic x-rays (Leung and Huang, 1997). The hair strontium levels in these patients showed notable fluctuations compared to levels in healthy subjects, but did not provide any useful information about the cancer treatment of the patient.

Russian scientists have analyzed strontium levels in human teeth using XRF with a ^{109}Cd source. Since teeth are part of the skeleton, these measurements may be treated as a bone strontium measurement. The bone strontium level was measured in patients with different bone diseases and the results showed a decrease of strontium concentration when patients suffered from osteomyelitis, chondroma, osteogenic sarcoma, malignant osteoblasto-clastoma etc. in comparison to healthy bone. Nevertheless, all these measurements were done *in vitro* (Zaichick, 1994).

Another invasive way to gain information about tissue strontium concentrations is through tissue biopsies. However, biopsy is painful, involves a risk to the patient and it also may not be possible to repeat it more than once.

A number of publications in medicine and archaeology report measurement of the Sr/Ca mass ratio in bone *in vitro* (Grynpas *et al.*, 1990) This ratio serves as an indicator of the diet which in turn may reveal information about a population's way of living, social status and habits. Three common techniques to determine the Sr/Ca ratio are:

atomic absorption spectrometry, plasma mass spectrometry, and neutron activation analysis. The only technique that might be applied for *in vivo* strontium measurement is neutron activation analysis, since it does not require bone removal from the subjects or its analytical preparation.

Fast neutron activation analysis can be used producing ^{87m}Sr via the $^{88}Sr(n, 2n)$ ^{87m}Sr reaction, which has a cross section of 220 mb at 14 MeV. The cross section increases to 260 mb at 17 MeV. The amount of strontium in bone can best be determined by observing the γ-rays at 388 keV (82 % branching ratio), which are produced from the decay of ^{87m}Sr with a half-life of 2.8 h. Using this nuclear reaction, the Sr/Ca mass ratio was measured in archeological bone samples, showing that it offers lower uncertainty than other commonly used techniques. Additionally, it allows for the samples to be preserved (Hult and Fessler, 1998). When 14 MeV neutrons are used for strontium activation, calculated fluence rate of the fast neutrons that will produce peak area with approximately 1000 count during 600 s irradiation time, was converted to the dose using neutron fluence-to-kerma conversion factor (Verbeke, 2000), giving the dose of approximately 120 mSv to the hand.

Neutron activation analysis has both advantages and disadvantages as an *in vivo* technique for bone strontium measurement in comparison to XRF. The most important benefit is that neutron activation analysis will not be as sensitive to attenuation of the signal in the overlying tissue. On the other hand, the radiation dose that needs to be delivered to the subject is much higher than the dose delivered by XRF (Part II - Section 2.7), imposing a limit for ethical approval for the procedure. In addition, the availability of a suitable neutron source, in general, is less than that of radiation sources for XRF, and

a neutron activation facility is not generally mobile and it is more expensive to setup and run than an XRF system.

Recognizing the advantage of having a better understanding of the role that strontium plays in the human body along with the need for a noninvasive, *in vivo* diagnostic procedure, this work concentrated on the development of a technique to measure strontium concentrations in the human body. Knowing that the target and storage organ of strontium is bone, the technique of x-ray fluorescence was developed to measure bone strontium levels in humans.

Chapter II

The Basic Components of Gamma Spectroscopy System

The technique of *in vivo* x-ray fluorescence has been used for clinical *in vivo* trace element analysis since the mid 1960s, with much of the pioneer work being done in Sweden and the United Kingdom. Elements from iron to uranium now have been measured in the human body, both at natural and elevated levels. There are several publications describing application of XRF in trace element analysis as previously cited, but each element needs careful consideration.

Many of the problems associated with *in vivo* elemental analysis have to be addressed, and many of them are in conflict with each other, thus a compromise must be reached. Two of the most important issues that control the overall design parameters of an XRF system are the amount of radiation delivered to a patient and the counting time. The upper limit on radiation dose is usually accepted as 0.01 Gy skin entrance dose

(Wielopolski, 1999), while the counting time is typically limited to less than 45 minutes. The major difficulty in fulfilling these constrains results from Compton scattering from the patient, that is predominately composed of low atomic number elements, leading to an unavoidable large background and a poor signal-to-noise ratio. Furthermore, due to Compton scattering, XRF spectra are usually collected under high count rate conditions, requiring a detection system with high count rate efficiency, high energy resolution and compactness, preferably mobile. The design of any XRF system, along with that for bone strontium, is a combination of the seven following components: radiation source, geometrical configuration, detector and electronics, data analysis, calibration and dosimetry.

A further common difficulty arises from the depth of the measurement site within the body, due to attenuation in tissue. This is even more restricted for bone strontium (Z = 38) measurement than for higher atomic number elements, due to low x-ray energies. Each of the components will be addressed separately, then the compromise arrived at for bone strontium XRF system design will be described.

2.1 Excitation Source

The excitation source type and energy is one of the critical components that must be selected carefully. The ideal excitation source should have the mean emission greater than, but close to, the element's absorption edge to be investigated. The closer this energy is to the element's K edge the greater the signal that will be generated, resulting directly

x-ray lines	Energy (keV)	Emission (relative to $K\alpha_1$)
$K\alpha_1$	14.1650	100
$K\alpha_2$	14.0979	52.0
$K\beta_1'$	15.83	24.4
$K\beta_2'$	16.08	3.0

Table 2.1 Strontium K-shell x-ray characteristics (Lederer and Shirley, 1978).

from the photoelectric cross-section which has the highest value just above the absorption edge of the element.

For *in vivo* analysis of superficial sites, where overlying tissue is thin, the maximum x-ray signal is obtained using a source with photon energy just greater than the appropriate shell energy. However, for deep-seated organs, where the attenuation of the incident photons is significant, a higher energy source may produce a greater detected x-ray yield. This is because, for higher energy sources, energy loss after a scattering collision need not reduce the photon energy below that of the shell edge. The scattered photon is thus still capable of producing x-ray emission in the target organ.

The K edge of strontium is at 16.1050 keV and it has several x-rays, as shown in table 2.1. Therefore, two suitable candidates for the excitation source, that have an energy above the strontium K edge, are ^{109}Cd and ^{125}I. The only practical energy for strontium excitation is above the element's K absorption edge, since the strontium L absorption edge and accompanied x-rays are below 2 keV, and thus, cannot be reliably detected during *in vivo* bone measurement due to attenuation by overlying tissue.

^{109}Cd emits a γ-ray at 88.035 keV with an emission probability of 3.61 %, accompanied by silver K x-ray lines at much lower energies as illustrated in table 2.2. These silver x-rays are approximately 26 times more intense than the 88.035 keV γ-ray

(Lederer and Shirley, 1978) and 6 to 9 keV above the K-edge, consequently, with the ability to fluoresce strontium.

Similarly, ^{125}I emits a γ-ray at 35 keV with an emission probability of 6.7 % together with tellurium x-rays at energies closer to the strontium K-edge. Nevertheless, the energy difference between the strontium K-edge and tellurium lines is larger, being 11 to 19 keV.

Isotope and accompanied low energy radiation (keV)	Half-life (days)	Principal γ-ray energy (keV) (emission probability in %)	Photoelectric absorption cross section for strontium (cm^2/g)	Energy of main Compton peak (keV)	
				90°	180°
^{109}Cd	462.6	88.035 (3.61 %)	0.95	75.10	65.45
Ag lines		22.16 (78 %)	48	21.24	20.39
		24.94 (16.66 %)	34.9	23.78	22.72
^{125}I	59.408	35.49 (6.7 %)	13.1	33.19	31.17
Te lines		27.4 (118.6 %)	26.9	26.00	24.75
		31(22.2 %)	19.1	29.23	27.65

Table 2.2 A comparison of the characteristics of the possible isotopic sources for strontium x-ray fluorescence measurement.

The smaller energy difference between the strontium K-edge and excitation source energy is for ^{109}Cd, resulting in the higher photoelectric absorption cross section for strontium (table 2.2). This means that ^{109}Cd will give rise to a more intense strontium signal per unit incident flux, as the photoelectric cross section of strontium is larger for this photon energy than the corresponding value for ^{125}I. In addition, this source has a longer half-life that is more suitable for a clinical environment, compared to the ^{125}I source with a short half-life that needs to be changed more often. Also, there is the immediate availability of the ^{109}Cd source for routine bone lead measurement that is

performed in the laboratory, and therefore no specific additional cost to this project. As a result, a ^{109}Cd excitation source was chosen as the excitation source for strontium bone measurement. The source has been purchased encapsulated in a stainless steel capsule having a cylindrical shape with a diameter of 6 mm and height of 4 mm.

Based on all facts mentioned above, ^{109}Cd was used throughout this work. However, at both 90° and 180° geometries Compton peaks of ^{109}Cd source are positioned close to the strontium x-ray lines, thus contributing to the background below the strontium peaks and lowering signal-to-noise ratio. This was more prominent when 180° was applied compared to 90° geometry. In the case of ^{125}I source, however, Compton peaks are at higher energies, and as a result this source might give lower background below the strontium x-rays, and consequently better signal-to-noise ratio. Nevertheless, more data are needed to answer this question clearly.

Combined with the interaction probability and the half-life of the excitation source, the optimization of Compton and coherent peak positions relative to each other, as well as to the strontium x-ray peaks has to be investigated through the source-sample-detector geometry.

2.2 Geometrical Configuration

At low photon energies (10 – 150 keV), scattering with atomic electrons is the dominant scattering process. The two scattering processes of importance are coherent (Rayleigh) scattering and incoherent (Compton) scattering. Coherent scattering is the

elastic scattering of a photon from an atom, which results in the emission of a photon with unchanged energy. Compton scattering is an interaction between a source photon and an electron in the absorbing sample, in which the photon is incident on a stationary, free electron as a first approximation. Therefore, the scattered photon will have reduced energy. The use of low energy photons favours coherent scattering since the cross section decreases rapidly as the photon energy increases. A small scattering angle favours the fluence rate of coherently scattered photons, which are highly forward directed. However, the choice of small scattering angle and low photon energies introduces difficulty in resolving the coherent peak from the large distribution of incoherently scattered photons in the recorded pulse height distribution.

The magnitude of the background in the characteristic x-ray energy region originates predominantly from Compton scattering, due to the fact that the human body is a thick sample with low atomic number materials. The excitation source, together with the sample-source-detector geometry, may affect the Compton peak position, and consequently, change the energy separation between the strontium x-ray and coherent peaks, as well as the x-ray and Compton peaks. Table 2.2 lists the energies of the Compton peaks for the ^{109}Cd radioisotope for the two commonly used geometry configurations for XRF, 90 and 180 degrees.

It is important to observe that the position of the Compton peak with the ^{109}Cd source is at higher energies than the characteristic strontium x-ray peaks for both proposed geometries. Therefore, scattered radiation contributes to the continuum between zero energy and the Compton peaks, degrading the signal-to-noise ratio in the strontium peaks. Moreover, the coherent and Compton peaks are positioned in close proximity, and

therefore hard to resolve. If this is the case, it prevents simplification of *in vivo* bone strontium assessments, as will be analyzed and discussed in Chapters III and IV (Part II).

One of the important characteristics of this XRF system is that strontium may be activated by both primary photons and photons that undergo Compton scatter in the sample. The ideal XRF system, when fluorescence x-rays are normalized to a coherent scatter signal, requires that the element under investigation be activated only by the primary photons. Unfortunately, this cannot be achieved with either the ^{109}Cd or ^{125}I radioactive source configured in a 90 or 180 degree geometry in respect to the detector.

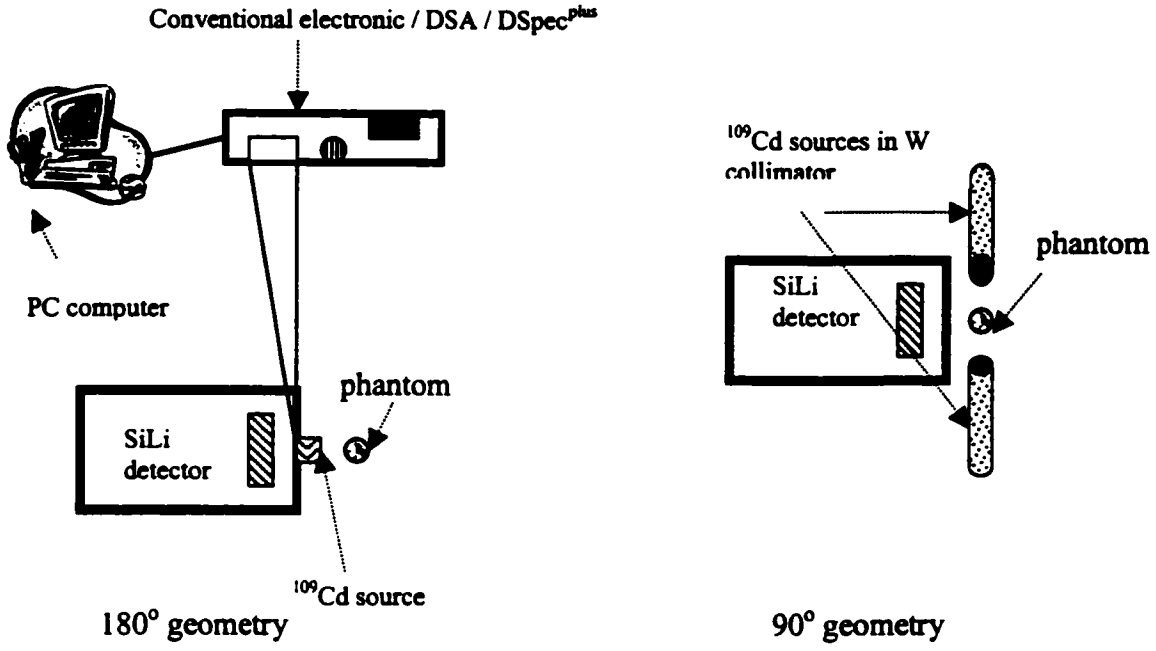

Figure 2.1 Experimental set-up for the 180 and 90 degree source-sample-detector geometries studied for the bone strontium XRF system.

To investigate the difference between the 90° and 180° geometries, a high concentration strontium bare bone phantom was measured in these two positions, the experimental set-ups for which are depicted in figure 2.1. The geometry investigation for strontium bone measurement was done using a plaster of Paris bone phantom (see Part II - Sec 2.5 for more details), that was measured in a 90 degree geometry either using one or two collimated sources, or in a 180 degree source-sample-detector geometry with one radiation source. Note that all measurements discussed in this section are performed using a SiLi detector.

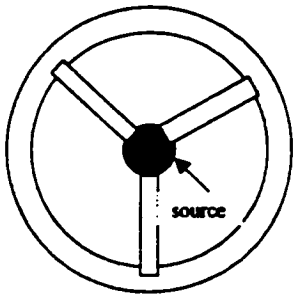

Figure 2.2 Radiation source holder used during backscatter geometry configuration that is placed onto front face of the detector.

When backscatter geometry was used, the radiation source was placed in a tungsten capsule and mounted in front of the detector, in its center, using a specially designed plastic holder (figure 2.2). Recognizing the high attenuation of all signals that are collected during strontium XRF measurement in most materials, the holder is designed to cover the detector's surface area as little as possible while holding the radiation source in position. In comparison with the holder that is routinely used for bone lead XRF measurement, the plastic front face has been removed and only three thin arms were retained to support the encapsulated source in place, opening the rest of the detector's front face to the radiation. The tungsten capsule had an

open, unfiltered front face, thus the source was irradiating the sample while the detector was shielded from the incident radiation.

When a 90° geometry is used, however, the radiation source must be placed in a collimator (cylinder; height 4 cm, outer diameter 2 cm, inner diameter 1 cm). Throughout these experiments, a tungsten collimator with an approximate 7° collimation angle (O'Meara, personal communication) was used. The radiation source was at 2.43 cm from the front surface of collimator; therefore, this is the minimum distance between the source and sample at the 90 degree geometry.

Spectra acquired (1800 s of real time) from a phantom with a high strontium level are presented in figure 2.3. Strontium x-ray characteristic peaks, as well as the coherent and Compton peaks that are detected, are labeled on the figure.

A significant difference in the strontium activations between the 180 and 90 degree geometries is observed. Higher strontium activation is detected at the 180 degree accompanied with higher background below the characteristic x-ray peaks in comparison to the 90 degree geometry, due to different scattering of incident photons at these two geometries. Once the *in vivo* strontium measurements started, it was observed that the background at both geometries increased significantly due to the additional scattering from overlying soft tissue. The background at the 180 degree geometry increased so much as to completely mask the strontium x-rays.

When the 180 degree is used, a peak at 16 keV is noticed that is situated in the upper energy side of the strontium Kβ peak, and cannot be fully resolved from it with the currently used SiLi detector and electronics. The source of this peak is unknown; nevertheless, it is not detected in the 90 degree geometry, suggesting that it might be a

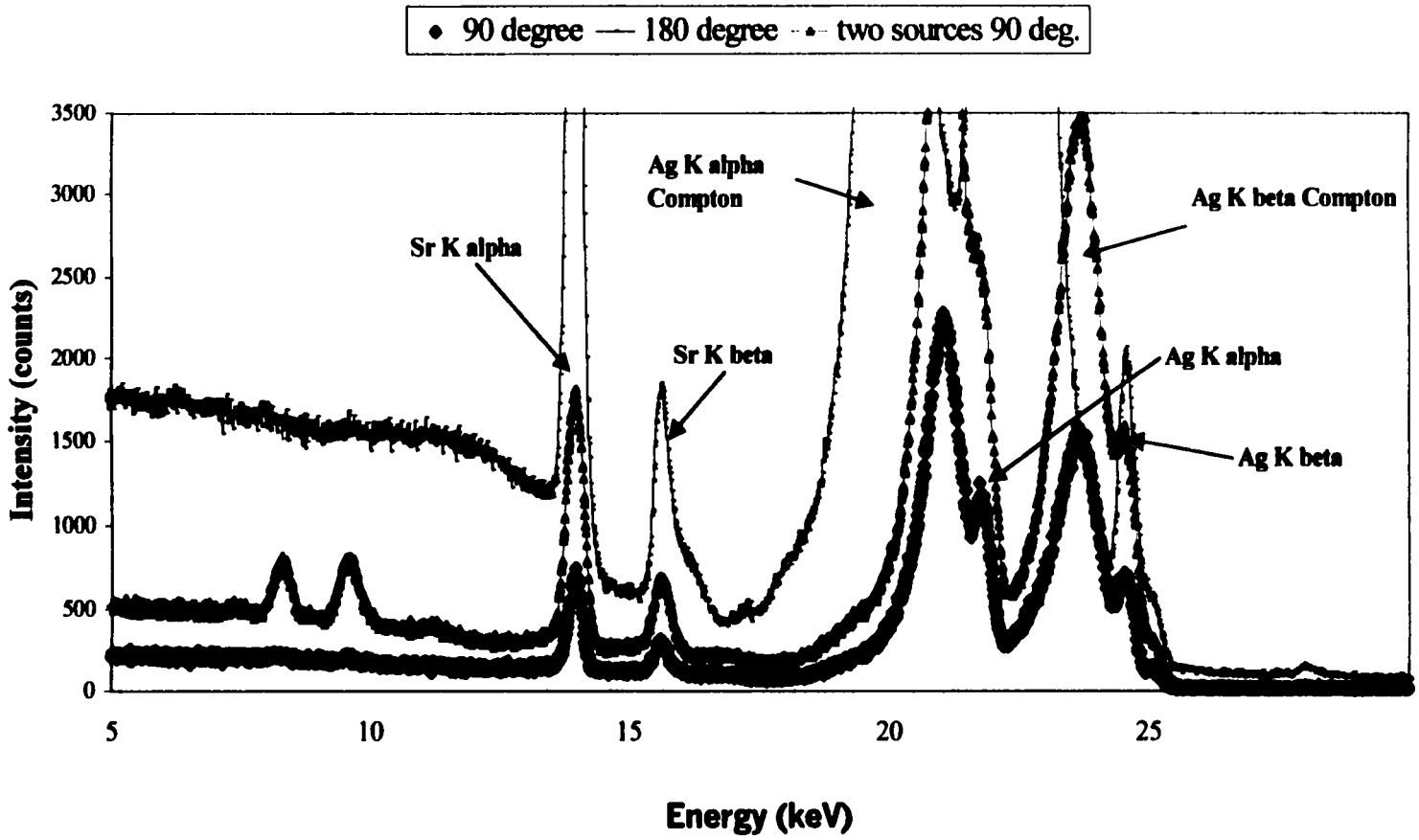

Figure 2.3 Spectra acquired during the investigation of different source-sample-detector geometries for the bone strontium XRF system. A high concentration strontium bone phantom was measured in 90° geometry using either one collimated ^{109}Cd source (blue spectrum) or two sources (red spectrum). The figure contains a spectrum from same bone phantom measured in 180° geometry as well (green spectrum).

scattering peak. A long measurement of zero added strontium phantom contained this peak as well, while the strontium x-ray peaks had very low intensity, clearly eliminating the possibility that this peak was strontium $K\beta_2$ peak, at 16.08 keV energy. Since there is only one unidentified peak in the spectra, it is concluded that this is not a characteristic x-ray peak of some element, which is unintentionally present in the view of the source and detector.

Energy separation between the Compton and coherent peaks is higher for the 180 degree than that of the 90 degree source-sample-detector relative position (table 2.2). Nevertheless, because of more photons collected from the 180 degree geometry that underwent Compton scattering, the two Compton peaks have large widths, and thus, the coherent peaks are positioned in their tails. The coherent peaks are not fully resolved from Compton peaks for the 180 degree, independently of the electronics used for signal processing (see Part II – Sec. 2.4 for more details). Although not completely resolved, due to the limited energy resolution of the detector and their small energy difference, the Compton and coherent peaks remain distinguishable from each other for the 90 degree geometry. In the attempt to investigate further the 90 degree geometry that exhibits less strontium activation but a better signal to background ratio as well as an unobstructed strontium Kβ peak and resolved Compton and coherent peaks, two radiation sources were used. Double the activation is achieved, however, the use of two irradiation sources was found inconvenient for positioning during *in vivo* measurement (Part II - Chapter IV).

Furthermore, once the complete XRF strontium system was assembled and a pilot *in vivo* study started it was observed that the signal to background ratio was significantly more degraded in the *in vivo* spectrum of bone strontium, due to the presence of soft

tissue between the bone site and the detector or source. This effect was more prominent at the 180 than at the 90 degree geometry due to the significant increase of the background below the strontium characteristic x-rays, further suggesting that a 90 degree geometry should be used for the strontium XRF system. All these observations suggested that a 90 degree geometry between the source, sample and detector should be used for bone strontium assessment.

Therefore it was established, that strontium XRF bone measurements should be performed using a collimated ^{109}Cd radiation source positioned in a 90 degree source-sample-detector geometry. The next step in the development of this system was to select a detector and signal processing electronics with optimal resolution and throughput of the acquired signal for this specific use.

2.3 Detection System

The weakness of the x-ray signal and complexity of the measured strontium spectra demands a detector with high count rate and efficiency capability, as well as high energy resolution. The selection of an appropriate detection system is largely based on the energy of the signals being recorded from the target element.

The two most widely used solid state detectors in XRF detection are hyper pure Ge detectors for energies above 30 keV, and SiLi detectors for lower energies typically used for L XRF systems of high atomic number elements ($Z > 50$), or K XRF systems for low atomic number elements with emitted x-rays in the 1 to 30 keV energy region. In both cases, the detection efficiency depends upon the surface area and thickness of the semiconducting crystal, while the resolution of the detector affects the lower limit of detection. The better the resolution the smaller the fraction of the background counts under the x-ray peaks of interest. Both detectors operate at liquid nitrogen temperature, which necessitates a dewar making their use cumbersome. Moreover, their prices are comparable.

Although large-area detectors suffer from lower energy resolution, their high geometrical efficiency means that it is widely accepted that they should be used when measuring a single element (Wielopolski, 1999, Mattson and Scott, 1989), if there is not another element in the human body with peaks or scattered radiation to interfere with the element under investigation.

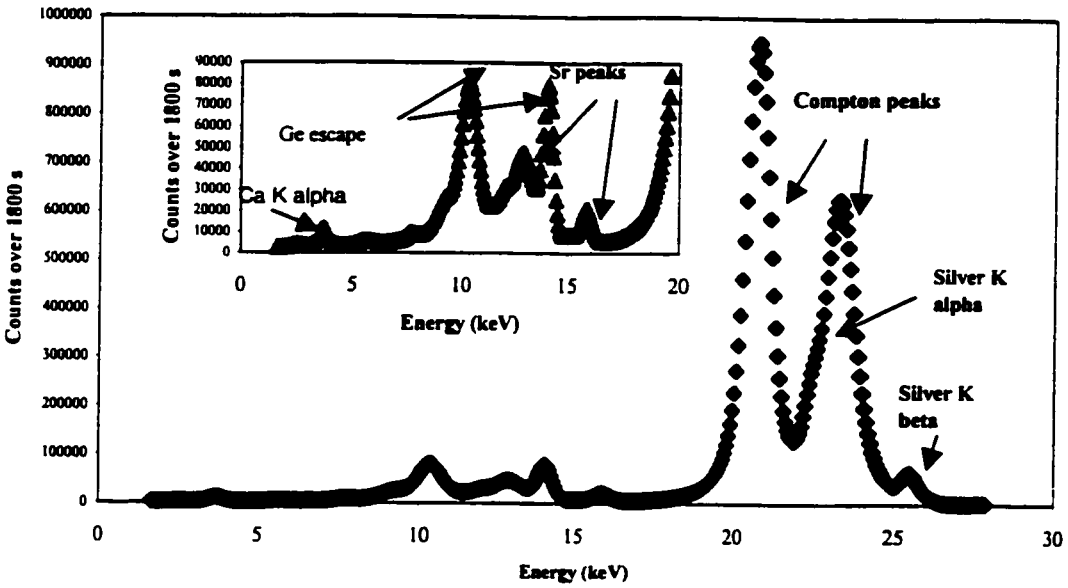

Figure 2.4 Spectra acquired using a pure Ge detector. The water phantom was positioned at a 90 degree geometry. Spectrum contained prominent Ge escape peaks in the strontium x-rays energy region. The HPGe detector was incapable of resolving the silver Kα x-ray from the Compton peak.

Due to the immediate availability of a hyper pure Ge detector, it was used for measuring phantom spectra at the beginning of this project, while investigating other components of the bone strontium XRF system. Preliminary strontium solution measurements were done using a hyper pure Ge detector with a diameter of 50 mm, a thickness of 20 mm, and a resolution of 700 eV at 122 keV for a pulse shaping time 1 μs (O'Meara, 1999).

Figure 2.4 presents pulse height spectra of the strontium water phantom acquired with the HPGe detector and conventional electronics. Although the strontium characteristic x-rays are successfully measured, the spectrum is very complex due to the presence of the escape peaks that are positioned approximately 10 keV below each

measured peak. For example, the escape peak from the prominent 25 keV Compton peak is positioned between the strontium Kα and Kβ peaks.

Beside the unsuitable position of the escape peaks as the most important motive to replace the HPGe for a different detector, it is interesting to point out that the water phantom spectrum had very low intensity coherent peaks, as labeled on figure 2.4. Since the probability of coherent scatter is directly proportional to Z^2 and water has low atomic number, very few photons underwent this type of scattering when the strontium water solution was irradiated.

Moreover, in the energy region of interest, it was anticipated that the resolution of this detector should be worse than for a silicon detector, further supporting the decision to purchase the more appropriate solid state detector for this application – a SiLi detector.

In a silicon detector, the photoelectric effect is more probable than Compton scattering for photon energies below about 55 keV (Knoll, 1989). At energies below 30 keV the photoelectric effect is predominant, thus the response function of a SiLi detector to photons below this energy is dominated by a single full-energy peak caused by absorption of the photoelectrons. If the electric field in the detector is high, charge collection is complete and the peaks shape can be represented adequately by a Gaussian function (Part II - Section 2.5).

Some photoelectric absorption causes prompt emission of characteristic x-rays as the result of electron reorganization in the electron shell. At low energies of incident photons most of the absorption occurs near the surface of the detector, where the escape of resulting silicon x-ray peaks can be significant. The result is the appearance of a small x-ray escape peak in the spectrum, that in silicon will be located 1.8 keV below the full-

energy peak. As illustrated in figure 2.4, the corresponding escape peaks in a germanium detector spectrum are much more prominent because of the smaller average penetration distance of the incident radiation and the greater probability that the Ge characteristic x-rays will escape due to their higher energy (Knoll, 1989). The fluorescence yield in Ge (50 %) is much larger than that in Si (5 %), so that the probability of emission of a characteristic x-ray is also higher (Lederer and Shirley, 1978; Knoll, 1989).

The commercially produced low energy photon spectrometer (ORTEC) consisted of a cooled SiLi detector, preamplifier and liquid nitrogen dewar (30 l volume). Its recommended operating bias was negative 1000 V. For low-noise performance, the input stage of the preamplifier is cooled as well to reduce electronic noise. A preamplifier with pulsed optical feedback (Model 239 POF) was integral to the detector and therefore used in conjunction with either conventional or digital electronics, as will be discussed in the next section.

Recent improvements in technology of semiconductor detector resolution have allowed full-width-half-maximum values as low as 100 eV for small area detectors. Nevertheless, the SiLi detector that was used in this work has a surface area of 200 mm^2, and an energy width of ~ 200 eV at 5.9 keV. An ^{55}Fe source successfully reproduced the ORTEC specified resolution upon purchase. The energy – dependant efficiency of the SiLi used is close to 100 % in the energy region from 5 to 20 keV. The efficiency at low energies is critically dependant on the thickness of the window materials associated with the detector and cryostat. Thus, the thinnest available beryllium window of 0.05 mm thick was ordered with the SiLi detector.

For these reasons, a SiLi detector has been used as the detector for the *in vivo* K-shell x-ray fluorescence measurements of strontium in human bone, that will be further discussed throughout this work.

2.4 Performance of Different Electronics with the SiLi Detector

The performance of two new digital spectroscopy systems, that have recently become available, was investigated and compared to a conventional analogue system for ^{109}Cd XRF measurements of bone strontium.

In the conventional analog system, signal processing is done using an analog amplifier (Ortec Amplifier Model 572), and a fast analog to digital converter (Canberra Fast ADC Model 8715), where the amplitude intensity of the amplified signal from the SiLi detector is converted to a digital code. Due to high count rates, pulse pile-up rejection is utilized to reduce background. The best resolution was obtained when a 10 μs shaping time was used, successfully resolving all the required peaks in the spectrum. The major limitation of the conventional system is low throughput, nevertheless, the analog system was set to approach the resolution measured with the digital electronics for comparison. The digital code was stored and analyzed by S 100 (Canberra) software with a multi channel analyzer to increment the appropriate channel in the spectrum, together with real time monitor display. These electronics will be referred to as the conventional system.

An alternative type of signal processing has become commercially available, which uses digital signal processing. The advantage of digital spectrometers is the ability to filter the signal digitally, which should result in higher throughput without losses in resolution. As well, digital spectrometers provide better long-term stability of both resolution and peak shape. In 1996, the ORTEC DSPEC was introduced to the market, followed with a second generation, the DSPEC^{PLUS} that was promoted in 1999. Competing with ORTEC, Canberra produced its version of a digital signal processing unit, the DSA-2000, in 1997.

The DSPEC^{PLUS} was used with its accompanied Maestro software that allows control of the DSPEC unit, a high voltage supply to the detector as well as quantitative analysis and storage of spectra. The DSPEC^{PLUS} replaces both amplifier and ADC components of the analog system. It filters pulses digitally, using a quasi-trapezoidal filter to enhance the system signal to noise ratio, rather than the triangular filter that is employed in the analog system.

In the conventional analog system, changing the shaping time constant changes the rise and fall time in the triangular filter. The new digital system allows the researcher to adjust more constants, namely the rise and fall time, the width of the flat top, and the cuspiness (concave shape of the rising and falling edges) of the rise and fall times on the trapezoidal filter. To optimize the DSPEC^{PLUS} for any detector and application, the software offers a wide range of these settings. Additionally, it has an automatic "optimize" function that combines the choice of flat top and pole zero adjust into one simple operation.

Bone strontium measurements were performed at different rise times, flat top and cusp constants to determine the best setting in respect to the throughput and resolution of this system. Firstly, the rise time was changed from 0 to 23 μs in steps of 2 μs, while keeping the flat top and cusps constant. With low rise time highest throughput was achieved, while at high rise time the best resolution of the peaks can be measured using the Maestro software. More significant change in the resolution could be observed than in the peak or total spectra throughput when the rise time was changed. Between 10 and 14 μs rise time, no significant change was noticed either in the resolution or in the throughput. Thus, 12 μs rise time was selected as the optimal rise time. Secondly, cusp constant of the filtering function was evaluated, keeping the rise time at the selected value and the flat top at 0.9 μs as before. The DSPEC^{PLUS} offers only 6 cusp parameter values. The best system performance was achieved at 0.9 μs cusp constant. The last parameter, flat top, was evaluated using the chosen rise time and cusps while varying the flat top from 0.8 to 2.4 μs. The flat top was selected as 0.9 μs, since very small changes in the peak resolution were noted as well as in the throughput when this parameter was varied. Once all the parameters were selected, the high concentration phantom was measured three times to compare system performance with the analog system and the DSA-2000 digital system.

The DSA-2000 digital spectrometer system replaces the same parts in the analog electronics as the DSPEC^{PLUS}. It, also, filters and shapes the pulses digitally immediately from the preamplifier and the signal is filtered using an internal algorithm. This digital system produces a trapezoidal pulse shape like the previously discussed digital system. There are 35 possible rise and fall times, and 21 possible flat top times built into this

system that is controlled by Genie-2000 software. The software was installed on a personal computer linked to the DSA by an Ethernet connection. The detector's high voltage supply is controlled by the unit and software. A similar evaluation of all the parameters that define peaks was performed to that for the DSPEC^{PLUS} system. Final DSA-2000 system set up was rise/fall time of 12 μs, and the flat top at 0.9 s, since the system does not offer the adjustment of the cusps time. With these parameters optimal resolution was achieved with the largest throughput, while the silver Kα peak was well separated from lower energy Compton peak in the spectrum.

Before discussing, however, the performance of different electronics it is necessary to emphasize that DSA-2000 digital system is designed for use with germanium and sodium-iodide detectors. Therefore, there is not an option for the SiLi detector that is built into the software setup. After consultations with Canberra, the system was set as it would be connected to a germanium detector, and then, the rise time and flat top were selected.

Strontium spectra were acquired, 300 s in length, using each of these three electronics and a high concentration phantom placed 2 cm from the detector's surface in the 180 degree geometry. Each measurement was repeated three times. Each system offers different programs for data acquisition and analysis, therefore, to ensure the same data analysis all spectral data analysis was completed using the Marquardt nonlinear least square fitting routine that will be discussed later in this chapter (Section 2.5). As illustrated in table 2.3, comparison was made using the following quantities: energy resolution, throughput of the strontium Kα characteristic peak and its precision, and total spectral throughput.

Comparable energy resolution with all three electronics has been achieved, although the analog electronics were set to approach this resolution neglecting its throughput. As a result, the conventional analog system had both the lowest peak and total throughput. The analog and DSA-2000 electronics presented the same energy resolution that is worse than that achieved using the DSPEC^{PLUS}. The DSPEC^{PLUS} achieved the energy resolution 272 eV at of the strontium characteristic peak, accompanied with 80 % of the total throughput in comparison with that of the DSA-2000 digital electronics. Moreover, DSPEC^{PLUS} had the highest peak count throughput and the best peak precision.

	Peak Throughput (counts)	Peak Precision (%)	Total Throughput (counts)	Energy Resolution at 14 (eV)
Conventional electronics	35247	0.97	1862111	322.76
DSPEC^{PLUS} Ortec	227609	0.38	8396094	271.63
DSA – 2000 Canberra	205171	0.41	10406880	323.93

Table 2.3 Performance of different electronics with the SiLi detector. Data were acquired using one high concentration phantom positioned in a 180 degree source-sample-detector geometry. Data analyzes was done with a fitting routine developed for the strontium system.

In addition to all results presented in table 2.3, it is necessary to mention that the DSPEC^{PLUS} unit used was on limited time loan from ORTEC, as well as that it was a prototype model. Thus, recognizing its superior performance to the conventional electronics or DSA-2000 digital unit for this specific application, further experiments were done using the DSA-2000 digital spectrometer.

Improvements in throughput achieved with digital electronics should lead to greater precision in bone strontium measurements, which should lead to a reduction in the minimum detectible limit of the system. From the conclusions in terms of throughput and resolution performance of the digital and conventional systems, the digital spectroscopy system should be used for the bone strontium XRF system.

2.5 Data Analysis

The objective of data analysis is to evaluate the intensities, via the areas or heights of peaks, in the pulse-height spectrum for the strontium characteristic lines. *In vivo* XRF spectral data are complex with very low line intensities and possible distortions, which require some processing before the final line intensities can be established.

McMaster's trace element group utilizes a non-linear least square fitting routine developed by Marquardt in 1963 (Bevington, 1992). This fitting routine has been successfully applied to bone lead, mercury, cadmium, manganese and aluminum data analysis. Therefore, the non-linear least square fitting routine has once more been adjusted, but for bone strontium data evaluation.

The strontium x-ray region was fitted with two Gaussian peaks, with linked amplitudes and positions, on a linear background. Similarly, each silver coherent peak was fitted with one Gaussian peak on one exponential background.

Once the amplitudes of peaks were determined it was possible to generate calibration lines, as the characteristic x-ray amplitudes plotted against Sr to Ca ratio, or as the ratio of the intensities of x-ray to coherent signal versus Sr to Ca ratio.

2.6 Calibration

The calibration converts the estimated peak intensities or areas into element concentrations expressed in standard units. The high subject variability makes this task difficult in any *in vivo* quantitative analysis of a trace or minor element. Because of the strontium x-rays' low energies, the peak intensities are strongly affected by attenuation in the matrix, and the distribution of strontium in the bone. It is also affected by the volume or mass that is sampled. Since normal subjects have low strontium levels, it is difficult to develop calibration phantoms that can account for subject variability and, at the same time, properly represent human tissue at the characteristic x-ray energies. However, in order to test the precision of new system design, a calibration has to be performed using materials that simulate the subjects as closely as possible, for which the system was designed.

Based on physical parameters and experimental observation, and prior to the pilot *in vivo* measurements, two sets of plaster of Paris phantoms that simulate bone were constructed. However prior to that, a set of strontium chloride water solutions was made and used during system design evaluation.

Phantom material was selected to exhibit similar photon interaction cross sections to the tissue being modeled. For bone strontium measurement, the ideal phantom has to simulate human bone and overlying tissue. Firstly the bone materials are discussed, and then briefly, the soft tissue materials.

At McMaster, the standard material used to simulate bone in the XRF systems is plaster of Paris ($CaSO_4 \bullet 1/2H_2O$). Since it is commercially available, a bone equivalent

plastic had been investigated as well. As illustrated in figure 2.5, plaster of Paris and bone equivalent plastic exhibit similar attenuation to that of cortical bone at the energy range of strontium x-rays and coherent peaks. It is also observed that the ratio between the mass attenuation coefficient of plaster of Paris and cortical bone has constant a value of 1.47, and the corresponding ratio between bone equivalent plastic and the plaster of Paris is 0.68, suggesting that both materials may be used for bone simulation. Nevertheless, plaster of Paris has been used simply due to the price difference and immediate availability, as well as the fact that the phantom is formed from powder by adding water and a known amount of strontium, resulting in undemanding synthesis of the bone phantoms.

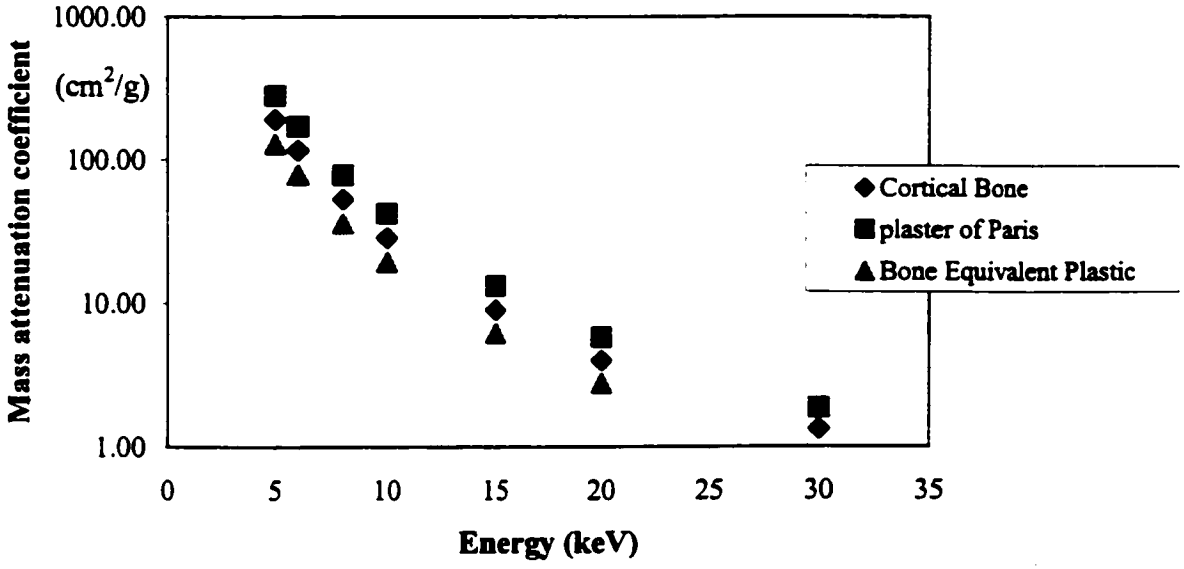

Figure 2.5 Mass attenuation coefficients for cortical bone and possible bone simulation materials for phantom construction.

Six strontium doped plaster of Paris phantoms (cylinders; 3.5 cm high and 3.6 cm diameter) were prepared (marked 1 to 6, named "euro set"). The strontium concentrations

in the phantoms were: 0, 0.22, 0.44, 0.93, 2.15 and 4.57 mg of added strontium per gram of calcium. The calibration procedure revealed that the plaster of Paris used contained strontium as a trace element at approximately (4.2 ± 0.1) mg Sr/g Ca. Therefore, another effort was made to lower the contamination by constructing a second set of bone phantoms (cylinders; 3 cm high and 3.5 cm diameter) using high purity, pharmaceutical, plaster of Paris from Europe. Ironically, this set of phantoms contained even more strontium as a tracer (approximately (5.9 ± 0.2) mg Sr/g Ca). This second set (marked with letters a to f, and named "pharmaceutical set") contained phantoms with 0, 0.18, 0.46, 1.18, 2.09 and 4.30 mg of added strontium per gram of calcium. The associated uncertainty of strontium concentration in both sets of phantoms was 0.01 mg Sr/g Ca. Once the calibration line was generated, the phantom with 1.18 mg Sr/g Ca had to be rejected due to an unrealistic number of counts, and therefore, distortion of the calibration line. It is useful to mention again that bone strontium levels in normal subjects are estimated to vary between 0.1 to 0.3 mg per g of calcium.

Phantom set	Slope ± σ (slope) (counts/(mg/g))	Intercept ± σ (intercept) (counts)	r^2 value	Strontium contamination (mg Sr /g Ca)	MDL (mg Sr /g Ca)
Euro set					
Kα	79 ± 1	323 ± 3	0.995	4.08 ± 0.08	0.11
Kβ	14.1 ± 0.3	62 ± 1	0.976	4.4 ± 0.1	0.44
Pharmaceutical set					
Kα	56 ± 2	328 ± 3	0.987	5.8 ± 0.2	0.17
Kβ	10 ± 1	66 ± 1	0.989	6.6 ± 0.6	0.75

Table 2.4 Data of regression analysis of two sets of phantoms, called euro and pharmaceutical.

Comparing the calibration parameters of the two sets of phantom it may be seen that the calibration slope of the euro set is larger by factor of 1.4 than the slope of the pharmaceutical set. Recently it has been learned that plaster of Paris, that is believed to be $CaSO_4 \bullet 1/2H_2O$, can contain a significant amount of $CaCO_3$ (unspecified by company) that would result in the different densities as well as surfaces of the built phantoms. During phantom preparation it was noticed that the two plasters behaved differently; for example, more CO_2 was released from euro plaster and it needed a longer time to set. In addition, the pharmaceutical plaster was smoother powder than the plaster bought in Europe. The diverse chemical composition of plaster of Paris might lead to a different attenuation of the signals in the phantoms, resulting in the different values of the calibration slope.

The minimum detectable limit for each strontium x-ray line and for both sets of phantoms was calculated using a common formula:

$$MDL = 2 * (\sigma \text{ (intensity of concentration of zero phantom)} / \text{slope}$$

With the slopes listed in table 2.4, and the uncertainties in the strontium peaks for the blank phantom spectra, once again the euro set of phantoms performed better with a lower minimum detectible limit. Therefore, the euro set of bone phantoms was used for any future strontium bone estimations throughout this work.

Currently, phantoms have not been designed to model overlying soft tissue. Nevertheless, it was established using the same approach as for materials to simulate

human bone, that either water or soft tissue plastic should be used to simulate human soft tissue (data not shown).

The strontium characteristic x-rays require intensity correction due to strong signal attenuation by the overlying tissue. Consequently, only bone near to the surface can be measured. It is anticipated that the soft tissue thickness will be measured prior to in *vivo* XRF strontium measurement, providing necessary information about signal attenuation, and subsequent correction for the estimation of strontium levels in bone.

Considering all the problems in building pure calibration phantoms as well as the significant signal attenuation in soft tissue, the best approach for absolute validation of *in vivo* bone measurement might be to use an actual human organ, i.e. cadaver amputated finger. A small sample taken from the measurement site in the organs being used as standards then can be analyzed with alternative standard technique such as atomic absorption, mass spectrometry or any other valid analytical method.

2.7 Dosimetry for Strontium Finger Measurement

A fundamental issue for *in vivo* elemental analysis is that it is performed on humans and, therefore, is limited by the radiation dose that can be delivered to the patient. Thus, the strontium XRF system for *in vivo* analysis is no different from any other XRF system and, before it can be used on any subject it requires dosimetry assessment.

The dose is determined from the exposure rate using an NEL 600 cm^3 ionization chamber (type 2575) with Farmer Dosimeter (type 2570). The response of this system has been calibrated against a source, ^{60}Co, at Health Physics at McMaster over a long period of time. Thus, the exposure rate of the ^{60}Co source was measured and calibrated at the ^{60}Co photon energies. The source strength was measured three times at a distance of 1 m from the source to ensure field uniformity and validity of the $1/r^2$ field dependence. Each measurement was corrected for atmospheric pressure and temperature, using the Farmer Dosimeter's internal correction, since the chamber contains vented air and its volume depends on these variables. As recommended, acclimatization of the chamber involved exposure of the chamber to at least 2 R in order to ensure stability in its response to the following measurement. Measurements determined that the ^{60}Co source exposure is 39.86 mR in 30 minutes at 30 cm distance, the distance used in routine calibration procedure. Uncertainty of this value is usually cited as 5 % based on the National Research Council, Canada (Ottawa, ON), where the chamber was originally calibrated.

Two ^{109}Cd source measurements were performed. The first was 30 minutes measurement at 30 cm from the bare, uncollimated source and the measured source exposure was 1.04 mR. The second measurement was at 6.5 cm distance, and the ^{109}Cd source was placed inside the tungsten collimator, which is used for bone strontium measurement at 90 degree geometry. The source exposure was 1.50 mR in 30 minutes at the time of measurement. At each distance the source strength was measured three consecutive times.

Both, calibration source and ^{109}Cd, were measured using "A" window (Melinex, thickness 25 mg cm^2), which is suitable for measuring exposure in air to photons in the

energy range of 20 to 250 keV. The energy response of this system had been measured and well documented, relative to ^{60}Co, and these data were used to correct (correction factor of 4.95 mR/nC) the exposure to true exposure recorded from the ^{109}Cd source (Heinmiller, 1988). Using the same window, but without the radiation source in the room, a background was measured and all data were corrected prior to any further calculation.

Once the true exposure rate in the air is known, it has to be converted to absorbed dose using a standard expression relating exposure in dry air and dose to skin and/or bone, D_m, given as

$$D_m = 34 \cdot X \frac{(\mu/\rho)_m}{(\mu/\rho)_{air}}$$

where X is the exposure, (μ/ρ) is the mass energy absorption coefficient for skin, bone and dry air. These coefficients are energy dependent, hence, the weighted ratio of these coefficients was used to convert the true exposure to dose for all energies emitted by the source.

For general screening purposes and for patients, an entrance dose to a small area of the skin of 10 mGy might be a guideline for dose (Wielopolski L., 1999). However, the dose delivered to a small area of the skin during bone strontium measurement is 6.56 mGy (0.07 cm^2) and only 0.46 mGy (0.68 cm^2) at a 2.5 cm distance from the source from bare and collimated source, respectively. Therefore, these skin doses are considered to be at acceptable level for the x-ray fluorescence system.

In order to quantify the total (effective) dose delivered to the patient, the absorbed dose to the skin and bone surface was corrected using the irradiated area (Todd *et al.*,

1992). The assumption was made that both the skin and bone surface, are exposed to the same radiation field, neglecting attenuation due to the overlying soft tissue that is present for an *in vivo* measurement. Thus, this will be a conservative estimation of effective dose. The dose to skin is calculated as 40 and 27 nSv from the bare and collimated source respectively. The corresponding doses to the bone surface are 11.7 and 7.7 μSv. The effective dose to the subject, therefore, will be approximately 120 or 80 nGy during a 30 minute measurement time, depending whether the bare or tungsten collimated ^{109}Cd source is used.

Since the attenuation of incoming radiation is neglected, the effective dose is dominated by the dose delivered to the bone surface. Furthermore, one can calculate that only approximately 17 % of silver Kβ will be attenuated by 0.3 cm thick overlying soft tissue. Thus, the overestimation of the dose that will be delivered with this fluorescence system is minor.

Due to the similarity to the bone lead system, the estimated effective dose can be compared with the effective dose equivalent from a typical tibia lead exam which has been accurately determined to be 34 nSv for a half hour measurement (Todd *et al.*, 1992).

Given that there are a couple of differences between the two systems, it is anticipated that a bone strontium XRF measurement should deliver a higher dose to the patient than the lead system. The two ^{109}Cd sources did not have the same activity and size. Hence, they irradiated different skin areas. The source activity of the lead system was 7.4 GBq with a 0.09 cm^2 of skin area, while the source used for bone strontium measurement had an activity of 0.8 GBq with a skin area either of 0.07 cm^2 (bare source) or 0.68 cm^2 (collimated source) exposed to it. While the ^{109}Cd source used for strontium

activation was just positioned in the center and in front of the detector, the source applied for the lead measurement had a 0.5 mm thick copper filter (to eliminate the accompanying silver x-rays). Knowing that silver x-rays are approximately 26 times more intense than the gamma radiation emitted from the source, the dose delivered from the unfiltered ^{109}Cd source, which is necessary for the bone strontium XRF system, is estimated and measured to be higher than the dose from a bone lead exam, despite the lower activity of the source used for the strontium measurement.

Chapter III

Normalization of Bone Strontium Measurements

Measuring strontium in human bone is a demanding procedure due to the need to perform many corrections prior to any estimation of the strontium levels in bone. The reliability of bone strontium XRF measurement relies on the ability to relate the measured net number of counts of characteristic x-rays to a mean concentration of strontium in the bone.

The number of detected x-rays is proportional to the strontium concentration; however, it will be strongly affected by overlying tissue thickness between the radiation source and the bone surface, as well as the tissue thickness between the detector and the bone surface. This is the most important limit for bone strontium estimation since there is great attenuation of strontium x-rays with increasing overlying tissue. Other factors that affect the net counts are source-subject and detector-subject distance, the site within the

body, and possible subject movements during the measurement. Furthermore, source strength, duration of measurement and size of detector should be accounted for before bone strontium estimation.

In an attempt to simplify the bone strontium measurement, and make it more robust for clinical application, different approaches to normalization have been investigated, and the detailed analysis as well as the results will be presented in this chapter. The main intent of these normalization techniques is to use already available information in the detected *in vivo* spectrum and to report results in a clinically relevant manner while greatly simplifying the system. In addition, the suggested techniques try to eliminate the need for an x-ray image, and thus an increase in the patient dose, as a means of assessing overlying tissue thickness for data correction. Alternatively, the tissue thickness can be measured using an ultrasound measurement.

It has been shown in the case of both lead (Somervaille *et al.*, 1985; O'Meara *et al.*, 2001) and uranium XRF measurements (O'Meara *et al.*, 1997 and 1998b) that these variations can be overcome by using coherently scattered γ-rays as an internal normalization parameter for the detected x-ray intensities. Therefore, detailed Monte Carlo simulations of coherent normalization have been performed to investigate its application to strontium assessment. As an alternative, variation in overlying tissue thickness can be corrected for by considering the strontium Kα/Kβ x-ray ratio. Another possible means of reporting results, which is more clinically relevant, might be a Sr/Ca ratio in bone. However, the attenuation of calcium x-rays in overlying tissue may preclude a practical measurement of this ratio.

If all suggested normalizations prove not to be applicable for this system, bone strontium concentrations still may be estimated using a direct calibration, once necessary signal corrections are completed. The direct calibration was successfully applied for other *in vivo* XRF systems. For example, the ^{57}Co-based bone lead system accounts for bone size and overlying tissue by taking two orthogonal planar X-rays of each subject, followed by signal corrections and calibration (Ahlgren *et al.*, 1976, Börjesson, 1996, Christoffersson *et al.*, 1984). Alternatively, an ultrasound measurement was applied prior to the bone lead L XRF measurements (Wielopolski *et al.*, 1981). Ultrasound is the preferable method because it does not increase a patient's dose in comparison to the X-ray. Therefore, throughout this work the overlying tissue thickness will be measured by ultrasound, as will be discussed in Chapter IV (Part II).

3.1 Coherent Scatter Peak Normalization of Strontium X-ray Peaks

The coherent scatter peak normalization may be used if the characteristic x-ray peak and coherent signal are produced by the same incident fluence, and if they originate from the same location in an interrogated sample. In addition, the two signals must have the same angular distribution, as well as being attenuated in a similar fashion in the media between the origin and the detector.

The original idea of coherent scatter normalization was applied to bone lead measurement in a backscatter geometry (~ 180°) using a ^{109}Cd source (Somervaille *et al.*, 1985). The benefit for the lead XRF system is utilized by the availability of a radiation

source that has an energy only 30 eV above the K edge of lead. Therefore, Compton scatter of an angle greater than 3.6° will result in scattered γ-rays below the K edge, and both the characteristic lead peak and the coherent signal are produced by the same fluence of uncollided ^{109}Cd γ-rays, as required in the first criterion. Moreover, both signals originate from the same site - bone, and have similar angular distributions, since the differential coherent scattering cross section varies very little between 120 and 180 degrees and the x-rays are emitted isotropically. Regarding the last criterion, the 88.035 keV coherent signal and 72.8 to 87.3 keV for the lead x-rays undergo similar attenuation in bone, soft tissue and air, between the signal origin and the detector, due to their similar energies. With all this established, there is only one correction that is necessary to convert any *in vivo* XRF spectrum to a lead concentration in bone, which simply accounts for the difference in coherent scatter cross sections between bone and the phantom material used in establishing the calibration lines. Therefore, it was demonstrated and successfully applied that coherent normalization eliminates all geometrical effects and the resulting x-ray to coherent ratio was simply proportional to the lead concentration in the measurement site.

The same normalization technique has been applied to uranium XRF measurements where a ^{57}Co source was positioned in a backscatter geometry (O'Meara *et al.*, 1997). In addition, coherent normalization has been investigated for a ^{57}Co-based XRF system to measure lead concentrations in the second phalanx of the forefinger with two sources, prearranged in a 90° geometry, developed by Ahlgren *et al.* in the mid-1970's (O'Meara *et al.*, 2001). Contrary to the first ^{109}Cd-based lead XRF system, these

normalizations were investigated using a Monte Carlo simulation code developed specifically for *in vivo* XRF measurements and reported by O'Meara *et al.*, 1998a.

Coherent normalization has been demonstrated to work within limits of uncertainty for the uranium system, using a ^{57}Co in backscatter geometry, although some of the main criteria are not satisfied. For this system the energy difference is 6.5 keV between the primary gamma rays and the uranium K edge, and a large fraction of Compton scattered photons can produce x-rays. Therefore, the intensity of uranium x-ray and coherent peaks are due to different incident fluencies. However, the Monte Carlo simulations demonstrated that there are countering influences in this system, and that the ratio of x-ray to coherent ratio remains constant for a wide range of geometries and soft tissue and bone thicknesses, suggesting that the normalization may be applied within certain limits (O'Meara *et al.*, 1997).

Recently published work revealed that this normalization can still be applied for the ^{57}Co-based bone lead XRF system, organized in a 90 degree geometry, even though most of the criteria are not satisfied (O'Meara *et al.*, 2001). For example, there is 34 keV energy difference between the incident γ-rays and lead K-edge. Thus singly Compton scattered photons, which have been scattered through 120 degree or less, have sufficient energy to excite lead K x-rays; hence, the lead x-rays and coherent signal are generated by different incident fluences. Since the system geometry is 90 degree, they have different angular distributions as well. Moreover, the two signals exhibit different attenuation in the tissue and bone, due to their large energy difference. The only requirement that is satisfied for this system is that both signals, lead x-rays and coherent scatter, originate from bone. Nevertheless, experiments and modeling indicated that the

coherent normalization can be used, since the ratio of x-ray to coherent peak areas over physiologically relevant bone radii and soft tissue thickness vary within 5 – 10 % of the mean ratio, within uncertainty.

Regarding the strontium XRF system with ^{109}Cd source, the primary photon energies that can excite strontium are the silver lines with energies of 22.16 and 24.94 keV. An inconvenience of the strontium system is that the x-ray and coherent scatter photons detected do not arise from the same incident fluence in the measurement site. The incident photon energies are from 6 to 9 keV above the strontium K edge, thus Compton scatter results in gamma rays with sufficient energy to excite strontium, independently of the applied scattering geometry (90 or 180 degree).

The second criterion is that both events have to originate from the same location in an interrogated sample. The strontium x-rays arise from the bone, because that is the principal storage organ for strontium. In addition, no other storage site is known for strontium and certainly, no other site is in view during the measurement. However, in principle it is not clear whether the coherent signal originates from bone and/or tissue. To address this problem the differential cross section of coherent scatter dependence with atomic number and scattering angle were calculated, as well as the differential cross section of 22.16 keV photon scattered through 90 degree for bone mineral, soft tissue and plaster of Paris (phantom material).

At 90 degrees the differential cross section of coherent scatter depends on the second or third power of atomic number, as illustrated on figure 3.1. This result suggested that the difference between the differential cross section of bone and soft tissue will not be large, as in the case of ^{109}Cd-based bone lead XRF system with value of

approximately 30 (Somervaille *et al.*, 1985). As a result, the detected coherent intensity might not be primarily from the bone.

Therefore, the differential coherent scattering cross sections were calculated using soft tissue composition from ICRU – 44 (XCOM web page) and that of bone mineral ($Ca_{10}(PO_4)_6(OH)_2$) from Woodard (1962). It may be seen that for 90 degree scatter, the soft tissue scatter cross section is approximately 3.04 times smaller than that of bone mineral. It follows that coherent scatter will originate from bone as well as from overlying soft tissue.

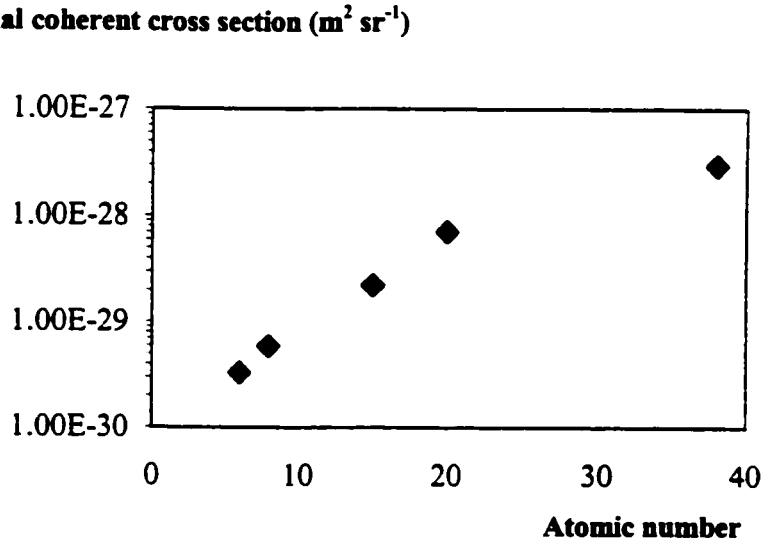

Figure 3.1 Differential cross section for coherent scatter of 22.164 keV photons with atomic number

The differential coherent scattering cross section ratio between bone and plaster of Paris was calculated to be 1.256 that has to be incorporated as a correction factor for any *in vivo* strontium concentration estimation in bone when coherent normalization is applied. This accounts for the difference in coherent scatter cross sections between bone and the phantom material used in establishing the calibration lines, as will be discussed in Part II - Chapter 4.

Moreover, figure 3.2 illustrates that at a given angle the differential cross section increases with atomic number and that the cross section difference increases with the scatter angle. For scatter angles greater than 120 degree and for high atomic number elements, the coherent scatter cross section is approximately constant, but it does vary

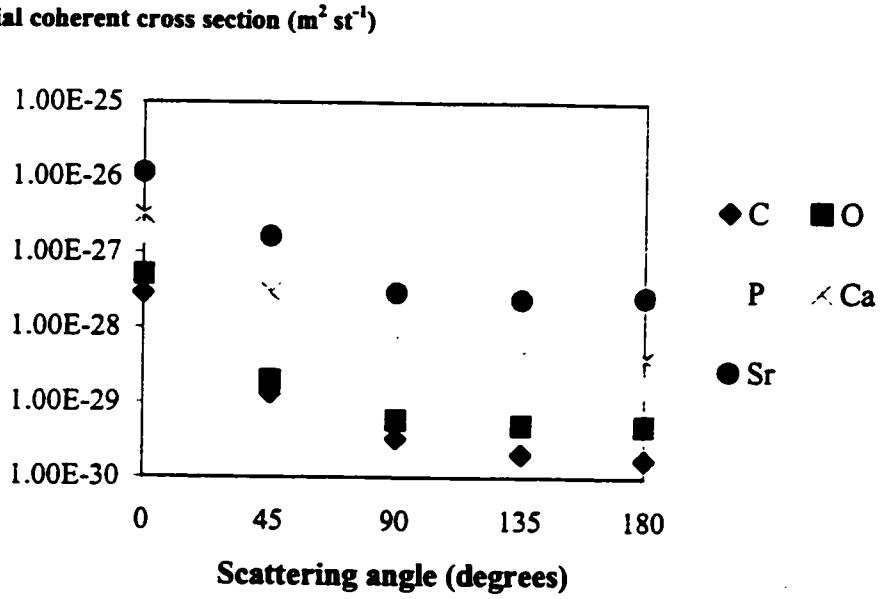

Figure 3.2 Differential cross section of coherent scatter of 22.16 keV photons versus angle of scattering.

with angle for angles around 90 degree. Therefore, the Sr x-rays and coherently scattered Ag x-rays do not have the same angular distribution at 90 degree that is an additional requirement for the coherent normalization.

In terms of the last criterion that has to be fulfilled, the attenuation of the signals has to be similar in the media between the origin and the detector. Due to the energy difference between the strontium x-rays and the silver coherently scattered signals, this criterion is not satisfied either. For example, in cortical bone the calculated attenuation coefficients for 14.16 and 22 .16 keV photons are 20.848 and 6.075 cm^{-1}. The

corresponding values in soft tissue are 2.687 and 0.874 cm^{-1} . A detailed analysis of different attenuation properties of the two primary signals will be addressed in section 3.3 of this chapter.

For all these reasons, it was uncertain if the coherent normalization may be used, and Monte Carlo simulations were necessary to establish the validity of applying coherent normalization to the strontium XRF system.

A Monte Carlo program, written by O'Meara (O'Meara *et al.*, 1998) to assess the validity of coherent normalization, was tested with the well established ^{109}Cd bone lead system that has been described in the literature repeatedly (for example Gordon *et al.*, 1993 or Chettle *et al.*, 1991). The developed code has been extensively compared to experiments, both for plaster of Paris calibration phantoms and bone, and then further adapted for the uranium and the ^{57}Co-based system for lead discussed above. The uranium modeling results have been compared to phantom measurement as well (O'Meara *et al.*, 1997).

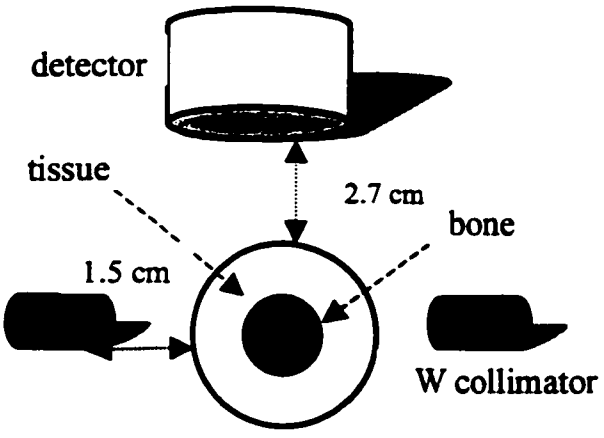

Figure 3.3 Schematic of the geometry that has been used to test the normalization method dependence on bone size and tissue thickness. As the bone radius increased, the overlying tissue thickness and distance between sample and detector, and sample and sources were kept constant.

The same code was used for the investigation of strontium for coherent normalization, once appropriate changes to input data files were completed. The simulations were run in a setup consisting of either one or two ^{109}Cd radiation

sources positioned at a 90° to the detector surface for a finger bone having 500 parts of strontium per million parts of bone mineral. Five simulations were run with bone radii varying from 0.30 to 0.50 cm while the overlying tissue thickness was kept constant at 0.60 cm. The distances between the sample and the detector surface, as well as the sample and the sources were constant at 2.7 cm and 1.5 cm respectively. Note that throughout the simulations the solid angle subtended by the detector changed because distances were kept constant. The two radiation sources were each placed inside a tungsten collimator with a collimation angle of 7 degree. Similar simulations were run with a fixed bone radius of 0.4 cm while the overlying soft tissue was varied from 0.45 cm to 0.75 cm. The schematic of both sets of simulations is presented in figure 3.3. It should be noted that the sources remain aligned with the center of the sample with changes to the geometry. The calculated results did not include detector efficiency modeling.

The overall goal of these simulations was to investigate the change in the number of x-rays detected per coherent event detected over a physiologically meaningful range of both soft tissue thicknesses and bone radii. Prior to that, the ratio of number detected to the number produced for each type of event was also investigated, over the same tissue thicknesses and bone size.

The following equation correlates the parameters that have been looked at more closely, as well as their combination to give the ratio of x-ray to coherently scattered events that are detected by the detector:

$$\left\{\frac{\#\ Xray}{\#\ coh}\right\}_{detected} = \left\{\frac{\#\ Xray}{\#\ coh}\right\}_{produced} \bullet \frac{\left(\frac{(\#\ Xray)_{det}}{(\#\ Xray)_{prod}}\right)}{\frac{(\#\ coh)_{det}}{(\#\ coh)_{prod}}} \qquad \text{(equation 3.1)}$$

$$\left\{\frac{\#\ Xray}{\#\ coh}\right\}_{detected} = \left\{\frac{\#\ Xray}{\#\ coh}\right\}_{produced} \bullet \frac{fx}{fc}$$

where on the left hand side is the ratio of x-ray to coherent photons detected by the detector, and on the right hand side is the product of the same ratio that has been produced in the sample multiplied by the ratio of fractions detected, f_x/f_c.

These ratios were independently investigated for strontium Kα and Kβ events per silver Kα and Kβ coherently scatter x-rays. Thus, four ratios were evaluated, namely $\frac{SrK\alpha}{AgK\alpha}, \frac{SrK\beta}{AgK\alpha}, \frac{SrK\alpha}{AgK\beta}$ and $\frac{SrK\beta}{AgK\beta}$.

3.1.1 Effect of Overlying Tissue Thickness on Coherent Normalization

The major limit for bone strontium XRF measurements is the attenuation of strontium x-rays in the overlying soft tissue.

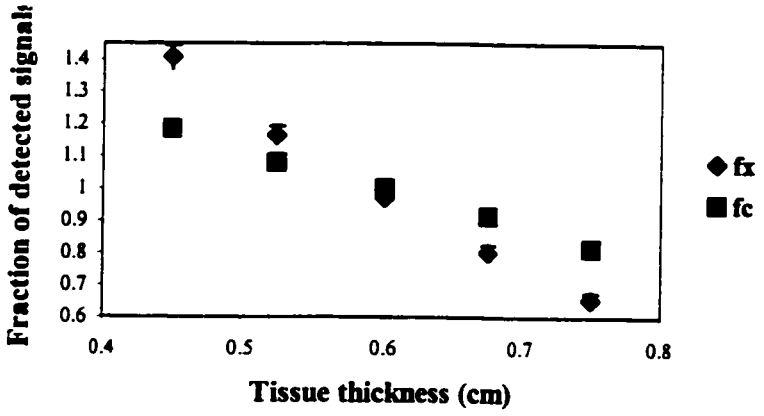

Figure 3.4 Variation of fraction of detected x-rays and coherent scatter against overlying tissue thickness.

As the overlying tissue was increased, both the fraction of detected strontium x-rays, fx, and detected coherently scattered photons, fc, decreased (figure 3.4). Due to different attenuation properties of these two signals, it was observed that strontium x-rays were more attenuated by tissue than silver Kα photons. Note, that all data have been normalized to a mean of unity such that these values can be plotted on the same scale.

The modeling resulted in no change in the number of x-rays produced per coherent scatter in bone $((\#Xray/\#coh)_{produced})$ as tissue thickness was increased, figure 3.5. It is anticipated that there should be an increase in the number of x-rays produced with increasing thickness, due to an increase in the Compton scatter component of the photon flux with sufficient energy to activate strontium in bone. Coherent events are produced only by the incident photon flux from the source, while strontium may be activated by the Compton scatter component as well as with the incident photons. Since

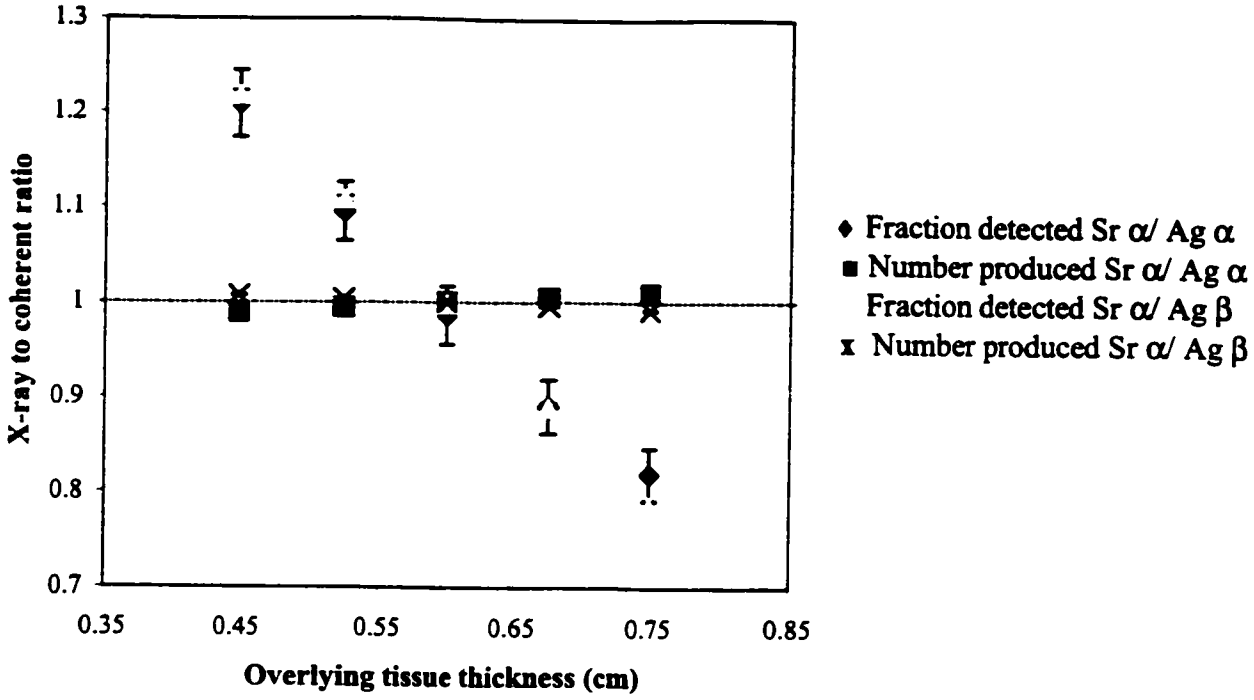

Figure 3.5 The ratio of x-ray to coherent events produced versus overlying tissue thickness. The ratio of the fractions of these events subsequently detected is also plotted. Note the uncertainties of most ratios are too small to be shown on the figure.

Compton events increase with soft tissue thickness this should increase the production of strontium x-rays as well. Nevertheless, attenuation in tissue (figure 3.4) balances the expected increase in the number of x-rays produced, making the ratio constant.

Since it is important to evaluate the dependence of the detected ratio of events on increasing tissue thickness, the ratio fx/fc has been assessed for tissue thichness variations, as demonstrated in equation 3.1. The fraction of x-rays detected, f_x, per fraction of coherently scattered photons detected, f_c, was observed to decrease with increasing soft tissue thickness as well. It is believed that two factors contribute to this decrease. First and the primary cause for the trend, is the greater attenuation of the strontium x-rays with increasing tissue thickness as compared to the coherently detected photons (figure 3.4). A second effect is the decrease in the solid angle subtended by the

detector. Throughout the simulations the fixed detector – sample distance resulted in the bone shifting further away from the detector as the tissue thickness is increased, figure 3.3. This change coupled with attenuation led to the observed decrease in the fx/fc ratio, as the amount of overlying tissue is increased.

This trend in the detected fractions affects the total ratio of strontium x-rays to coherent events detected ($(\#Xray/\#coh)_{detected}$), which was determined for increasing tissue thickness by taking the product of the two ratios plotted in figure 3.5, and as given in equation 3.1. Since the production of x-rays increases little and there is significant

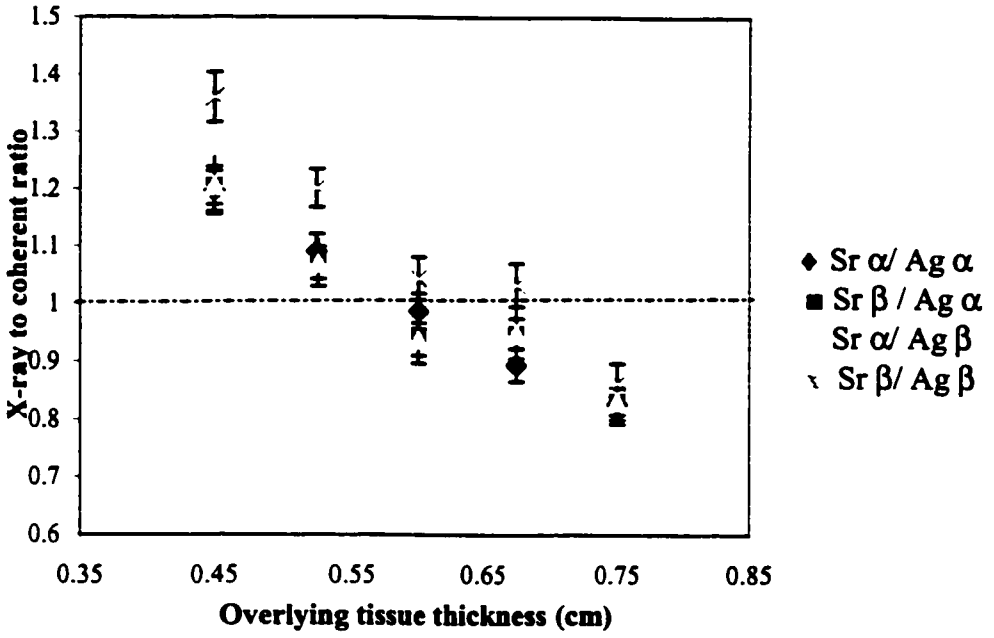

Figure 3.6 Ratio of total detected x-ray to coherent intensities versus tissue thickness.

attenuation with tissue, the net result is a decrease in the coherent ratios detected, as illustrated in figure 3.6.

Over a tissue change of 0.3 cm the resulted x-ray to coherent ratio varies within 20 % of the average value of all the simulations run. Similar simulations have been performed for a backscattering geometry (180°). The same trend has been observed with the resulting ratio change within 15% for a tissue change of 0.3 cm (data not shown).

It may be seen that signal attenuation in soft tissue might limit the use of coherent normalization for the bone strontium XRF system. However, similar simulations were done when the bone size was changed while overlying tissue thickness was constant.

3.1.2 Effect of Bone Radii on Coherent Normalization

Using the same rationale as before, the most relevant term for the application of coherent normalization is the ratio f_x/f_c. In this case the ratio is a function of the attenuation properties of the bone for the photon energies being considered, and the solid angle subtended by the detector. As the bone radius increases, there is more attenuating material in the path of the photons in the direction of the detector that more strongly attenuates the strontium signal than the coherently scattered photons. Thus, based on the different signal attenuation in bone, it is expected that f_x will decrease more rapidly than f_c, leading to a decrease of the ratio as the bone radius is increased. It is interesting to note as shown in figure 3.7 that a small difference in the attenuation of the two coherently scattered signals does not affect these trends. There is an additional loss of signal from the change in the solid angle subtended by the detector, as the bone radius is increased, although the differential attenuation is the primary reason of the observed trend.

Accordingly, as the bone radius was increased, the simulation resulted in no change of the number of strontium Kα x-rays per coherent signal produced, as well as a decrease in the number of strontium x-rays detected per coherent photon in the bone matrix (figure 3.7). Similar trends for the number produced and fraction detected are observed when the strontium Kβ photons are normalized either using the Ag Kα or Ag Kβ coherently scattered photons present in the spectrum (data not shown).

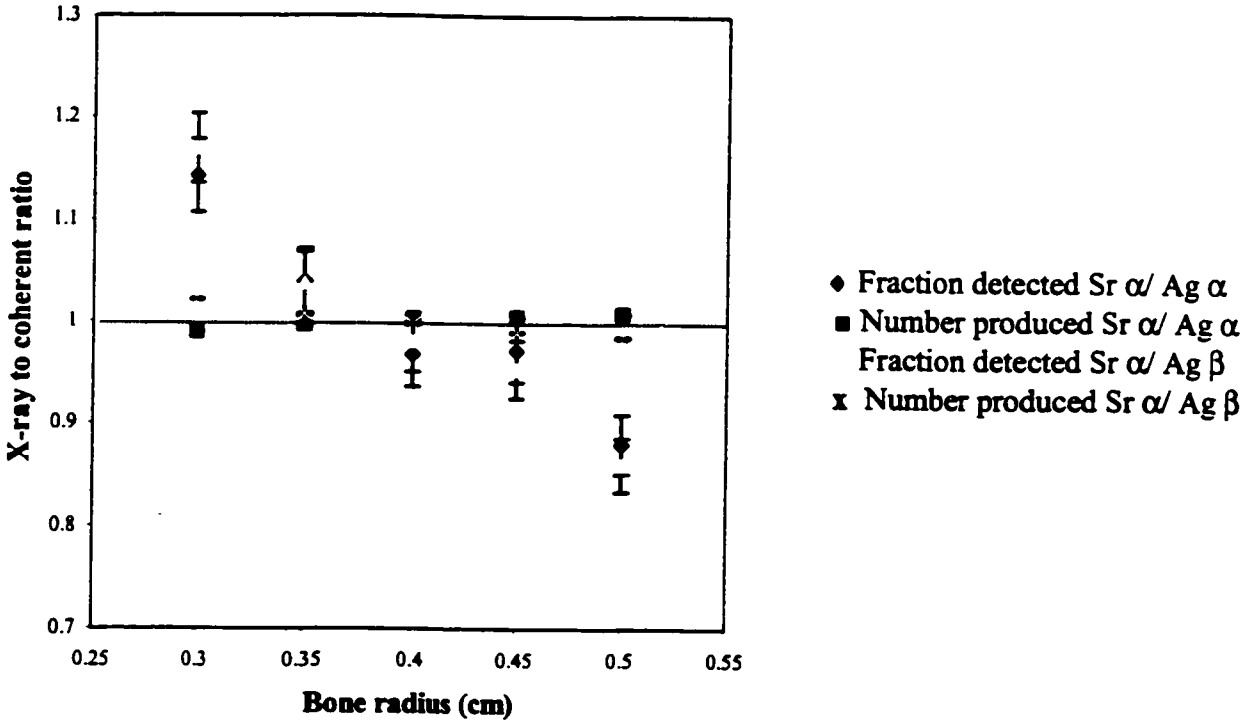

Figure 3.7 Ratio of the x-ray to coherent signal produced versus bone radius using a 90 degree geometry and two radiation sources. Also presented is the ratio of the fractions of these events subsequently detected (f_x and f_c in equation 3.1).

The combined effect is a decrease in the detected x-ray to coherent ratio as the bone radius is increased. The overall ratio of events detected, for all four possibilities is presented in figure 3.8.

Over a change of 0.3 cm in bone thickness the investigated ratio varies within 20% around the average value of the x-ray to coherent ratio for all simulations run. Although these simulations indicate an additional limit to the application of coherent normalization they are less important than signal attenuation by the tissue. Signal attenuation in bone is significant, thus, the strontium x-ray signal originates only from the

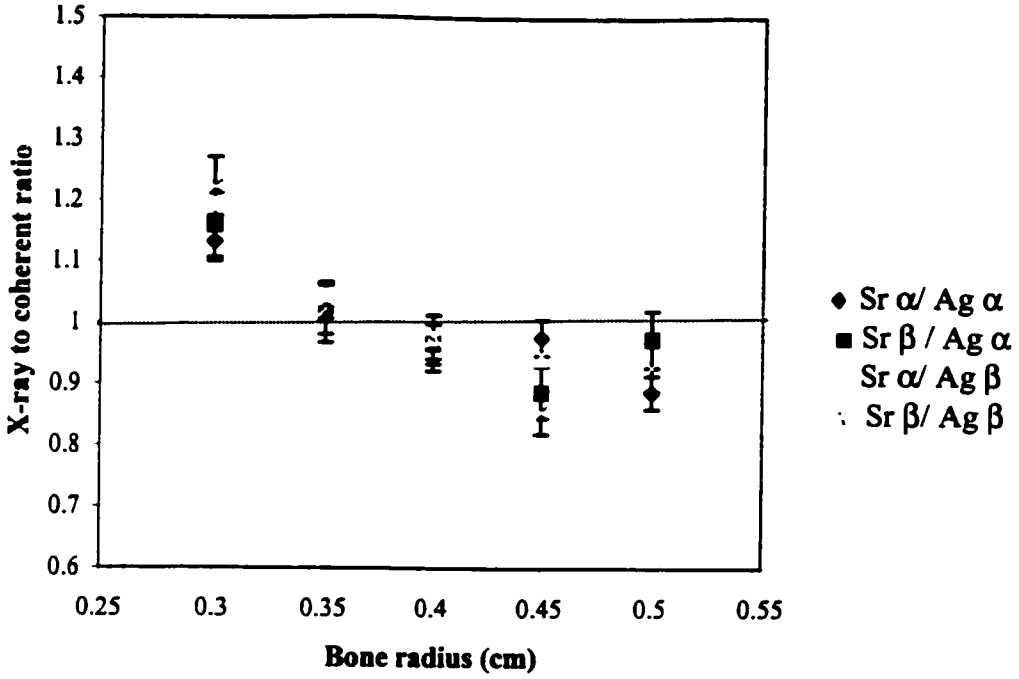

Figure 3.8 Ratio of detected x-ray to coherent intensities versus bone radius.

bone surface. On the other hand, the coherent signal changes with change in bone size, leading to the observed decrease in the x-ray to coherent ratio.

The Monte Carlo modeling suggested that the coherent normalization of bone strontium signal might not be applicable. Nevertheless, it is anticipated that conclusions reached from the modeling should be tested experimentally before completely rejecting this normalization technique.

Therefore, another approach to the normalization, which will be discussed in the next part of this chapter, was investigated hoping that it might give a possible way to normalize the strontium signal.

3.2 Strontium Kα/Kβ X-ray Ratio as a Method of Peak Normalization

In principle, strontium emits both Kα and Kβ x-rays with energies of 14.16 and 15.83 keV, respectively, that can be experimentally detected during *in vivo* measurement.

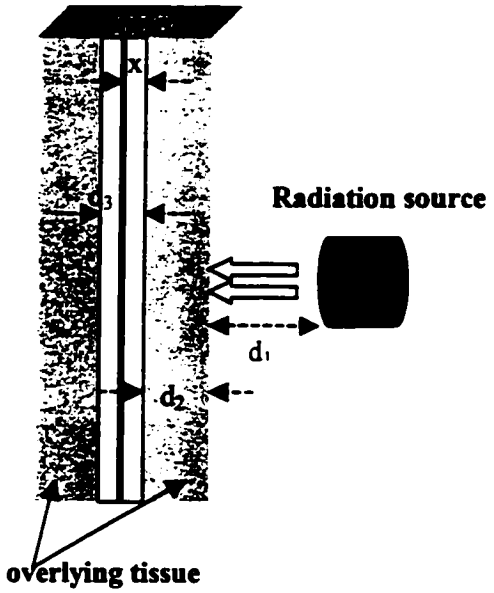

Figure 3.9 Schematic representation of the attenuation media consisting of a layer of bone, overlying tissue and air that are considered for Kα to Kβ x-ray normalization.

Let us consider the simplified model depicted in figure 3.9, in which monochromatic exciting radiation is incident upon the sample, while the detected x-ray radiation emerges from it. In this model it is assumed that strontium is homogeneously distributed throughout the bone with a thickness d_3, and is not present in the overlying soft tissue. The model considers a thin layer of bone, dx, positioned inside the bone site at a depth of x from the bone surface, and surrounded by overlying soft tissue of thickness d_2, followed by air with a thickness of d_1. Thus, the incoming Ag Kα radiation, which reaches dx, is attenuated by three media: air, soft tissue and bone. The incoming Ag Kα intensity, I_{Ag}, can be expressed by the equation

$$I_{Ag} = I_0 \exp(-(\mu_{11} d_1 + \mu_{12} d_2 + \mu_{13} x) \qquad \text{(equation 3.2)}$$

where I_0 is the intensity of incident radiation, μ_{ij} is the mass attenuation coefficient with i representing the energy of the different radiation (i = 1 Ag Kα; i = 2 Sr Kα; i = 3 Sr Kβ) and j refers to the different medium (j = 1 air; j = 2 soft tissue; j = 3 bone).

Similarly, the out-coming strontium Kα and Kβ x-rays are attenuated while traveling from their place of origin in bone toward the detector, and the attenuation of the detected radiations may be written as

$$I_{K\alpha} = c_\alpha \cdot I_0 \exp(-(\mu_{11}d_1 + \mu_{12}d_2 + \mu_{13}x)\exp(-(\mu_{21}d_1 + \mu_{22}d_2 + \mu_{23}x)dx$$

$$I_{K\beta} = c_\beta \cdot I_0 \exp(-(\mu_{11}d_1 + \mu_{12}d_2 + \mu_{13}x)\exp(-(\mu_{31}d_1 + \mu_{32}d_2 + \mu_{33}x)dx \quad \text{(equation 3.3)}$$

where c_α and c_β are the cross sections for the production of strontium Kα and Kβ x-rays, respectively.

After rearranging these equations and solving the integrals using the assumption that the x-ray signal can originate from any position inside bone ($0 < x < d_3$), the equations become

$$I_{K\alpha} = \frac{c_\alpha I_0}{(\mu_{13} + \mu_{23})}\exp(-(\mu_{11} + \mu_{21})d_1)\exp(-(\mu_{12} + \mu_{22})d_2)(1 - \exp(-(\mu_{13} + \mu_{23})d_3)$$

(equation 3.4)

$$I_{K\beta} = \frac{c_\beta I_0}{(\mu_{13} + \mu_{33})}\exp(-(\mu_{11} + \mu_{31})d_1)\exp(-(\mu_{12} + \mu_{32})d_2)(1 - \exp(-(\mu_{13} + \mu_{33})d_3)$$

It was calculated that 99 % attenuation of the strontium signal is achieved by 1.71 mm of cortical bone for Kα, and by 2.33 mm of cortical bone for Kβ x-rays. Since these thicknesses represent the signal originating from the bone surface, it may be assumed that bone is infinitely thick, and consequently, the strontium Kα/Kβ x-ray ratio may be expressed as

$$\frac{I_\alpha}{I_\beta} = \frac{c_\alpha}{c_\beta}\left(\frac{\mu_{13}+\mu_{33}}{\mu_{13}+\mu_{23}}\right)\exp(\mu_{31}-\mu_{21})d_1\exp(\mu_{32}-\mu_{22})d_2 \qquad \text{(equation 3.5)}$$

Furthermore, due to the significant difference between the attenuation coefficients in air and soft tissue, the signal attenuation in air is negligible. Thus, a simpler equation independent of bone thickness as well as the subject-detector distance can be written as

$$\frac{I_\alpha}{I_\beta} = K\exp(\mu_{32}-\mu_{22})d_2 \qquad \text{(equation 3.6)}$$

where constant K corresponds to

$$K = \frac{c_\alpha}{c_\beta}\left(\frac{\mu_{13}+\mu_{33}}{\mu_{13}+\mu_{23}}\right) \qquad \text{(equation 3.7)}$$

This result demonstrates that a linear relationship exists between the $\ln(I_\beta/I_\alpha)$ and the soft tissue thickness d_2. The corresponding mass attenuation coefficients are presented in table 3.1. Although in principle, variation in overlying tissue thickness can be corrected for by considering the strontium Kα/Kβ x-ray ratio, this approach has a limit due to the relatively large count uncertainties that have been associated with *in vivo* strontium Kβ x-rays intensities from normal subjects (please, refer to Part II - Chapter

Energy	Mass attenuation coefficient in air (cm^2/g) [$\rho = 1.21 \times 10^{-3}$ g/cm^3]	Mass attenuation coefficient in soft tissue (cm^2/g) [$\rho = 1.06$ g/cm^3]	Mass attenuation coefficient in cortical bone (cm^2/g) [$\rho = 1.92$ g/cm^3]
Silver			
22.16	0.774	0.825	3.164
24.94	0.575	0.613	2.286
Strontium			
14.16	2.400	2.535	10.858
15.83	1.809	1.917	7.988

Table 3.1 Mass attenuation coefficients for coherently scattered photons and strontium x-rays in different materials between the source and the detector. Data are calculated by extrapolation from data provided on the XCOM web page (http://physics.nist.gov/PhysRefData/Xcom/Text/XCOM.html).

IV). Thus, the uncertainty associated with the x-ray ratio itself is expected to be high. On the other hand, for a strontium measurement of subjects with moderate and/or high strontium levels, where the signal to background ratio is high, the uncertainty that accompanies the x-ray ratio normalization is expected to be at an acceptable level. Nevertheless, more data are necessary to address this prediction properly.

3.3 Strontium to Calcium X-ray peak Ratio as a Method of Normalization

Currently levels of strontium in bone are analyzed *in vitro* using atomic absorption analysis or fast neutron activation analysis and reported results are typically normalized to the calcium concentration present in bone. Therefore, this approach to normalization has been investigated as well, in an attempt to report *in vivo* results in a more familiar manner to physicians.

Calcium (Z = 20) has its $K\alpha_1$ peak located at 3.691 keV (100 relative intensity) that typically cannot be resolved at all from its $K\alpha_2$ positioned at 3.688 keV (50), and cannot be fully resolved from its $K\beta_1$' at 4.013 (19.2). Due to its low atomic number it is anticipated that the overlying tissue will significantly attenuate the out-going calcium signal from the bone. The attenuation coefficient for the calcium $K\alpha_1$ peak in soft tissue has been calculated as 78.61 cm^{-1}. Using this result, and assuming that the only attenuation will be by the overlying soft tissue surrounding the bone, the attenuation of the calcium signal has been calculated. It may be predicted that a thickness of only 0.1 cm of soft tissue will attenuate the out-going $K\alpha_1$ signal to approximately 0.04 %.

This calculation is supported by the fact that a calcium peak has not been noticed during *in vivo* measurement at two sites – finger and tibia. For example, an *in vivo* acquired spectrum of a finger, where the average overlying tissue thickness has been measured on the ten subjects as 0.294 cm, the calcium $K\alpha_1$ peak has been completely attenuated by the subject's soft tissue. In other words, for this average overlying tissue for the index finger, it may be calculated that I/I_0 is only 9×10^{-11}.

Therefore, even though it is a clinically useful method of reporting results for bone strontium measurement, the Sr/Ca ratio cannot be used for *in vivo* strontium measurements due to the attenuation of the calcium signal, predominantly in the overlying soft tissue.

Chapter IV

Pilot *In Vivo* Study of Bone Strontium Measurements

The non-invasive measurement of bone strontium in humans using source excited K x-ray fluorescence was conducted in this work. Preliminary *in vivo* measurements on ten healthy subjects for two superficial bone sites indicated that the developed XRF system could be applied for bone strontium estimation. As part of this pilot study, ultrasound measurements of tissue thickness at four anatomical sites were conducted as well. Due to the high attenuation of strontium x-rays in the overlying tissue, an effort was made to find the measurement site with the thinnest overlying tissue. The tissue thickness at the measurement sites was needed for two reasons. First to have the ability to correct incoming and outgoing signals, and the second reason was to compare the tissue thickness with the thickness that may be estimated using the $K\alpha$ to $K\beta$ normalization that was discussed in Chapter III (Part II).

Before the *in vivo* survey, it was compulsory to obtain ethics approval of the study from the McMaster Human Ethics Board, as well as to develop a consent form. Shortly after ethics approval was granted subjects were recruited for the survey. Ten healthy subjects, five female and five male, ranging from 20 to 67 years of age were selected. None of the subjects had any intentional and/or known intake of strontium other then strontium present in the diet, or was using strontium-based drugs at the time of the survey. The subjects were asked to sign the consent form prior to any measurement, and were briefly introduced to the technique. In addition, all questions and concerns were properly addressed, and the subjects were given the ability to withdraw from the study at anytime.

4.1 Overlying Tissue Measurements using Ultrasound

Four possible anatomical sites for bone strontium XRF measurements were measured using ultrasound as part of this study. The site with the thinnest overlying soft tissue would be the most suitable site. The aim of ultrasound measurements thus was to measure the tissue thickness at the finger, tibia, forehead and anklebone. As a side note, the overlying tissue thickness was correlated to subject's body mass index (BMI), and these results shall be discussed later in this section as well.

It would be preferable to measure strontium concentration in a volume containing trabecular bone, since its turnover rate has been reported to be about four times that of cortical bone (ICRP 1975). Additionally, the strontium levels are reported to be higher in

trabecular than in cortical bone in monkeys (Boivin *et al*, 1996). Thus, when mineral is lost from the skeleton any changes in elemental composition and physical density will be manifested first in trabecular bone. The only site that was included in this experiment, where bone is predominantly trabecular and with relatively thin overlying tissue, is the ankle.

Cortical bone has longer residence time for heavy elements, and therefore, may give better indication of long term accumulation. Hence, tibia was evaluated as a possible site. In addition, the finger bone was included on the list of anatomical sites on the grounds it is easily accessible for XRF measurement and it has a thin soft tissue overlay. The same rationale was used for including an overlying tissue measurement of the human forehead. Both sites are predominantly made of cortical bone.

The ultrasound measurements of subjects were done in collaboration with Mohawk College in Hamilton. A GE Logiq 700 ultrasound machine was used, and the uncertainty on each measured tissue thickness was either ± 1 mm or 3 %, whichever value was larger (1 mm in each case here). Each volunteer was measured at four selected anatomical sites:

1. Finger: A point located on the dorsal surface of the middle phalanx of the left first digit (index finger); 1 cm distal to the proximal interphalangeal (PIP) joint;
2. Left Leg: A point located 1 cm medial from the prominent ridge known as the anterior border (crest) of the tibia; located approximately between the upper 1/3 and middle 1/3 of the tibia;

3. Foot: A point located on the lateral surface of the right os calcis; specifically 1 cm distal and posterior from the most inferior part of the lateral malleolus of the fibula;

4. Forehead: A point 1 cm inferior to the hairline in the mid sagittal plane; if the patient was bald / receding, one could still visualize approximately where the hairline would have been for the measurement;

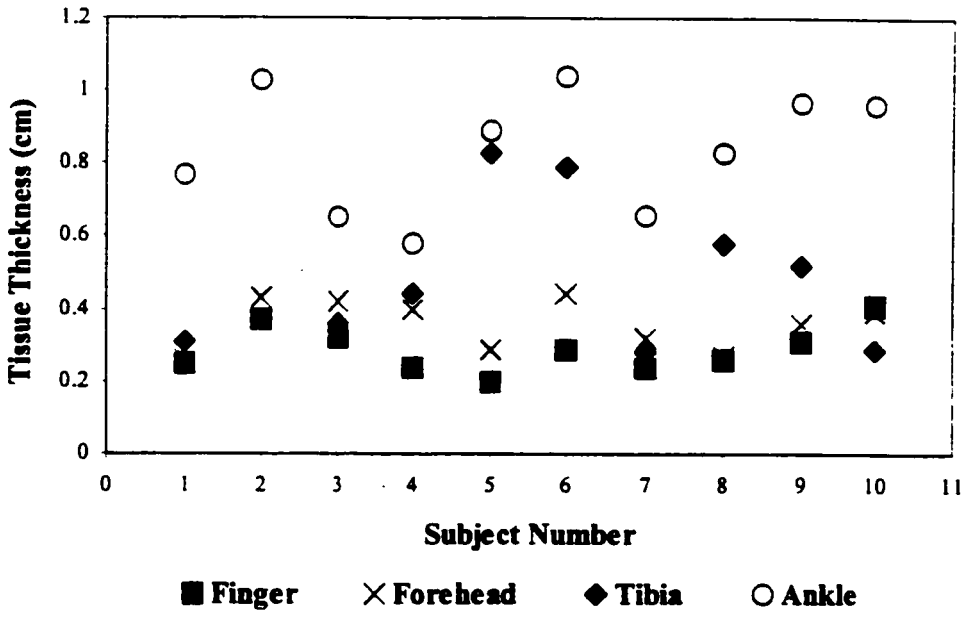

Figure 4.1 Overlying tissue thickness measured by ultrasound at four anatomical sites: finger, forehead, tibia and ankle of ten subjects (ranging from 20 to 67 years of age). The measurement uncertainty was ± 1 mm.

After finding the defined point and measuring the overlying soft tissue, a mark was made on the subject's skin. Consequently, the XRF bone measurement of the finger and tibia were performed at the same position. In addition, the subject's weight, height

and shoulder width were recorded, as the values needed to calculate the person's body mass index.

Figure 4.1 shows the tissue thickness at four anatomical sites measured in ten subjects. By visual inspection, it is possible to observe that the thinnest soft tissue covering the bone is either at the finger bone or at the forehead. The average tissue thickness at the finger was 0.289 cm with a standard deviation (SD) of 0.065. For the complete data set, the average tissue thicknesses are 0.358 cm (0.068 SD), 0.477 cm (0.200 SD) and 0.838 cm (0.167 SD) at forehead, tibia and ankle, respectively. Additionally data were subdivided into two groups (male and female), and the average tissue thickness was recalculated. The differences between sexes in respect to the soft tissue thickness did not reach statistical difference at the 5% significance level, on any of the investigated anatomical sites. However, the significance was almost reached for the overlying tissue at the finger. At the tibia, the differences between sexes are only significant at the 10% level.

These results suggest that the finger bone should be the best site for bone strontium XRF measurement having the thinnest observed overlying tissue in this data set. The forehead presents a second site that has a flatter area of bone, and thus, would be an easier site for the positioning and measurement in a 90 degree geometry than the finger. Nevertheless, XRF measurement at this site would need supporting equipment for patient positioning, that must include eye protection as well as restriction of movements during the measurement, that was not developed for this pilot study.

It is interesting to mention, based on the informal discussion with the volunteers and other subjects, that the finger is the preferred site for bone strontium measurement.

Most of the potential subjects were reluctant to expose their head to radiation. This concern originates more from public radio-phobia, rather than from the fact that the local or whole body radiation dose is high. Quite contrary, it was measured that the dose delivered during an XRF measurement is very low.

4.1.1 The Relationship Between Body Mass Index and Overlying Tissue Thickness at Four Anatomical Sites

Body mass index (BMI) can be calculated as a ratio of subjects' weight and their height squared. Alternatively, body mass index (BMI*) can be calculated as the ratio of weight, and the product of height squared and the shoulder width of the subject. Both equations were applied here, and the tissue thickness at the four anatomical sites was correlated to both the BMI and BMI*.

Since the sample size was small (N = 10), only the significance of the regression coefficients in each model (and not that of the correlation coefficient between variables in model) is addressed here. In other words, only the significance of the 'slope' and 'intercept' of the line was evaluated. This also means that the tissue thicknesses, being the predictor, are taken as fixed and not as random variables. An assessment of the significance of the co-variation between variables and a separate analysis for both sexes was performed using non-parametric techniques.

From the results, it may be concluded that amongst all predictors the tissue thickness measured at the ankle is the only significant predictor (p-level of 0.030) of the body mass index as measured by BMI, with a sample r of 0.68.

In all instances, the residual of subject 9 differed from the mean residual by more than 2 standard deviations. A separate data analysis thus was performed when this case was removed. In this case, the tissue thickness at the ankle remains significant (p-level of 0.024), but somewhat more precise (with a sample r of 0.74). Additionally in this case, it was observed that the tissue thickness of the finger becomes a predictor of BMI and BMI*, with sample p-values of 0.045 and 0.018 (r-values of 0.68 and 0.76), respectively.

Because of the lack of information regarding the distribution of the predictors, one way to overcome the limitations of the least square method in assessing the significance of the co-variation of the BMIs and the tissue thickness is to use the Spearman correlation coefficient. This non-parametric approach to the relationship between BMIs and tissue thickness supports the existence of a significant association between BMI and tissue thickness at the finger and the ankle, which was already suggested by previous analysis. Altogether, these results seem to suggest that there might be a significant linear association between BMI and the overlying tissue thickness at the finger and ankle. Nevertheless, a larger data set would help to clarify this result.

The Spearman correlation coefficient was also used to evaluate the association between these variables in both sexes separately, since five of the selected subjects were females and five males. None of the associations reached statistical significance at the 5% level with the tissue thickness at the finger emerging as the best predictor of the body

mass as measured by BMI, followed by tissue thickness at the anklebone. Overall, BMI* seems to be better predicted by tissue thickness at the tibia and ankle.

In the male subgroup, the overlying tissue thickness measured at the tibia and anklebone emerges clearly as the best predictor of the body mass. This reached statistical significance for BMI versus tibia with values of 0.037, and BMI* versus ankle of 0.037, which was suggested in the female subgroup.

These results suggest that BMI or BMI* might be used as predictors of the tissue thickness at the ankle and finger. However, a lager data set is necessary to address these correlations clearly.

4.1.2 The Relationship Between Age and Overlying Tissue Thickness

Similar data analysis was done involving the tissue thickness at the four anatomical sites and the subject's age, for the full data set of ten subjects. Age was taken as the independent variable and its normal distribution was not tested, similarly to that of the tissue thickness variables in section 4.1.1.

Age is a significant predictor of tissue thickness at the finger and tibia, in which cases the sample p-values were 0.016 and 0.023 (r-values of 0.73 and –0.70), respectively.

In the female subgroup, the tissue thickness at the tibia and ankle showed a significant association with age, as assessed by the Spearman correlation coefficient with value of -0.9 and a p-level of 0.037, in both cases. Age did not show any association with tissue thickness for the male subjects.

4.2 Experiment Design of *In Vivo* XRF Bone Strontium Measurement

The design of the bone strontium XRF system was discussed in Chapter II in detail. Nevertheless, it will be briefly outlined here as well.

It was established that ^{109}Cd (activity of 0.8 GBq at the time of measurements) in a 90 degree geometry results in the best signal-to-noise ratio in the energy range of the strontium characteristic x-rays in the spectrum. The small size radiation source was collimated using a tungsten collimator with a 7 degree collimation angle. The front face of the collimator was placed in contact with the irradiation site, while the source was placed at a depth of 2.5 cm from the collimator front face. The irradiated site was positioned in front of the large surface SiLi detector; hence, the incident and outgoing radiation formed a 90 degree angle on the surface of the subject's skin. The tungsten collimator simultaneously shielded the detector from the radiation source.

A SiLi detector was used and the detector output was passed thought the DSA-2000 digital spectroscopy unit, and then to a PC computer, which allowed the spectrum to be displayed on a monitor and the acquired spectra to be saved for later data analysis. All subjects, as well as the phantoms, were positioned at approximately 2 cm from the detector.

Once a subject was positioned, a measurement of 1800 seconds real time was conducted on two sites: the tibia of the left leg, and the second phalanx finger of the left hand. During the tibia bone measurement, the subject was seated with the source and detector positioned on the tibia, at the mark where the soft tissue thickness was measured previously using ultrasound. The leg was secure at the knee and the ankle to discourage

motion during data acquisition. Subjects were allowed to rest or walk between the two measurements. For the second measured site, the finger, the subject was seated at a table, holding a wax block to form 90 degrees to the second finger joint. The detector was lifted onto a table during the finger measurements, which allowed an easier and more comfortable position for the subjects. Nevertheless, throughout the finger measurement the subject movements were not restrained.

Contrary to phantom measurements, it was observed that the correct positioning of the subject is a very difficult task, because none of the measured sites has an ideal geometrical shape, and their shapes vary from person to person. Therefore, it is anticipated that in a case of needing to repeat measurements on the same subject, it will be essential to design an apparatus for fixing the site relative to either the detector or the source. Design of such supporting equipment has to be considered in any future *in vivo* study whenever 90 degree geometry is applied.

Strontium bone measurements are typically 30 minutes in length, and result in an effective whole body dose of 77 nSv. This is comparable to the natural background radiation dose received in approximately 20 minutes assuming an annual level of 2 mSv.

The acquired spectra were analyzed with a non-linear least squares routine designed for the phantom spectra. It is necessary to point out that the Marquardt method of data analysis can produce strontium levels that are negative, both in low-level phantoms and in human bone, although it is physically and physiologically not possible. The negative results arise from the statistical processes associated with radiation itself, as well as the way it is measured and further analyzed. The background below an x-ray peak is fitted from the regions on each side of the peak, and because of the statistical

uncertainty in each channel, the integrated signal in the region of the peak can be less than that of the background. Therefore, the x-ray intensity can be estimated as negative when low concentrations are measured. (McNeill *et al*, 1999).

After peak fitting, different approaches to strontium level estimation were applied. First, a direct estimation of strontium concentration from the calibration line generated with plaster of Paris phantoms, assuming only attenuation of the most probable and primary incoming and outgoing radiations, namely the silver Kα peak and the characteristic strontium x-rays. A second estimation was done using the x-ray to coherent normalization, incorporating the correction factor of 1.256 to allow for the difference in the differential elastic cross section between bone and constructed phantoms. Then the Kα to Kβ ratio normalization was applied, as the third suggested approach to determine strontium levels in human bone.

4.2.1 Bone Strontium Estimation by Means of the Direct Calibration

Estimation of strontium concentration from the intensity of strontium x-ray peaks using a direct calibration is an undesirable method. There are many different reasons for this, that were mentioned previously, such as a necessity to correct for the attenuation of incoming and outgoing intensities in matrix between bone and detector, source-subject and detector-subject distance, to name some. Nevertheless, for this application it seems that the investigated normalization procedures could not be reliably applied, and that the direct calibration should be used for bone strontium XRF.

As discussed in section 2.1 (tables 2.1 and 2.2), a ^{109}Cd source emits three types of incoming photons. Principal gamma radiation (88.035 keV) has a low abundance (3.61 %) and photoelectric absorption cross section for strontium of 0.95 $cm^2\ g^{-1}$. Thus although the least attenuated by the overlying tissue due to their high energy, these photons may be neglected as the source for strontium activation. Silver lines at 22.16 and 24.94 keV, on the other hand, have much higher abundance and photoelectric cross-section for strontium. Therefore, silver Kα creates 6.7 times as many strontium x-rays as silver Kβ. The attenuation of silver photons in soft tissue is significant, having mass attenuation coefficient of 0.824 and 0.613 $cm^2\ g^{-1}$ at 22.16 and 24.94 keV respectively. It was thus estimated that only 10 % of detected strontium signal would be neglected when strontium activation by silver Kβ is neglected.

Furthermore, strontium x-rays are more attenuated than silver x-rays by soft tissue, having the mass attenuation coefficients of 2.53 and 1.92 $cm^2\ g^{-1}$ at 14.16 and 15.83 keV, respectively. Combining the attenuation of silver and strontium Kαs it may be seen that 75 % of signal attenuation originates from strontium attenuation in the tissue. Thus, when silver Kβ activation of strontium is neglected only approximately 2.5 % of the detected signal attenuation will not be estimated. Knowing the uncertainty associated with *in vivo* XRF measurement is in some cases up to 60 %, neglecting this small portion of strontium signal attenuation is acceptable.

Before direct calibration, both the strontium x-rays and the silver Kα peak are corrected for the overlying tissue thickness that was premeasured by ultrasound. Using this attenuation correction and the calibration of the system (see, table 2.4) that was established in plaster of Paris phantoms, in was possible to assess the sensitivity of the

system *in vivo*. Figure 4.2 demonstrated the results of the mean concentration of ten subjects.

Each subject had a mean concentration calculated, that is an inverse variance weighted mean of the two concentrations derived from the two separate x-ray intensities (Kα and Kβ) and calibration lines.

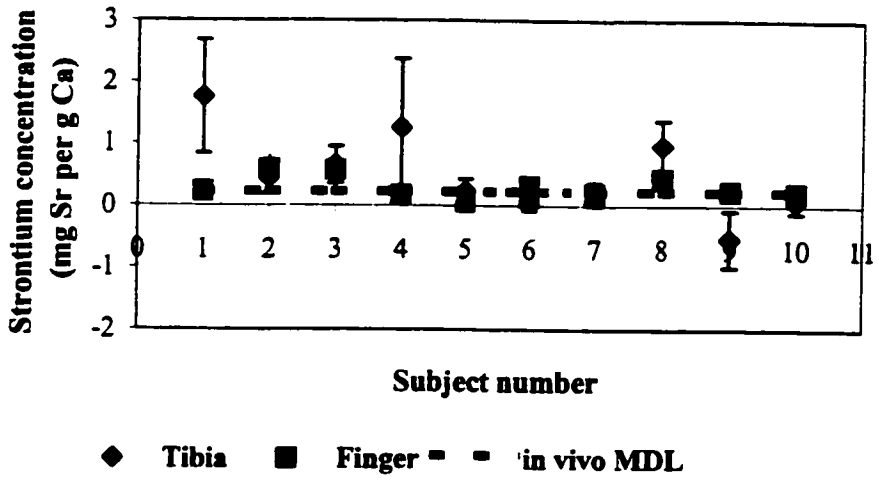

Figure 4.2 *In vivo* measurement results at two anatomical sites. Mean strontium concentration is determined as the inverse variance weighted mean of the concentrations calculated using direct calibration data shown in table 2.4. The dashed line presents the system's minimum detectible limit (MDL) of 0.25 mg Sr/g Ca in finger that was estimated using the *in vivo* data set.

The mean finger strontium concentration is 0.23 (SD 0.18) mg of strontium per gram of calcium, ranging from 0.13 to 0.58 mg Sr/g Ca. If the median value of the range of uncertainties is doubled and used as a measure of the precision of the *in vivo* system, the *in vivo* minimum detectible limit is of the order of 0.25 mg Sr/ g Ca for the finger bone. As it may be seen on figure 4.2, five subjects have strontium concentrations above

the system MDL value. However, bone strontium levels of four subjects are within the uncertainty of system's detectable limit and the strontium level of only one subject (number 5) is below the estimated MDL for the finger bone.

Similarly, the mean tibia strontium level is 0.34 (SD 0.65) mg Sr/g Ca, with the lowest and highest measured values of –0.53 and 1.76 mg Sr/g Ca in bone respectively. Higher overlying tissue thicknesses, and larger signal attenuation lead to the system's *in vivo* MDL being as high as 0.56 mg Sr/g Ca for tibia. Therefore, only four subjects (numbers 1, 3, 4 and 8) were measured with strontium levels above the MDL value and two with estimated concentrations within uncertainty of the detectable limit.

The difference in strontium concentration between the finger and tibia was addressed by calculating the individual Z scores calculated using the following equation:

$$Z = \frac{[F]-[T]}{\sqrt{\sigma_F^2 + \sigma_T^2}} \qquad \text{(equation 4.1)}$$

where [F] and [T] are the measured strontium concentration in the finger and the tibia of the same subject, and σ_F and σ_T are their associated uncertainties. If there is no difference between the strontium levels in each site, then it is expected that the individual Z values will be distributed with a mean of 0 and standard deviation of 1. A mean Z value of 0.4 with a standard deviation of 1.3 was calculated for the sample size of ten, suggesting that there is no statistically significant evidence for a difference in the strontium measured at the two sites.

4.2.2 Bone Strontium Estimation by Means of the Coherent Normalization

During the survey, six strontium phantoms (euro set of phantoms) were measured in random orientations, as a method to calibrate the XRF system. The calibration phantoms and data for the direct calibration are presented in Section 2.6. Nevertheless, to estimate the strontium concentration using coherent normalization it was required to calculate the ratio of intensities of Sr Kα and Sr Kβ to the coherent peak at 22 keV for each phantom and to recalculate the calibration parameters. Table 4.1 contains the parameters of new regression analysis, and the accompanied minimum detectable limits.

Phantom set	Slope ± σ slope) (counts(mg Sr/g Ca)$^{-1}$)	Intercept ± σ (intercept) (counts)	r^2 value	MDL (mg Sr/g Ca)
Euro set				
Kα	0.098 ± 0.005	0.35 ± 0.02	0.99	0.12
Kβ	0.018 ± 0.001	0.067 ± 0.005	0.98	0.40

Table 4.1 Summary of regression analysis of the euro phantoms measured during the *in vivo* pilot study. The ratio of strontium x-ray to coherent intensity (equation 4.1) was plotted against strontium concentrations in phantom. The minimum detectable limit (MDL) is also included in the table.

Once the *in vivo* measurements were completed, the strontium (Sr) and the coherent peak (coh) heights were determined using the non-linear least squares routine developed for phantoms, followed by the calculation of their ratio as

$$R = \frac{\text{Sr x - ray}}{\text{coh peak}}$$

$$\sigma_R = R \times \sqrt{\left(\frac{\sigma_{Sr}}{Sr}\right)^2 + \left(\frac{\sigma_{coh}}{coh}\right)^2} \qquad \text{(equation 4.2)}$$

After it was established that plaster of Paris exhibits similar attenuation of the incident fluence and characteristic x-rays to that observed in bone (Sec. 2.6), the coherent scatter cross section of these materials was calculated. A correction has to allow for the difference in the elastic scatter cross section between plaster of Paris phantom and bone mineral. The differential cross sections have been extrapolated from the tabulated data of Hubbell and Øverbø (1979). As a result, the correction factor with a value of 1.256 has to be applied to all *in vivo* strontium estimations when the coherent normalization of characteristic x-rays is used.

Figure 4.3 illustrates the results of the weighted mean concentrations in the finger and tibia of ten healthy subjects, male and female.

The average strontium concentration at finger of these volunteers is 0.061 mg Sr/g Ca, with a standard deviation of 0.04 mg of strontium per gram of calcium in bone. The corresponding values for tibia are 0.054 and 0.04 mg Sr/g Ca. The minimum detectible limit was of the order of 0.048 mg Sr/g Ca in finger bone (dashed line in figure 4.3).

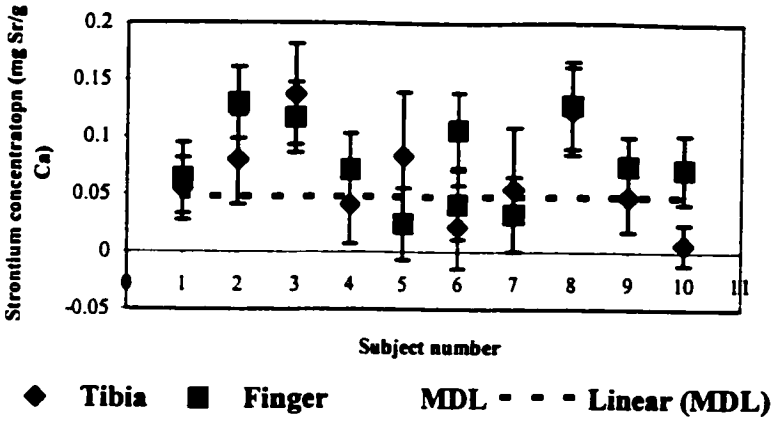

Figure 4.3 *In vivo* strontium levels at two anatomical sites measured in ten subjects calculated using the coherent normalization. Mean strontium concentrations are determined as the inverse variance weighted mean of concentrations calculated using the calibration data shown in table 4.1. The dashed line presents the system's minimum detectible limit (MDL) of 0.048 mg Sr/g Ca that was estimated using the *in vivo* data set.

These data revealed that the estimated bone strontium concentrations when the coherent normalization is applied are lower than the values reported in the literature, as well as the values that are estimated from the direct calibration. Moreover, it is observed that coherent peak intensity increased in the *in vivo* spectra in comparison to the coherent intensity measured in the bare phantom, approximately by a factor of 1.4. Since this is not the case with the bone lead XRF system, these observations were investigated further.

One of the most important requirements for legitimate normalization is that the x-ray to coherent ratio is invariant for a range of absorber thicknesses. In an experiment that is explained in the next section, where the plastic absorber was used to simulate overlying soft tissue, a coherent peak intensity increased as the thickness of plastic absorber was increased, leading to an overall decrease of the strontium x-ray to coherent ratio, as illustrated in figure 4.4.

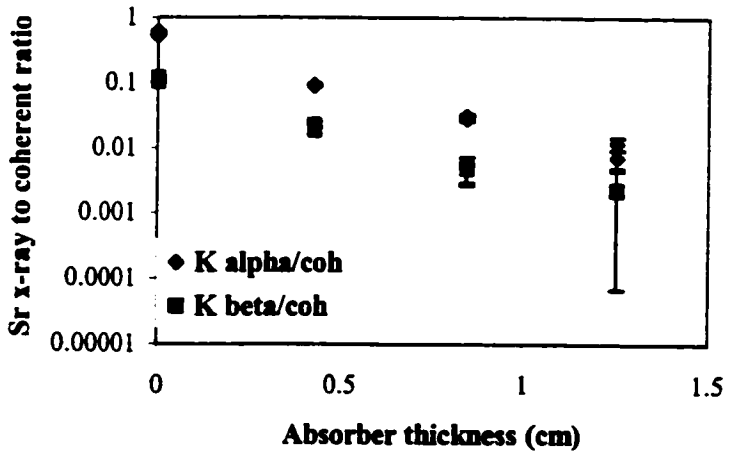

Figure 4.4 Experimental measurements of x-ray to coherent ratio as a function of plastic absorber thickness.

It was previously calculated for 90 degree scatter, that the differential cross section of bone mineral is greater only by factor of 3.04 than the same cross section of soft tissue. It follows that the coherent signal originates from both phantom and plastic absorber. A cancellation factor that is simultaneously present is coherent signal attenuation in the absorber. However, the combined effect demonstrated that there is increase in the coherent peak intensity as the absorber thickness is increased. Note that due to a design of the experiment, the solid angle viewed by the detector at the phantom changes with absorber thickness and leads to less signal detected. Nevertheless, the

predominant effect, governing a decreasing trend of x-ray to coherent ratio, is significant strontium x-ray attenuation in the plastic (figure 4.4).

As discussed in section 3.2, there are four criteria that have to be satisfied for the coherent normalization to be valid: (i) the strontium and coherent signal should be produced by same incident fluence, (ii) the two signals should originate from bone, (iii) have same angular distribution, and (iv) should be attenuated in a similar manner. Since none of these criteria is fulfilled for bone strontium XRF system, and there is not any counterbalancing factor that would give ratio that is invariant over a range of soft tissue thickness, it was concluded that this approach to normalization should be rejected for the bone strontium XRF system.

4.2.3 Soft Tissue Thickness Estimation by Means of the Kα to Kβ Normalization

Is was anticipated that the overlying tissue thickness of the irradiated bone site may be determined by taking the Kα to Kβ ratio, as discussed in Section 3.3. Once the thickness of the attenuating matrix is known, the incoming photons and outgoing radiation of the characteristic strontium x-ray peaks can be corrected for the attenuation in the overlying soft tissue, and then, straightforward strontium concentration estimation may be achieved, by simply applying the calibration generated using the bare bone phantoms. This approach would eliminate the need for an accompanying ultrasound or X-ray measurement. If X-ray radiography is used as a tool to estimate overlying tissue

thickness, the total dose delivered to the subject would be unnecessarily increased compared to that when only the XRF measurement is conducted.

This idea was tested on a simple experiment design where the phantom strontium signals were attenuated using different thickness of plastic absorber, which has similar attenuation properties to human soft tissue. Each absorber thickness was pre-measured three times at different places. Next, the plate was positioned in front of the plaster of Paris phantom that contained 2.15 mg Sr/g Ca. The spectra were acquired for 1800 s real time, three consecutive times without repositioning of either the phantom or the plastic attenuator, while the source-sample-detector geometry was 90 degree. After the strontium peaks were determined, the plastic thickness (d_2) was estimated using the following equations

$$d_2 = 2.056 - \frac{\ln(\frac{I\alpha}{I\beta})}{0.734}$$

$$\sigma_{d_2} = \sqrt{\frac{\sigma^2_{I\alpha}}{(0.734 I_\alpha)^2} + \frac{\sigma^2_{I\beta}}{(0.734 I_\beta)^2}} \qquad \text{(equation 4.3)}$$

where the constants included the mass attenuation coefficients of plaster of Paris and Perspex (polymethyl methacrylate) plastic at appropriate x-ray energies. Iα and Iβ are measured peak amplitudes of the strontium Kα and Kβ x-rays with their uncertainties, respectively. For a detailed derivation of this equation and the calculation of the constants, please refer to Section 3.3.

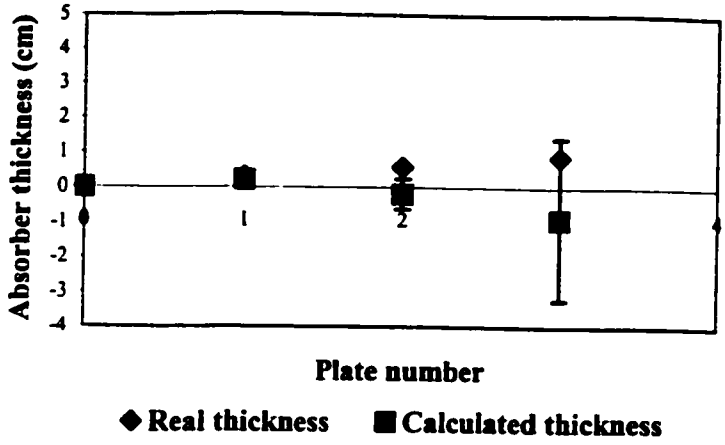

Figure 4.5 Comparison of plastic plates real thickness with the calculated value using the Kα to Kβ ratio.

Figure 4.5 demonstrates the comparison of measured and estimated plastic sheet thickness for the four experiments, with plastic thicknesses of 0, 0.30, 0.60 and 0.89 cm.

It may be concluded that the thickness of the attenuating matrix might be calculated using the ratio of strontium Kα and Kβ x-rays only when the matrix thickness is low. For the thickness larger than approximately 0.5 cm, the experimental uncertainty of the measurements accompanied with further data processing, is very large. In addition, due to the significant signal attenuation at larger thickness, the fitting might lead to a negative peak amplitude, and therefore, completely preclude the use in these calculations, since the logarithmic function of a negative number is not defined. For this experiment design, the difference between the uncertainty of the thick and thin attenuator suggests that there is a systematic error when thicker matrices are measured, thus limiting the application of this concept. The most probable source of this error is the fact that strontium low energy x-rays are easily attenuated. However, in this specific case the increase in the measurement time or source activity may lead to reduced uncertainty, and therefore, better results.

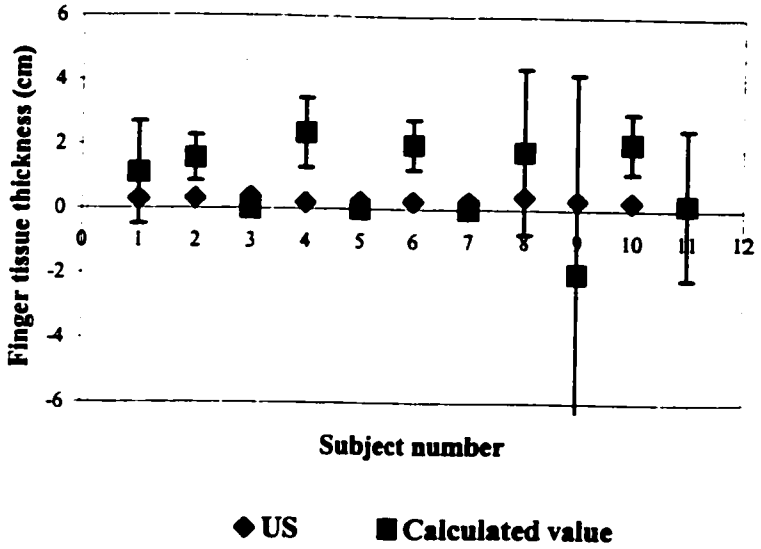

Figure 4.6 Comparison of soft tissue thickness at the finger bone measured using ultrasound and estimated by means of the Kα to Kβ ratio.

Figures 4.6 and 4.7 summarize the comparison of the soft tissue thickness measured using ultrasound (Section 4.1) and calculated from the *in vivo* strontium data. It is necessary to emphasize that in this circumstance, the equation for soft tissue thickness estimation contained the mass attenuation coefficients of bone and soft tissue as a replacement for that of plaster of Paris and Perspex. Therefore, the soft tissue thickness (d_2) is calculated using the equation

$$d_2 = 2.264 - \frac{\ln(\frac{I\alpha}{I\beta})}{0.655} \qquad \text{(equation 4.4)}$$

where Iα and Iβ are fitted peak amplitudes of strontium Kα and Kβ x-rays, respectively. The uncertainty of this estimation is similar to equation 4.3, except that the constant value of 0.655 was used instead of 0.734.

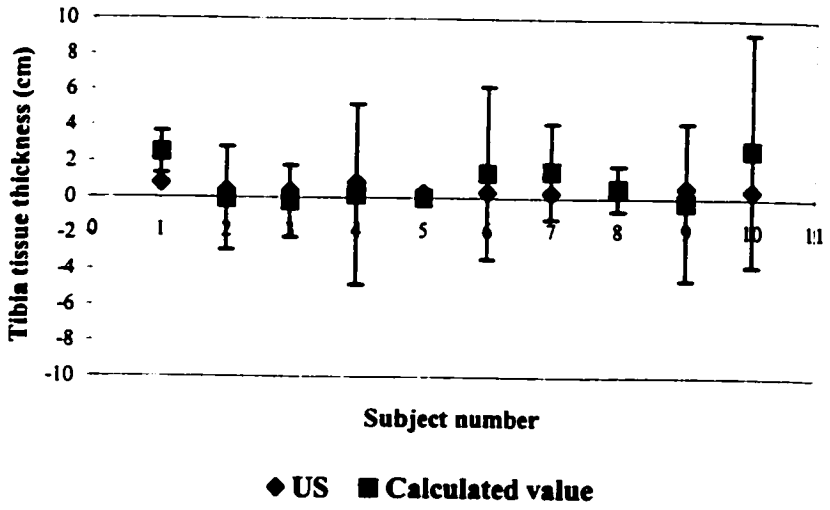

Figure 4.7 Comparison of soft tissue thickness at the tibia measured using ultrasound and estimated by means of the Kα to Kβ ratio.

As expected, the soft tissue estimation of index finger showed better agreement with the ultrasound measurements, since the overlying tissue thickness is much lower at this anatomical site. *In vivo* measurements exhibited all predicted and discussed possibilities regarding the peak amplitudes and their uncertainty, e.g. negative amplitude, and thus not defined logarithm (subjects number 3, 5 and 7 – finger tissue; subject 5 – tibia measurement), as well as an increase in the measurement uncertainty with an increase in the overlying tissue thickness.

Regarding the possibility of lowering the uncertainty of *in vivo* tissue calculations, and thus to lower uncertainty on the tissue estimation, an increase of measurement time

or repeated measurements might be considered. Unfortunately, both possibilities have limits. First is that subjects typically cannot sit immobile longer that 45 minutes, while the second possibility includes an increase in the delivered dose as well as that the subjects might not be available for the repeat measurement. The absorbed dose linearly increases with the measurement time, while the counting statistics only improve as the square root.

Once the XRF system for strontium measurements is applied to measure the element's elevated levels in the finger bone, it is expected that the tissue thickness estimation using the Kα to Kβ ratio would result in lower uncertainties on the strontium results than the uncertainties reported here. This should be simply due to the better signal-to-background ratio once more counts are detected. Consequently, this approach to estimate tissue thickness should be revisited for subjects with high strontium levels.

Chapter V

In Vivo X-ray Fluorescence Measurements of Strontium in Bone

The second part of this work concentrated on the development and testing of a system for strontium measurement in people. Contrary to neutron activation analysis that was used for aluminum bone measurement, strontium concentrations were evaluated by means of x-ray fluorescence (XRF).

Based on information available in the literature it was learned that the target and storage organ of strontium in humans is the skeleton (Boivin *et al.*, 1996; Cabrera *et al.*, 1999), in which the strontium concentration may vary between 0.1 to 0.3 mg per gram of calcium. Thus, a source-excited *in vivo* XRF system for measuring strontium in human bone was designed, and Part II - Chapter II described the process involved in this system design.

Once a compromise was reached between the basic components of a system, a collimated ^{109}Cd source was employed to excite the strontium K x-rays, with source and detector in approximately a 90 degree geometry relative to the sample surface. Strontium characteristic x-rays are detected at energies of 14.16 and 15.83 keV with a SiLi detector connected to a DSA-2000 digital spectrometer and personal computer for data storage. The DSA-2000 electronics was used throughout the course of this work, although it was recognized that another commercially available digital system, DSPEC^{PLUS}, might give better energy resolution and peak precision for this specific application. Using plaster of Paris strontium doped phantoms that simulate a bare bone, it was determined that such a system has a detection limit of 0.11 and 0.44 mg Sr/g Ca for strontium Kα and Kβ peaks, respectively. An associated effective dose of 77 nSv was delivered to a subject for 30 minute measurement time. This direct system calibration revealed that the bone strontium XRF system has a minimum detectable limit sufficient for monitoring of strontium levels in healthy subjects as well as in patients with elevated bone concentrations.

Parallel to the system design, three normalization procedures were suggested, and further evaluated once *in vivo* bone strontium spectra were acquired. For XRF in bone of a living subjects, the observed intensity of characteristic x-rays will depend on the overlying tissue thickness, source-subject and detector-subject distance, as well as the shape and size of the measured bone. Therefore, calibration should account for these inter-patient variations. During the course of this work, however, phantoms and subjects were measured at the same distances, while the overlying tissue at the measurement site was measured using an ultrasound providing the required information for the signal

attenuation correction. In addition, the system calibration was performed during the *in vivo* study to eliminate the differences due to the changes in source activity.

As was extensively discussed by Somervaille *et al.* (1985), coherent normalization is feasible and extensively used for the ^{109}Cd-based bone lead system because it satisfied a set of criteria that are discussed in detail in Chapter III (Part II). These criteria, however, are not fulfilled for some systems such as the ^{57}Co-based lead and uranium XRF systems. Nevertheless, recent publications reveal that deviations from the criteria result in several cancellation factors giving an x-ray to coherent ratio that is almost constant over a relevant range of overlying tissues and bone sizes (O'Meara *et al.*, 2001, O'Meara *et al.*, 1997).

Coherent scatter normalization, as a first approach to normalization, was evaluated by Monte Carlo simulations, to investigate its application to the bone strontium XRF system. The modeled geometry consisted of a radiation source position 90 degrees in respect to the detector, and the source was aligned with the center of the bone sample (figure 3.3). The results for physiologically relevant tissue thicknesses and bone radii suggested that coherent normalization could not be used due to the signal attenuation in the matrix. It was also demonstrated that the attenuation of strontium x-rays governs a decreasing trend in the number of x-ray to coherent events detected as the overlying tissue thickness was increased, although the attenuation of the coherent signal contributed to this trend as well. Similar results were obtained for the attenuation in bone. Since it was established that all required criteria for coherent normalization are not satisfied in the case of the bone strontium XRF system (Part II – Sec. 3.1 and 4.2.2), these results were not surprising. Final rejection of this normalization process, however, was reached once it

was experimentally observed that there is a decrease of the x-ray to coherent ratio with increasing tissue thickness. In addition, the number of coherent events was noticed to be higher in an *in vivo* spectrum than in bare bone phantoms. Since it was calculated that the ratio of differential coherent cross sections for soft tissue and bone mineral has a value of only 3.04, the experimental results were explained by the fact that the coherent signal originates from both the overlying tissue and bone. Therefore, one of the main features for applying coherent normalization, i.e. to eliminate signal variation with overlying tissue thickness, was lost, precluding the use of coherent normalization for the bone strontium XRF system.

As an alternative normalization, the strontium Kα/Kβ x-ray ratio was evaluated as a way to calculate the overlying tissue thickness, as is outlined in Section 3.2 (Part II). Given that the two signals originate from the bone surface and neglecting their attenuation in air, it was shown that the overlying tissue thickness is proportional to the Kα/Kβ x-ray ratio. Thus, the tissue thickness may be estimated using this ratio, followed by the correction of x-ray signals for the attenuation in the overlying tissue, and before applying the calibration parameters for conversion of the measured peak amplitudes to strontium concentrations in bone. Additionally, experimental results revealed that the uncertainties associated with this approach are large, thus limiting its application only to subjects with thin overlying soft tissues and elevated strontium levels. Nevertheless, more *in vivo* data are needed to evaluate this normalization.

The third suggested normalization was the assessment of the Sr/Ca ratio in bone. However, the attenuation of Ca x-rays have not permitted the use of this normalization, as described in Part II – Chapter III.

The aim of any research is to test and apply the developed design, and in that light this work is no different. The pilot *in vivo* study of ten subjects illustrated that ^{109}Cd-based XRF is capable of measuring strontium concentrations in bone. It was observed that only one subject had a strontium level that was below the system's *in vivo* detectable limit of 0.23 mg Sr/g Ca. Four subjects had higher strontium concentrations than the capability of the system reported here, while five measured volunteers had strontium concentrations within the uncertainty of the reported minimum detectable limit of the system.

The goal was to obtain the absolute concentrations of strontium and it was accompanied with significant uncertainties, even though well characterized phantoms were available. There are a number of reasons for this, the first being the large attenuation of strontium x-rays that have rather low x-ray energies. The uncertainties in concentrations arising from the attenuation in overlying tissue thickness depend upon both x-ray energy and organ depth. It was calculated that 90 % of the signal would be attenuated with only 0.84 and 1.12 cm of soft tissue for strontium Kα and Kβ respectively, clearly imposing a limit for the application of the bone strontium XRF system.

Another uncertainty can arise in defining the measurement volume and the density of matrix holding the element of interest. This is particularly important in bone XRF measurement, where a wide variation in both density and geometry between different bones is evident. Assumption about strontium distribution in bone can also be a source of uncertainty, e.g. differences in its concentration between cortical and trabecular bone. In addition, because source and detector to subject distances are small,

uncertainties in positioning can give rise to significant overall error. Thus, the geometry needs to be carefully maintained by restricting subject's movements and dimensional information needs to be obtained from either an x-ray picture or ultrasound.

Alongside *in vivo* XRF measurements, ultrasound measurements of soft tissue thickness were completed at four anatomical sites: finger, forehead, ankle and tibia. The main conclusion drawn from these tissue measurements was, that for a given data set, the thinnest soft tissue was at the index finger (the middle phalanx of the left first digit point) with a value of (0.289 ± 0.065) cm, followed by the tissue at the subject's forehead and tibia bone. The thickest overlying tissue was measured at the anklebone. The overlying tissue thickness for every subject was required for a signal correction due to its significant attenuation in soft tissue, and before the strontium concentration can be estimated using the direct calibration. Besides, these data were used to compare the tissue thickness estimated from the strontium Kα/Kβ x-ray ratio as a way to evaluate this normalization (Part II - Sec. 3.2).

5.1 Future Development and Application of X-ray Fluorescence Technique for *In Vivo* Strontium Measurement in Bone

This work has examined the possibility of measuring strontium levels in human bone. Opportunities for future work can be crudely divided into two groups such as further system development and medical application. The first group will be stressed here; nevertheless, some ideas about the system application will be also mentioned.

Other available radiation sources for bone strontium XRF should be explored. Once it was established that coherent normalization cannot be applied to the system, there is no need for the coherent peak to be positioned close to the strontium characteristic x-rays, thus a different radiation source might offer lower background below the x-ray peaks. The background under x-ray peaks can be minimized when the Compton peak is farther apart from the x-rays. The greatest advantage being gained when x-rays are above Compton energies. As suggested, a ^{125}I source might provide lower background below the strontium x-ray peaks resulting in the ability to use the 180° geometry instead of the 90°, and thus higher strontium fluorescence can be achieved.

Another avenue that needs to be explored to improve the bone strontium measurement is polarized XRF. A significant improvement had been reported by using a partly polarized x-ray source for cadmium (Cristoffersson and Mattson, 1983) and mercury (O'Meara, 1999) XRF measurements. This has the advantage that the background under the strontium peaks from Compton scattering of the primary beam might be reduced. Furthermore, the higher photon fluxes available from such a source means that for a same measurement condition and time, the system minimum detectable limit should be reduced.

The technique can be further refined by modifying a source collimator and developing one that is well tested for this specific purpose. The collimator optimization for the bone strontium measurement might lead to better signal-to-noise ratio. A couple of parameters on the collimator should be investigated further, for example diameter and size of the collimator, then source–sample distance and the shape of the collimator itself.

It is suggested that prior to any experimental time invested in the collimator optimization, Monte Carlo modeling should be undertaken.

Although digital electronics was investigated and used throughout this work, optimal running parameters need to be reevaluated. Recently it was learned that a more reliable approach to select these parameters is by using a merit number defined as a product of full-width-half-maximum of a peak and fixed real time. The lowest value of the merit number should be used for the best system performance. Moreover, DSPEC^{PLUS} electronics should be used in future work, since simply by changing to this digital electronics the system would offer better sensitivity.

It is suggested that body mass index (BMI) might be good predictor of the tissue thickness at the current measurement site of bone strontium – finger. Due to the small sample size, this possibility was only just detectable in ten subject measured. Nevertheless, the prediction of overlying tissue thickness at the finger should be checked on a larger data set. Once it is proven that the correlation exists, the BMI of each subject can be calculated as a predictor of finger tissue thickness prior to the XRF strontium measurement; hence, subject with large tissue thickness should be rejected for the measurement, and therefore, avoid unnecessary exposure to the radiation.

The bone strontium levels might be measured *in vivo* using a fast neutron activation analysis as suggested by a similar *in vitro* measurement. A major limitation of this technique is a dose that needs to be delivered to the subjects. Nevertheless, further experiments are necessary to completely assess this approach.

The final remark about bone strontium system development should be about a necessity to perform system validation by comparing the XRF measured strontium levels to results obtained by some other available method.

The medical need for *in vivo* bone strontium assessment arises because strontium may be either beneficial or harmful. Recently it has been noted, that bone strontium levels in dialysis patients with osteomalacia and children with rickets, were increased relative to patients with other types of renal osteodystrophy or to healthy subjects, possibly indicative of strontium's harmful effects. Opposite to that, there are suggestions that low levels of strontium may play an important role in treating osteoporosis, the occurrence of which constantly increases due to the aging population in developed countries. Moreover, the availability of bone strontium concentrations would be valuable information for dual energy x-ray absorptiometry, which may overestimate bone density in the presence of high strontium levels. The knowledge and ideas briefly mentioned here offer various possibilities that need to be further explored.

A relationship between strontium levels in different body site needs to be also investigated. Moreover, a correlation of *in vivo* bone strontium concentration to blood and urine levels in humans needs to be established.

The *in vivo* bone strontium XRF system that is presented in this thesis could help physicians to understand a roll of strontium in these bone processes and open new horizons to our understanding of strontium related bone problems and benefits.

REFERENCES AND BIBLIOGRAPHY

PART I *In Vivo* Neutron Activation Analysis of Aluminum in Human Bone

Ahn H. W. *et al.*, (1995), Interactive effect of fluoride and aluminum uptake and accumulation in bones of rabbits administrated both agents in their drinking water, *J. Toxicol. Environ. Health* 44, 337-350.

Alfrey A. C. *et al.*, (1976), The dialysis encephalopaty syndrome: Possible aluminum intoxication, *N. Engl. J. Med.* **294**, 184-188.

Alfrey A. C. *et al.*, (1980), Metabolism and toxicity of aluminum in renal failure, *Am. J. Clin. Nutr.* **33**, 1509-1516.

Alfrey A. C., (1980), Aluminum metabolism in uremia, *Neurotoxicology* **1**, 43.

Alfrey A. C., (1993), Aluminum and renal disease, In *Moving points in nephrology,* eds. E. Bourke, N. P. Mallick and V. E. Pollak, Basel, 110-124.

Anane R. *et al.*, (1995), Bioaccumulation of water soluble aluminum chloride in the hippocampus after transdermal uptake in m ice, *Arch. Toxicol.* **69**, 568-571.

Arnold M. L., (2000) Development of system for *in vivo* measurement of manganese, A PhD Thesis, McMaster University, Hamilton ON.

Arnold M. L. *et al.*, (2001), Monte Carlo modeling of accelerator based *in vivo* neutron activation measurements of manganese levels in human brain: system design and detection limit, 4th Topical Meeting on Industrial radiation and Radioisotope Measurement Applications, Raleigh, USA.

Best-Pattersen R. *et al.*, (1994), Neuropsychological deficit among elderly workers in aluminum production, *Am. J. Ind. Med.* **25**, 649-662.

Bevington P. R. (1992), Data reduction and error analysis for the physical sciences, 2nd Edition. McGraw-Hill, Inc., New York, USA.

Caswell R. S. *et al.*, (1982), Kerma Factors of Elements and Compounds for Neutron Energies Below 30 MeV, *Int. J. Appl. Radiat. Isot.* **33**, 1227-1262.

Chettle D. R. and Fremlin, (1984) Techniques of *in vivo* neutron activation analysis, *Phys. Med. Biol.* **29(9)**, 1011-1043.

Chettle D. R. *et al.*, (1980) Multi-elemental shielding in a mixed neutron gamma line ray field, Bulletin of Bismuth Institute, 5-6.

Eastwood J. B. *et al.*, (1990), Aluminum deposition in bone after contamination of drinking water supply, *The Lancet* **August 25, 1990**, 462-464.

Ellis, K. J. *et al.*, (1988), *In vivo* monitoring of skeletal aluminum burden in patients with renal failure, *J. of Radioanalytical and Nuclear Chemistry, Articles* **124 (1)**, 85-95.

Exley C. *et al.*, (1996), Aluminum Toxicokinetics, J. *Toxicol. Environ. Health* **44**, 569-584.

Flaten T. P., *et al.*, (1996), Status and future concerns of clinical and environmental aluminum toxicology, J. *Toxicol. Environ. Health* **44**, 527-541.

Gitelman H. J. (1989), Aluminum and Health, edited by Hillel J. Gitelman, Marcel Dekker, New York and Basel, New York.

Gitelman H. J. *et al.*, (1995), Serum and urinary aluminum levels of workers in the aluminum industry, *Ann. Occup. Hyg.* **39 (2)**, 181-191.

Green S. and Chettle, D. R. (1992), A feasibility of the *in vivo* measurement of aluminum in peripheral bone, *Phys. Med. Biol.* **37**(12), 2287-2296.

Green S. *et al.*, (1993), Characteristics of an accelerator based system for *in vivo* aluminum measurement in peripheral bone, *Human Body Composition*, Edited by K. J. Ellis and J. D. Eastman, Plenum Press, New York, 289-293.

Greger J. L. and Sutherland J. E., (1997), Aluminum exposure and metabolism, *Critical Reviews in Clinical Laboratory Science* **34 (5)**, 439-474.

Hänninen H. *et al.*, (1994), Internal load of aluminum and the central nervous system function of aluminum welders, *Scand. J. Work Environ. Health* **20**, 279-285.

Hem J. D., (1986), Geochemistry and aqueous chemistry of aluminum, Kidney *International* **29**, S3-S7.

Hubbell, J. H., Seitzer, S. M. (1996), http://physics.nist.gov/PhysRefData/contents.html

ICRP, (1971), Data for the protection against ionizing radiation from external sources, No. **21**. Pergamon Press, Oxford.

ICRP, (1975), Report of the Task Group on Reference Man, No. **23.** Pergamon Press, Oxford.

ICRP, (1995), Basic Anatomical and Physical Data for use in Radiological Protection: The Skeleton, No. **70**. Pergamon Press, Oxford.

Lefebvre A. *et al.*, (1988), Cortical vs Trabecular bone aluminum in dialyzed patients, *Am. J. Kidney Diseases* **XII (3)**, 220-226.

Leung F. Y., (1995), Trace elements in parenteral micronutrition, *Clinical Biochemistry* **28 (6)**, 561-566.

Lewis D. G. *et al.*, (1997), Monte Carlo design study of a moderated ^{252}Cf source for *in vivo* neutron activation analysis of aluminum, *Phys. Med. Biol.* **42**, 625-636.

Liskien, H., Paulsen, A. (1975), Neutron production cross sections and energies for the reactions $^{7}Li(p,n)^{7}Be$ and $^{7}Li(p,n)^{7}Be^{*}$, *Atomic Data Nucl. Tables* **15 (1)**, 57-84.

Ljunggren K. G. *et at.*, (1990), Blood and urine concentrations of aluminum among workers exposed to aluminum flake powders, *British. J. Ind. Med.* **48**, 106-109.

Nuclear Data Tables, part 3 (1960), National Academy of Science, Washington, DC.

Martyn C. N. *et al.* (1989), Geographical relation between Alzheimer's disease and aluminum in drinking water, *The Lancet* **January 14, 1989**, 59-62.

McLachan, D. R. C. *et al.*, (1991), Would decreased aluminum ingestion reduce the incidence of Alzheimer's disease?, *Can. Med. Assoc.* **145 (7)**, 793-804.

Moreno A. *et al.*, (1994), Aluminum in the neonate related to parenteral nutrition, *Acta. Peadiatr.* **83**, 25-29.

O'Mahony D. *et al.*, (1995), Bone Aluminum Content in Alzheimer's Disease, *Dementia* **6**, 69-72.

Palerme S. *et al.*, (1993a), Pilot Study for *in vivo* Aluminum Measurement, Edited by K. J. Ellis and J.D. Eastman, Plenum Press, New York, 303-306.

Palerme S. (1993b), Pilot Studies for *In Vivo* Bone Aluminum Measurement, A Master's Thesis. McMaster University, Hamilton ON.

Pejović-Milić A. (1998), An Accelerator Based *In Vivo* Measurement of Aluminum in Humans by Neutron Activation Analysis, A Master's Thesis. McMaster University, Hamilton ON.

Pejović-Milić A. *et al.* (1998a), Development of an Accelerator Based Determination of Aluminum Burden in Peripheral Bone by Neutron Activation Analysis, *Appl. Radiat. Isot.* **49 (5/6)**, 717-719.

Pejović-Milić, A. *et al.*, (1998b), The Development of an *in vivo* Procedure for Routine Aluminum Monitoring in Human Bone by Neutron Activation Analysis, COMP & CCPM Conference Proceedings, London, Canada, 222-224.

Pejović-Milić A. *et al.*, (2000), Monte Carlo design study for *in vivo* bone aluminum measurement using a low energy accelerator beam, *Appl. Radiat. Isot.* **53**, 657-664.

Pennington J. A. T. (1983) Revision of the total diet study food list and diets, *J. Am. Diet. Assoc.* **82 (2)**, 166-173.

Pennington J. A. T. (1988) Aluminum content of foods and diets, *Food Additives Contaminants* **5 (2)**, 166-232.

Rifat S. L. *et at.*, (1990), Effect of exposure of miners to aluminum powder, *The Lancet*, **Nov. 10, 1990**, 1162-1165.

Riihimäki V. *et al.*, (2000), Body burden of aluminum in relation to central nervous system function among metal inert-gas welders, *Scand. J. Work Environ. Health* **26 (2)**, 118-130.

Robushkin I. *et al.*, (1995), Aluminum on surface water of the Kola Peninsula, Russia, *Sci. Total Environ.* **163**, 55-59.

Rogers D. W., (1979), Why not to trust a neutron remmeter, *Health Physics* **37 (6)**, 735-742.
Spencer A. J. *et al.*, (1995), Deposition of aluminum in kidney following aluminum chloride or citrate administration in rats, *J. Physiol. London*, **483**, 171-172.

Schmid K. *et al.*, (1995) Use of bone mineral content determination by X-ray absorptiometry in the evaluation of osteodystrophy among workers exposed to aluminum powders, *Sci. Total Environ.* **163**, 147-151.

Scott M. C. and Chettle D. R., (1986), *In vivo* elemental analysis in occupational medicine, *Scand. J. Work. Environ. Health* **12**, 81-96.

Sedman A. B. *et al.*, (1985), Evidence of aluminum loading in infants receiving intravenous therapy, *N. Engl. J. Med.* **312**, 1337-1343.

Sjogren B. *et al.*, (1988), Uptake and urinary excretion of aluminum among welders, *Int. Arch. Occup. Environ. Health* **60**, 77-79.

Sjogren B. *et al.*, (1990), Neuropsychiatric symptoms among welders exposed to neurotoxic metals, *British. J. Ind. Med.* **47**, 704-707.

Sokolowski T. W, (1989), Neutron dose measurement by means of a tissue equivalent proportional counter, A Master's Thesis. McMaster University, Hamilton ON.

Sutcliffe J. S., (1996), Review of *in vivo* experimental methods to determine the composition of the human body, *Phys. Med. Biol.* **41**, 791-833.

White D. M. *et al.*, (1992), Neurologic Syndrome in 25 workers from an aluminum smelting planet, *Arch. Intern .Med.* **152**, 1443-1448.

Wyatt R. M. *et al.*, (1993a), Development of an *in vivo* neutron activation analysis technique to measure bone aluminum, *Human Body Composition*, Edited by K. J. Ellis and J. D. Eastman, Plenum Press, New York, 319-321.

Wyatt R. M. *et al.*, (1993b), Development of a technique to measure bone aluminum content using neutron activation analysis, *Physiol. Meas.* **14**, 327-335.

Yanch J. C. *et al.*, (1992), Accelerator-based epithermal neutron beam design for neutron capture therapy, *Med. Phys.* **19(3)**, 709-721.

Yu W. *et al.*, (1998), Measurements of the neutron yields from $^{7}Li(p,n)^{7}Be$ reaction (thick target) with incident energies from 1.885 to 2.0 MeV, *Med. Phys.* **25(7)**, 1222-1224.

PART II *In Vivo* X-ray Fluorescence of Strontium in Human Bone

Ahlgren L. *et al.*, (1976), X-ray fluorescence and analysis of lead in human skeleton *in vivo*, *Scan. J. Work Environ. And Health* **2**, 82-86.

Bevington P. R. (1992), Data reduction and error analysis for the physical sciences, 2nd Edition. McGraw-Hill, Inc., New York, USA.

Boivin G. *et al.*, (1996), Strontium distribution and interaction with bone mineral in monkey iliac bone after strontium salt (S 12911) administration, *J. Bone Miner. Res.* **11(9)**, 1302-1311.

Börjesson J., (1991), Measurements of platinum, gold and mercury *in vivo*: an analysis of the Göteborg XRF *in vivo* measurement system: improvements, tests, and patient measurements, Thesis, Dept. of Radiation Physics, Univ. of Göteborg, Sweden.

Börjesson J. *et al.*, (1995a), *In vivo* XRF analysis of mercury: relation between concentrations in the kidney and urine, *Phys. Med. Biol.* **40**, 413-426.

Börjesson J. and Mattson S, (1995b), Toxicology: *In vivo* x-ray fluorescence for the assessment of heavy metal concentrations in man, *Appl. Radiat. Isot.* **46 (6/7)**, 571- 576.

Börjesson J., (1996), Studies of cadmium, mercury and lead in man, A Ph.D. Thesis, Dept. of Radiation Physics, University of Göteborg, Sweden.

Cabrera W. E. *et al.*, (1999), Strontium and bone, *J. Bone Miner. Res.* **14(5)**, 661-668.

Chettle D. R. *et al.*, (1990) Measurements of Trace Elements *In Vivo*, in `*In Vivo* Body Composition Studies' ed. S. Yasumura, J.E. Harrison, K.G. McNeill, A.D. Woodhead, F.A. Dilmanian, Plenum Press, 247-257.

Chettle D. R. *et al.*, (1991), Lead in bone : Sampling and Quantitation using K x-rays excited by ^{109}Cd, *Environ. Health Perspectives*, **91**, 49-55.

Christoffersson J. O. and Mattson M., (1983), Polarized x-rays in XRF analysis for improved *in vivo* delectability of cadmium in man, *Phys. Med. Biol.* **28**, 1135-1144.

Christoffersson J. O. *et al.*, (1984), Lead in finger bone analyzed *in vivo* in active and retired workers, *Am. J. Ind. Med.* **6**, 447-457.

Christoffersson J. *et al.*, (1997), Effects of strontium ions on growth and dissolution of hydroxyapatite and on bone mineral detection, *Bone* **20(1)**, 47-54.

Gordon C. L. *et al.*, (1993), An improved instrument for the *in vivo* detection of bone lead, *British J. Ind. Med.* **50**, 637-641.

Grynpas M. D. *et al.*, (1990), Effects of low doses of strontium on bone quality and quantity in rats, *Bone* **11**, 313-319.

Heinmiller B. (1988), Photon response of $Li_2B_4O_7$:Cu thermoluminisecent dosimeters, A M.Sc. Thesis, McMaster University, Hamilton, Canada.

Hoffer P. B. *et al.*, (1968), Fluorescent thyroid scanning – a new method of imaging the thyroid, *Radiology* **90**, 342.

Hubbell J. H. and Øverbø I. (1979), Relativistic atomic form factors and photon coherent scattering cross sections, *J. Phys .Chem. Ref.Data* **8(1)**, 69-105.

Hult M. and Fessler A., (1998), Sr/Ca mass ratio determination in bones using fast neutron activation analysis, *Appl. Radiat. Isot.* **49 (9/11)**, 1319-1323.

ICRP, (1975), Report of the Task Group on Reference Man, No. **23.** Pergamon Press, Oxford.

Jonson R. *et al.*, (1988), A method for *in vivo* analysis of platinum after chemotherapy with cisplatin, *Phys. Med. Biol.*, **33**, 847-857.

Knoll G. F. (1989), Radiation Detection and Measurement, 2nd Edition. John Wiley and Sons, New York, USA.

Lederer C. M. and Shirley V. S. (1978), Table of Isotopes, 7th Edition. John Wiley and Sons, New York, USA.

Leeuwenkamp O. R. *et al.*, (1990), Human pharmacokinetics of orally administrated strontium, *Calcif. Tissue. Int.* **47**, 136-141.

Leung P. L. and Huang H. M., (1997), Analysis of trace elements in the hair of volunteers suffering from Naso-Pharyngeal Cancer, *Biol. Trace. Elem. Res.* **57**, 19-25.

Marie P. J.. *et al.*, (1993), An uncoupling agent containing strontium prevent bone loss by depressing bone resorption and maintaining bone formation in estrogen-deficient rats, *J. of Bone and Mineral Res.* **8(5)**, 607-615.

Mattson S. and Scott M. C. (1989), *In vivo* elemental analysis using x-ray fluorescence: technique and applications, 2nd International workshop on XRF and PIXE in the life Sciences, Capri, June 29-30, 1989.

Mauras Y. *et al.*, (1986), Increase in blood plasma levels of boron and strontium in hemodialyzed patients, *Clinica. Chemica. Acta.* **156**, 315-320.

McNeill F. E. *et al.*, (1999), Factors affection in vivo measurement precision and accuracy of ^{109}Cd K x-ray fluorescence measurements, *Phys. Med. Biol.* **44**, 2263-2273.

Nielse S. P. *et al.*, (1999), Influence of strontium bone mineral density and bone mineral content measurements by dual x-ray absorptiometry, *J. Clin. Densitom.* **2(4)**, 371-379.

O'Meara J. M. *et al.*, (1997) The feasibility of measuring bone uranium concentrations *in vivo* using source excited K x-ray fluorescence, *Phys. Med. Biol.* **42**, 1109-1129.

O'Meara J. M. *et al.*, (1998a), Monte Carlo simulation of source-excited *in vivo* x-ray fluorescence measurements of heavy metals, *Phys. Med. Biol.* **44**, 1413-1428.

O'Meara J. M. *et al.*, (1998b), The validity of the coherent scatter peak normalization of x-ray intensities detected during *in vivo* XRF measurements of metals in bone, *Advances in X-ray Analysis* **41**. 932-940.

O'Meara J. M., (1999) Measuring lead, mercury and uranium by *in vivo* x-ray fluorescence, A PhD Thesis, McMaster University, Hamilton ON.

O'Meara J. M. *et al.*, (2001), Normalization with coherent scatter signal: improvements in the calibration procedure of the ^{57}Co-based *in vivo* XRF bone-Pb measurement, *Appl. Radiat. Isot.* **54**, 319-325.

Özgür S. *et al.*, (1996), Rickets and soil strontium, *Archives of Disease in Childhood* **75**, 524-526.

Reginster J. Y., (1997), Miscellaneous and experimental agents, *Am. J. Med. Scs.* **313(1)**, 33-40.

Reginster J. Y. *et al.*, (1999), Treatment of osteoporosis: where are we and where are we going to, *Morphologie* **83(261)**, 41-45.

Rudolph H. *et al.*, (1973) Muscle and serum trace elements profile in uremia, *Trans. Amer. Soc. Artif. Int. Organs.* **19**, 456-461.

Shakeshaft S. and Lillicrap S. C., (1993), An x-ray fluorescence system for the determination of gold *in vivo* following chrysotherapy, *Br. J. Rad.* **66**, 714-717.

Snyder R. E. and Secord D. C., (1982), The *in situ* measurement of strontium content in bone using x-ray fluorescence analysis, *Phys. Med. Biol.* **27(4)**, 515-529.

Somervaille L. J. *et al.*, (1985), In vivo measurement of lead in bone using x-ray fluorescence, *Phys. Med. Biol.* **30 (9)**, 929-943.

Todd A. C. *et. al.*, (1992), *In vivo* x-ray fluorescence of lead in bone using K x-ray excitation with ^{109}Cd source: radiation dosimetry studies, *Environ. Res.* **57**, 117-132.

Verbeke J. M., (2000), Development of high-intensity D-D and T-D neutron sources and neutron filters for Medical and industrial application, PhD Thesis, University of California, Berkeley, USA.

Wielopolski L. *et al.*, (1981), Feasibility study for *in vivo* measurement of lead in bone using L-X-ray fluorescence, *IEEE Trans. Nucl. Sc.* **28**, 114-116.

Wielopolski L. *et al.*, (1983a), Feasibility of noninvasive analysis of lead in the human tibia by soft x-ray fluorescence, *Med. Phys.* **10(2)**, 248-251.

Wielopolski L. *et al.*, (1983b), Application of XRF to measure strontium in human bone *in vivo*, *Adv. X-ray Anal.* **26**, 415-421.

Wielopolski L. *et al.*, (1989), *In vivo* measurement of cortical bone lead using polarized x-rays, *Med. Phys.* **16**, 521-528.

Wielopolski L., (1999), Design consideration for an EDXRF system for *in vivo* elemental analysis, *Advances in X-ray Analysis* **41**, 892-897.

Woodard H. Q., (1962),The elemental composition of human cortical bone, *Health Physics*, **8**, 513-517.

XCOM web page (http://physics.nist.gov/PhysRefData/Xcom/Text/XCOM.html).

Zaichick V. Y., (1994), Instrumental activation and x-ray fluorescence analysis of human bone in health and disease, *Journal of Radioanalytical and Nuclear Chemistry* **179(2)**, 295-303.